Abstract

Due to recent progress in theory and the growing number of physical realizations, low-dimensional quantum magnets continue to receive a considerable amount of attention. They serve as model systems for investigating numerous physical phenomena in spin systems with cooperative ground states, including the field-induced evolution of the ground-state properties and the corresponding rearrangement of their low-energy excitation spectra. This work is devoted to systematic studies of recently synthesized low-dimensional quantum spin systems by means of multi-frequency high-field electron spin resonance (ESR) investigations. In the spin-$\frac{1}{2}$ chain compound $(C_6H_9N_2)CuCl_3$ [known as (6MAP)$CuCl_3$] the striking incompatibility with a simple uniform $S = \frac{1}{2}$ Heisenberg chain model employed previously is revealed. The observed ESR mode is explained in terms of a recently developed theory, revealing the important role of the alternation and next-nearest-neighbor interactions in this compound. The excitations spectrum in copper pyrimidine dinitrate $[PM{\cdot}Cu(NO_3)_2(H_2O)_2]_n$, an $S = \frac{1}{2}$ antiferromagnetic chain material with alternating g-tensor and Dzyaloshinskii-Moriya interaction, is probed in magnetic fields up to 63 T. To study the high field behavior of the field-induced energy gap in this material, a multi-frequency pulsed-field ESR spectrometer is built. Pronounced changes in the frequency-field dependence of the magnetic excitations are observed in the vicinity of the saturation field, $B \sim B_s = 48.5$ T. ESR results clearly indicate a transition from the soliton-breather to a spin-polarized state with magnons as elementary excitations. Experimental data are compared with results of density matrix renormalization group calculations; excellent agreement is found. ESR studies of the spin-ladder material $(C_5H_{12}N)_2CuBr_4$ (known as BPCB) completes the determination of the full spin Hamiltonian of this compound. ESR results provide a direct evidence for a pronounced anisotropy in this compound, that is in contrast to fully isotropic spin-ladder model employed previously for BPCB. Our observations can be of particular importance for describing the rich temperature-field phase diagram of this material. The frequency-field diagram of magnetic excitations in the quasi-two dimensional $S = \frac{1}{2}$ compound $[Cu(C_4H_4N_2)_2(HF_2)]PF_6$ in the AFM-ordered state is studied. The AFM gap is observed directly. Using high-field magnetization and ESR results, parameters of the effective spin-Hamiltonian (exchange interaction, anisotropy and g-factor) are obtained and compared with those estimated from thermodynamic properties of this compound.

High-field electron spin resonance in low-dimensional spin systems

DISSERTATION

zur Erlangung des akademischen Grades

Doctor rerum naturalium
(Dr. rer. nat.)

vorgelegt

der Fakultät
Mathematik und Naturwissenschaften

TECHNISCHE
UNIVERSITÄT
DRESDEN

von

Mykhaylo Ozerov
geboren am 21.04.1982 in Storozhynets, Ukraine

HLD

Forschungszentrum
Dresden Rossendorf

HOCHFELD-MAGNETLABOR DRESDEN
Forschungszentrum Dresden-Rossendorf e. V.
2010

GUTACHTER:

Prof. Dr. Joachim Wosnitza
Prof. Dr. Bernd Pilawa

Eingereicht am: 14. Dezember 2010
Tag der Verteidigung: 04. Mai 2011

Із глибокою вдячністю - моїй мамі …
(With deep thankfulness - to my mother ...)

Content

1. Motivation

Due to their unusual physical properties, low-dimensional (hereafter low-D) magnets have recently attracted a great deal of attention. The presence of quantum fluctuations, significantly enhanced in spin systems with reduced magnetic dimensionality, gives rise to a variety of strongly correlated states determining unusual magnetic properties (including field-induced quantum phase transitions, formation of quantum spin gaps, etc.). To comprehend the role of quantum fluctuations in strongly correlated electron systems, it is important to explore their phenomenology in simple and well-controlled model systems. Because of that, studies of magnetic properties of low-D spin systems appears to be one of the most important problems of modern solid-state physics.

Electron spin resonance (ESR) is traditionally recognized as one of the most powerful and sensitive tools for probing magnetic excitations in exchange-coupled spin systems. Using the temperature or magnetic field as a tuning parameter, one can obtain valuable information on the nature of the ground state in these systems and estimate their important physical parameters and constants. In particular, high-field multi-frequency ESR spectroscopy can provide detailed knowledge on the energy-level diagram, often allowing (that is of particular importance) the observation of energy gaps directly.

In this work, some of the most important representatives of low-D magnetism (spin chains, spin ladders, and quasi-2D spin systems) have been studied by means of high-magnetic-field multi-frequency ESR. The thesis is organized as follows:

In Chapter 2, the experimental techniques developed at the HLD (Hochfeld Magnetlabor Dresden) and used for the high-field ESR experiments is described.

Chapter 3 describes magnetic and resonance properties of the quasi-1D chain system $(C_6H_9N_2)CuCl_3$. The analysis of ESR and magnetic properties of this material is analyzed based on the recently developed mean-field-like theory illuminating the important role of the next-nearest-neighbour (NNN) interactions.

In Chapter 4, the ESR excitation spectrum of Cu-PM, a spin-$\frac{1}{2}$ chain system with alternating Dzyaloshinksii-Moriya interactions and staggered g-tensor, is studied. The crossover from the sine-Gordon regime (with soliton and breathers as elementary magnetic excitations) to the fully spin-polarized state (with excitation spectrum formed by magnons) is observed. Experimental data show an excellent agreement with the results of the density matrix renormalization group calculations.

In Chapter 5, the spin-ladder material $(C_5H_{12}N)_2CuBr_4$ is studied by means of ESR. The studies provide straightforward evidences of a pronounced anisotropy in this compound, which is inconsistent with the isotropic spin-ladder model employed for this system previously. Our findings illuminate the importance of taking into account the anisotropy effects in $(C_5H_{12}N)_2CuBr_4$ for describing its magnetic properties in the vicinity of the quantum critical points.

Chapter 6 contains results of high-field magnetization, specific-heat, and ESR studies of the quasi-two-dimensional material $[Cu(C_4H_4N_2)_2(HF_2)]PF_6$. It is argued that despite the onset of three-dimensional long-range magnetic ordering the magnetic properties of this material are strongly affected by two-dimensional spin correlations. Combination of the high-field ESR data with results of high-field magnetization allows accurate estimation of the spin-Hamiltoinian parameters used for the interpretation of unusual magnetic properties of this compound.

The main results of this work are summarized in Chapter 7.

2. Experimental techniques

2.1. Introduction

Electron spin resonance (sometimes called electron paramagnetic resonance or EPR) provides a powerful means for investigations of low-energy magnetic excitations in numerous magnetic substances. It is widely accepted in the high-field ESR community that despite of high resolution and sensitivity, the application range of commercially available ESR spectrometers (with the highest frequency of $\sim$ 0.1 THz and magnetic fields up to 6 T) appears considerably limited. The use of such one-frequency spectrometers becomes rather inefficient when studying magnetic systems with a large zero-field splitting, complex frequency-field diagrams of magnetic excitations, or materials with field-dependent ESR parameters (g-factor, line-width, etc.). Multi-frequency ESR techniques (employing several frequencies) combined with high magnetic fields allow for more detailed studies of magnetic excitation spectra in such systems. If the frequency of a spectrometer can be tuned continuously or stepwise within a certain frequency range, the term „tunable-frequency ESR spectroscopy“ can be applied. The tunable-frequency ESR has a broad range of applications in solid-state physics, materials science, and chemistry (see for instance Ref. [1–7]).

As technique, ESR spectroscopy is based on the detection of resonance absorptions of electromagnetic radiation corresponding to transitions between electron-spin energy levels split by internal effects (crystal-field effects, exchange interactions, etc.) and/or by an applied magnetic field. The strength of such interactions in magnetic materials can vary from tenth of microkelvin to hundreds and even thousands of Kelvin (which corresponds to a frequency range from the MHz region to hundreds of THz). That is why extending the frequency range of ESR techniques up to the THz range appears to be one of the central issues in modern ESR spectroscopy.

Most of the work presented in this thesis has been done using a transmission-type tunable-frequency ESR spectrometer. The spectrometer

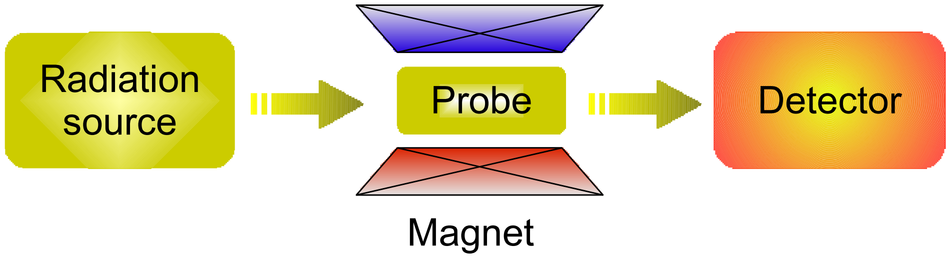

Figure 2.1.: *Schematic drawing of the transmission-type ESR spectrometer.*

is equipped with a 16 T superconducting magnet. A schematic diagram of a typical transmission-type ESR spectrometer is shown in Fig. 2.1. It consists of a radiation source, radiation detector, magnet, and the probe. A variety of radiation sources (Backward Wave Oscillators, Gunn- and VDI-diodes, microwave network analyzer MVNA) covering the frequency range from 50 GHz to 1.4 THz are available in ESR measurements. In addition, a pulsed-field ESR spectrometer has been designed and built. This pulsed-field spectrometer allows performing ESR experiments in pulsed fields up to 63 T and beyond using standard radiation sources (Gunn- and VDI-diodes) and a free electron laser (FEL) at frequencies up to 75 THz.

The remainder of this chapter is organized as follows. In sections 2.2 and 2.3, an overview of the millimeter- and submillimeter-wave radiation sources and detectors used for ESR experiments is presented. Section 2.4 introduces the magnets employed for ESR measurements. In section 2.5, a description of the ESR probes used are given.

2.2. Millimeter- and submillimeter-wave radiation sources

The broad frequency range of radiation required for tunable-frequency high-field ESR demands several types of radiation sources. These sources should generate monochromatic radiation with high output power and low noise, be stable and easy to operate. They should allow stepwise and continuous frequency tuning over a certain range, suitable for tunable-frequency ESR spectroscopy. It is important to mention that the output power of the majority of these devices significantly drops approaching the THz frequency range (down to some hundreds and even tens of μW) imposing serious restrictions for a sufficient ESR resolution in this frequency range. Due to the lack of

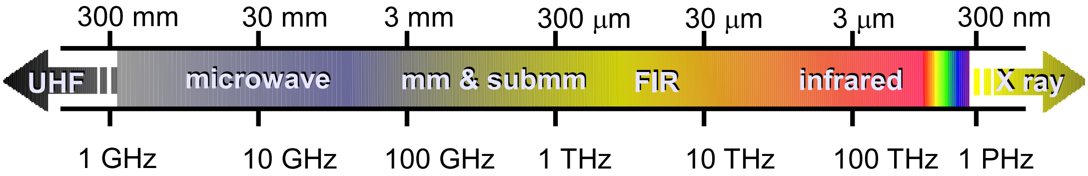

Figure 2.2.: *The frequency (wavelength) scale of the electromagnetic radiation.*

stable and intensive sources of electromagnetic radiation the frequency range between 300 GHz and 3 THz is known as the „THz gap“(Fig. 2.2). The present work has been done using a variety of radiation sources including vacuum sources of radiation (Backward Wave Oscillators and free electron laser), and semiconductor radiation sources (Gunn- and VDI-diodes, microwave network analyzer MVNA), quasi-continuously covering the frequency range from 50 GHz to 75 THz.

2.2.1. Vacuum radiation sources

Backward wave oscillators

Backward Wave Oscillators are classical electron-gun vacuum-tube microwave generators, possessing two important distinguishing abilities: to generate very short wavelengths (down to $\lambda \sim 0.2$ mm), and to electronically tune the working frequency in a broad range, up to ±30% from the central value. The operating frequency is determined by the periodicity of the BWOs slow-wave structure and the cathode voltage. The latter can be easily changed providing a fast and convenient way of tuning frequency.

The working principle of BWOs is based on the Smith-Purcell effect. Electron are traveling close and parallel to a metallic reflection grating (called slow-wave structure). An interaction of the traveling electron beam with the grating, a radiation known as Smith-Purcell radiation is produced. The virtual photons of the electron field are scattered by the grating, and the wavelength λ of the radiation is

$$\lambda = \frac{L}{m\beta}(1 - \vec{\beta} \cdot \vec{n}) \, ,$$

where L is the grating period, $\vec{\beta} = \vec{v}/c$ is the electron velocity in the unit of speed of light c, $\vec{n}$ is the unit vector along the emission direction, and m is the spectral order [8, 9]. In turn, this radiation resonantly interacts with the electron beam, when the phase velocity of the electromagnetic wave matches with the electron velocity. In BWOs the group velocity direction is opposite to

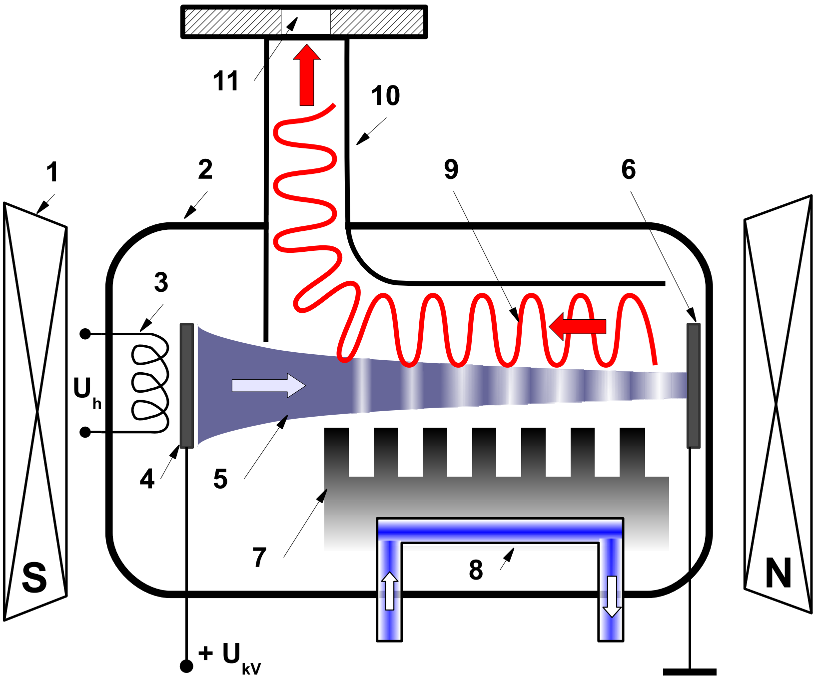

Figure 2.3.: *Schematic view of a BWO: 1 - magnet, 2 - vacuum jacket, 3 - heater, 4 - cathode, 5 - electron beam, 6 - anode, 7 - slow-wave structure, 8 - water cooling, 9 - electromagnetic back wave, 10 - rectangular waveguide, 11 - window.*

the phase velocity of the the electron beam (i.e., the angle between the vectors $\vec{n}$ and $\vec{\beta}$ is 180 deg). If the electron-beam current exceeds a certain threshold level (known as start current), this interaction results in nonlinear bunching of electrons in the beam, which amplify the Smith-Purcell radiation. Due to the built-in feedback mechanism, such system operates as an oscillator producing relatively high output power even without a resonator.

A schematic view of a BWO is shown in Fig. 2.3. All the elements are built in a metal vacuum jacket (2) placed in a magnetic field (1), which serves to collimate the electron beam inside the tube. If the heater (3) is switched on, the cathode (4) emits electrons (5) which, accelerated by a high-voltage electrical field, travel in vacuum toward the anode (6) (collector). The electrons pass over a comb-like slow-wave structure (7) interacting with it. During this process kinetic energy of the electrons is transferred into an electromagnetic field. A slow-wave structure with a grating period $L \approx 100 - 200\ \mu$m is used. To remove thermal heat [which is of particular importance for high-frequency BWOs (above 160 GHz)] a water-cooling system (8) is used. The magnetic field has to be high and homogeneous enough to guarantee that

Figure 2.4.: *The packetized (left) and an unpacketized (right) BWO.*

only a fraction of the electrons hits the slow-wave structure. The radiation leaves the metal jacket through an oversize waveguide (10) terminated by a quartz window (11). BWOs are highly sophisticated devices, working at extremely intensive conditions (with a voltage up to 6 kV, high temperature of the cathode - up to 1200 °C, and at high vacuum - down to 10^{-7} mbar).

Two types of BWOs sources [containing its own magnet (packetized) and without it (unpacketized)] are shown in Fig. 2.4. Low-frequency BWO-based radiation sources ($f \lesssim 180$ GHz) are packetized, employing small permanent samarium-cobalt magnets. For operation of high-frequency BWOs ($f \gtrsim 180$ GHz) stronger magnetic fields are required, which can be produced by a special permanent magnet system with a field up to 1.3 T (in a gap of 3.2 cm). Using a high-precision mechanical adjustment system, BWOs can be adjusted by rotating them around two axes - one is directed along the waveguide and another one orthogonal to the waveguide and to the direction of magnetic field. Typical requirements on the adjustment are alignments of about 1 deg or better.

Both the frequency and the output intensity of the BWOs is a function of the applied acceleration voltage (cathode voltage). The output frequency f is determined by the cathode voltage, $f \propto U^{3/2}$. The frequency can be adjusted within $\pm 20 - 30\%$ from the central frequency electronically, by tuning the cathode voltage U. The output power vs voltage (the BWO's spectral pattern) has a more complex dependence, which is unique for each BWO. In order to produce radiation power of high stability, BWOs should be fed using a very

Name	Frequency range GHz	Power mW		Name	Frequency range GHz	Power mW
ov 69	34-55	20		ov 32	233-547	3
ov 70	50-80	15		ov 81	490-859	4
ov 56	50-81	20		ov 80	524-694	4
ov 71	78-119	20		ov 83	682-1099	5
ov 86	113-178	40		ov 82	720-991	1.5
ov 87	117-177	30		ov 84	870-1229	2
ov 24	163-260	30		ov 85	1006-1422	1
ov 30	154-379	23				

Table 2.1.: *A summary of parameters of the BWO set available at the HLD. Power means a average power of the output radiation produced by BWO.*

stable power supply (with a jitter of less than $\Delta V/V \approx 10^{-5}$). Water cooling keeps the BWOs at a temperature of $\sim$ 19 °C preventing frequency fluctuations due to the thermal expansion of the slow-wave structure.

A set of BWO-based radiation sources covering the frequency range from 53 to 1400 GHz is available at the HLD. These BWOs are manufactured by ISTOK Research and Development Company (Fryazino, Russia). The spectral range and nominal output power are shown in Table 2.1. The manufacturer specifies only the average power for each BWO, whereas the output power strongly varies over the frequency range (Fig. 2.5).

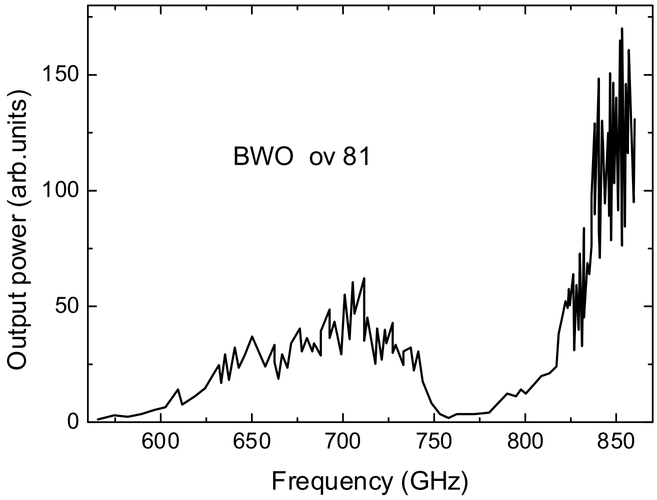

Figure 2.5.: *A typical output power vs frequency dependence of a BWO.*

Free electron laser FELBE

The first attempt to combine a FEL and pulsed magnetic fields was made using the FELIX radiation source at Rijnhuizen [10–13]. It is worth to mention that in contrast to radiation produced by conventional sources (for instance, BWOs or Gunn diodes) used for continuous-wave (cw) ESR spectroscopy, the radiation produced by FELs has a pulse structure with a typical pulse duration of the order of microseconds (in case of electrostatic or van de Graaf accelerators) or picoseconds (linear accelerator, hereafter linac). Due to the bandwidth-limited (or sometimes called Fourier-limited) pulse nature, the FEL radiation is not ideally monochromatic, particularly in case of linac-based FELs. Furthermore, the FEL pulse power can reach hundreds of kW/cm^2, which might lead to a number of parasitic effects, including for instance overheating of the sample and even its destruction as result of ionization defects. Effects of optical bleaching under the influence of high-power FEL radiation were reported for InAs/GaSb [10] and InAs/Al$_x$Ga$_{1-x}$Sb [14] structures, opening new opportunities in the so-called saturation spectroscopy [15] but, on the other hand, demonstrating a potential problem when employing high-power pulsed radiation produced by FELs for the conventional „low-power" spectroscopy.

FELBE is the acronym for the free-electron laser facility at the superconducting Electron Linear accelerator of high Brilliance and Low Emittance (ELBE) located at the Forschungszentrum Dresden-Rossendorf (FZD). There are two FELs at the FZD. Both of them are Compton FELs working in the upper region of the low-gain regime ($G \sim 10 - 80\%$) [16]. A mid-infrared (IR) FEL (undulator U27) can be operated in the wavelength range of 4 - 22 μm [16], using an electron-beam energy varying from 15 to 35 MeV. In August 2006, the installation of the long-wavelength FEL (undulator U100)

Parameter	**U27**	**U100**
Undulator period (mm)	27.3	100
Number of periods N$_u$	2x34	38
Undulator parameter K$_{rms}$	0.3 - 0.7	0.5 - 2.8
Wavelength (μm)	4 - 22	18 - 250
Pulse durations (ps)	0.9 - 4	5 - 30
Max. pulse energy (μJ)	2	5
Max. aver. power (W)	30	65

Table 2.2.: *FEL specifications*

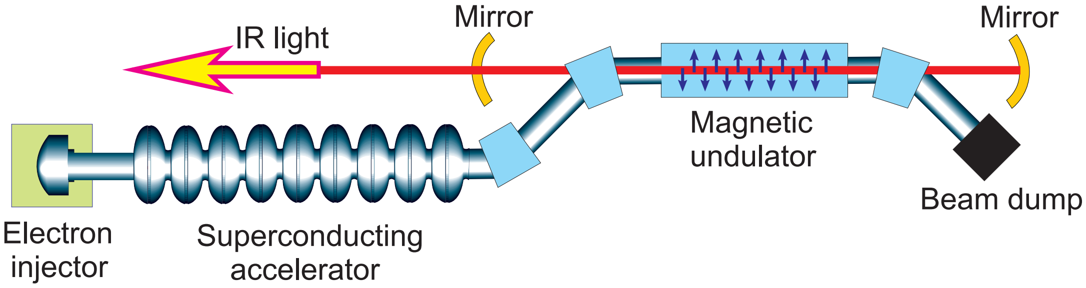

Figure 2.6.: *Schematic view of one of the FELs used at the FZD.*

has been completed and the first FEL lasing in the far-IR range was achieved [17]. In Table 2.2, parameters of both FELs are summarized.

Equipped with a partial-waveguide resonator [18] the undulator U100 covers the wavelength range from 18 to 250 μm. Thus, the combination of two FELs allows to quasi-continuously cover the wavelength range from 4 to 250 μm. The pulse energy (≤ 5 μJ) depends on the radiation wavelength, electron-beam energy, and resonator and undulator parameters. Driven by a superconducting linac, FELBE continuously generates IR radiation pulses with a repetition rate of 13 MHz. The possibility to operate in a quas-cw regime is one of the most important advantages of FELBE. This regime is of particular importance for pulsed-field ESR (with a typical magnetic field-pulse duration from 10 ms to some hundreds of ms), allowing to avoid complex problems of synchronization of FEL radiation and magnetic-field pulses, permitting longer acquisition times and thus better signal-to-noise ratios. In addition, operation in macropulse (macrobunch duration ≥ 100 μs, repetition rate ≤ 25 Hz) as well as single-pulse modes are possible. High-level linear polarization of the FEL radiation ($\approx 98\%$) was confirmed experimentally [19].

The FELs at the FZD consist of the following main parts: a superconducting accelerator (equipped with electron injector, beam lines, and beam dumps), magnetic undulator, and optical resonator (Fig. 2.6). The electron beam (with up to 1 mA beam current at 35 MeV) is produced by a radiofrequency (RF) linear accelerator. The RF power comes from 10 kW clystrons controlled by a low-level RF system. Electrons are preaccelerated in a 250 keV thermionic DC electron gun and prebunched in a two-stage RF buncher section. The main acceleration is achieved in two 20 MeV - 1.3 GHz linear accelerator modules equipped with cavities made from superconducting Nb and cooled to 1.8 K. Apart from driving the FELs, the accelerator can be used for generating various kinds of secondary radiation (x-rays, positrons, neutrons, and Bremsstrahlung) [20].

The wavelength of the FEL radiation, λ_n, is determined by the electron energy γ (in units of the electron rest mass), the undulator parameter K_{rms} (rms = root mean square), and the undulator period λ_U (n is the radiation harmonic number):

$$\lambda_n = \frac{\lambda_U(1 + K_{rms}2)}{2n\gamma 2} \, . \tag{2.1}$$

The dimensionless undulator parameter K_{rms} is given by

$$K_{rms} = \frac{eB_U\lambda_U}{2\pi m_e c} \, , \tag{2.2}$$

where e and m_e are the electron charge and mass, respectively, and B_U is the rms amplitude of the magnetic field on the undulator axis. The undulator parameter can be varied by changing the undulator gap which determines the magnetic field along the undulator axis. The wavelength ranges of the U100 and U27 undulators as a function of a kinetic electron energy, E_e^{kin}, calculated for different K_{rms} are shown in Fig. 2.7. The measured output power vs wave-

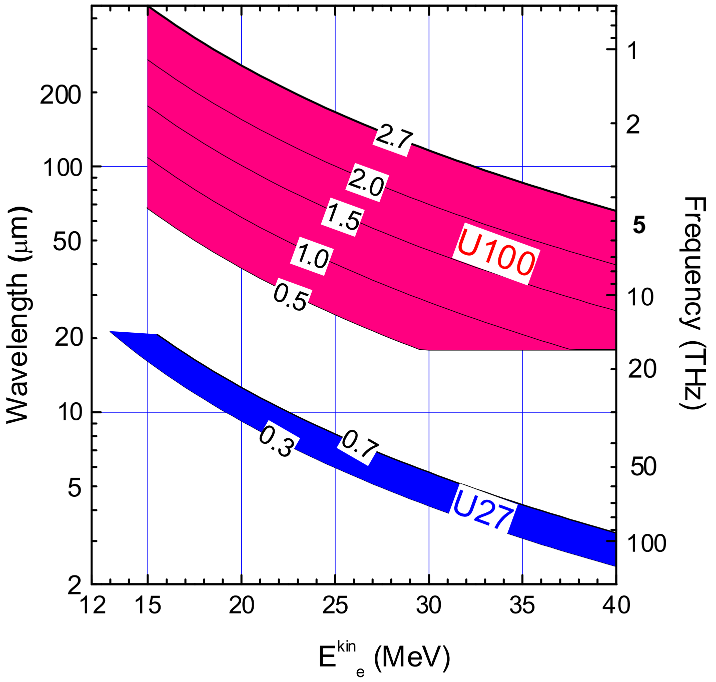

Figure 2.7.: *The wavelength (frequency) range of the U27 and U100 undulators as a function of the kinetic electron energy,* E_e^{kin}*, calculated for different undulator parameters* K_{rms}*.*

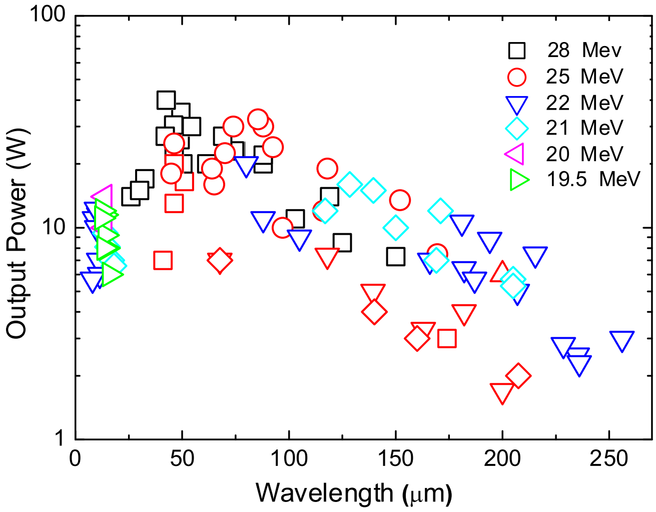

Figure 2.8.: *Typical measured output power vs wavelength for the two undulators, U27 ($\lambda < 20$ μm) and U100 ($\lambda > 20$ μm), for different kinetic electron energies (user statistics for the years 2008 and 2009).*

length for the undulators U27 and U100 at different kinetic electron energies (determined from the user statistics for the years 2008 and 2009) is shown in Fig. 2.8.

The undulator is the „heart“ of an FEL. A schematic view of the U100-based FEL (without accelerator section) is shown in Fig. 2.9. The undulator U100 contains 38 sections of Sm/Co magnets and magnet poles (made from soft high-permeability decarbonized iron) with a period of 100 mm (this parameter defines the name of the undulators, i.e., U100 or U27). Such periodicity makes it possible to achieve sufficiently high magnetic fields in a reasonably sized undulator gap. The magnetic field alternates along the undulator axis with a period λ_U wiggling the electron beam in a direction perpendicular to the undulator axis and the magnetic-field vector. Due to the transverse modulation the electrons emit light. Another important component of FELs is the optical resonator, which for U100 consists of a bifocal upstream and a cylindrical downstream mirror. The distance between the two mirrors, $L_R = 11.53$ m, is determined by the repetition rate of the electron pulses (13 MHz) coming from the accelerator, and chosen to secure an effective coupling between the electron beam and the oscillating wave in the resonator. The undulator U100 is equipped with a partial parallel-plate waveguide (7.92 m long, 10 mm distance between the plates), confining the IR beam in the vertical (transverse) direction, increasing the laser gain and allowing a smaller undulator gap

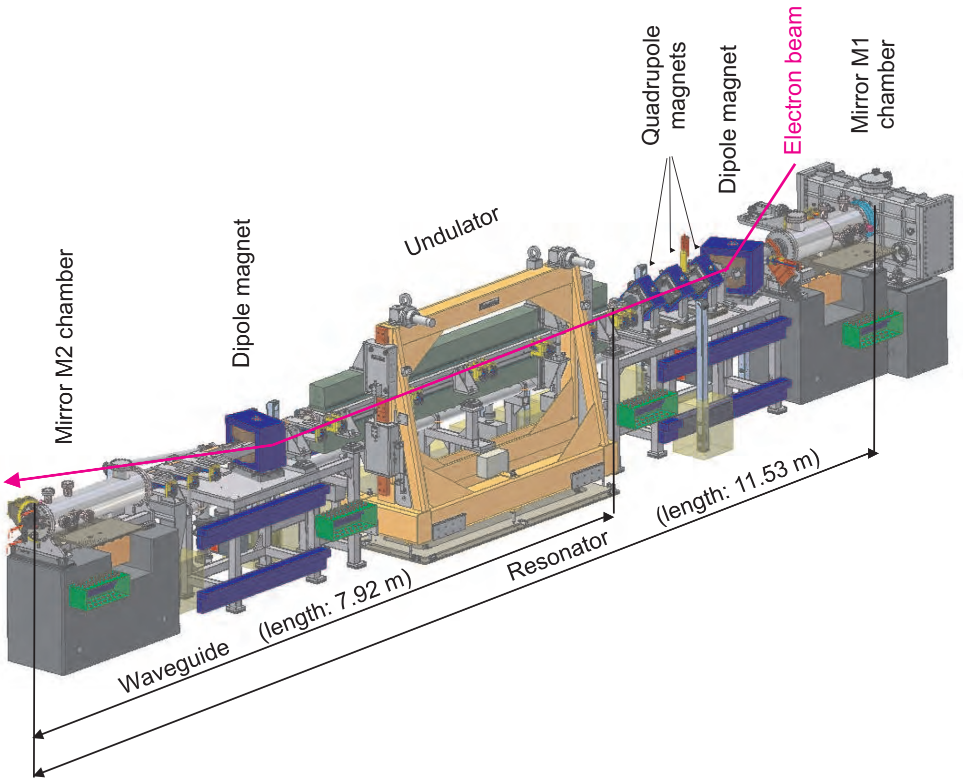

Figure 2.9.: *Schematic view of the U100-based FEL. The electron beam enters the FEL from the right side.*

(i.e., a higher modulation field). Because of the large variation of the beam radius determined by the radiation wavelength and expected laser gain, outcoupling holes of different diameters (2, 4.5, and 7 mm for U100) are used. The appropriate mirror can be shifted into the right position by using a high-precision linear translation stage.

The undulator U27 has been designed for a shorter wavelength range (4 to 22 μm). It is equipped with two planar undulator units with a length of 0.98 m each. Each unit contains 34 sections of NdFeB magnets with alternating poles with a period of 27.3 mm. In contrast to U100, the undulator U27 is not equipped with a waveguide; instead just an open optical resonator ($L_R = 11.53$ m) consisting of two spherical mirrors is used. To optimize the extraction ratio over the whole wavelength range, mirrors with different outcoupling hole sizes (1.5, 2.0, 3.0, and 4.0 mm) are used. The mirrors are mounted on a wheel which is fixed on a high-precision rotation stage.

The resonator length can be adjusted and stabilized using a Hewlett-Packard interferometer system. A separate beamline guides the IR beam to a diagnostic station. The radiation wavelength is measured using a Czerny-Turner-type spectrometer, which contains a turret with three different gratings to cover the wavelength range from 4 to about 230 μm. A standard Bruker Equinox 55 Fourier-transform spectrometer is used for measuring the spectral radiation parameters at wavelengths up to 250 μm.

From the diagnostic station, the beam is guided to user laboratories. For this purpose, gold-coated copper and stainless-steel mirrors are used. The reflectivity of the mirrors (with a surface roughness being better than 0.2 μm) is larger than 98.8% in the entire wavelength range. The IR beam is fed through a 27 m long tunnel to the adjacent HLD building. The FELBE-HLD beamline contains 13 mirrors (with effective diameters ranging from 100 to 200 mm). To reduce the number of mirrors to a minimum, some mirrors are used for beam deflection as well as for refocusing. To avoid the absorption of IR light by air, the beam has to be guided in pipes which are either evacuated or constantly purged with dry nitrogen gas. The power attenuation by the beamline is 3 - 10 dB and depends strongly on the radiation wavelength and used windows. If additional attenuation is required, the beam power can be reduced by 3 - 38 dB using an optical attenuator located at the diagnostic station. High-level linear polarization of the FEL radiation (better than 95%) after the propagation through the beamline was confirmed experimentally. Further details of the beamline are described in Ref. [21].

The pulse length of the FEL radiation and the spectral distribution of the power was measured by means of an autocorrelator and a spectrometer, respectively [22]. The resulting time-bandwidth product indicates the Fourier-transform-limited operation of both FELs. The radiation pulse length can be changed by a factor of about 5 by detuning the resonator with respect to its nominal length determined by the electron-bunch repetition rate. As confirmed experimentally, the spectral width of the produced radiation varies by the same factor. An example of the spectral distribution of the FEL power and the corresponding Gaussian line-shape fit for a wavelength of 188.8 μm is shown in Fig. 2.10. In this example, the full spectral width at half maximum, $\Delta\lambda/\lambda$, of the FEL radiation is 0.8%. This parameter can be changed continuously, depending on experimental requirements, approximately from 0.4 to 2%.

The FEL-based radiation source is a promising technique for the broad range of applications. Due to the high radiation power, the FEL light is attractive for the investigation of numerous non-linear effects in solids: higher-order harmonic generation, above-threshold ionization, ponderomotive potential effects, etc. (see for instance [23–25]). Finally, due to the

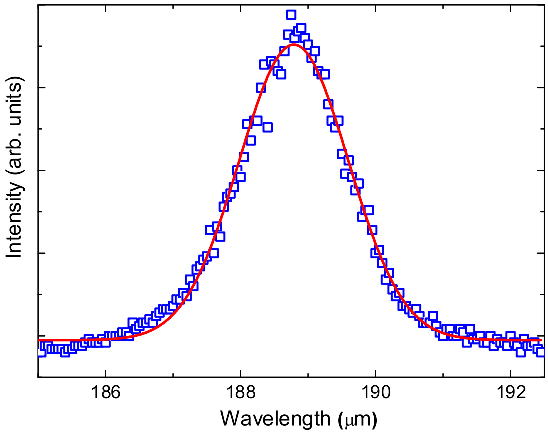

Figure 2.10.: *Example of the spectral distribution of the FEL power (symbols) and the corresponding Gaussian line-shape fit (line) for a wavelength of 188.8 μm. The full spectral width at half maximum, $\Delta\lambda/\lambda$, is 0.8%.*

extraordinary high brightness and tunability, FEL can be successfully used as an optical source for scattering scanning near-field optical microscopy and spectroscopy [26,27].

2.2.2. Solid-state radiation sources

Multiplier chain system VDI

Solid-state microwave generators discussed here represent the second type of radiation sources used in high-field ESR spectroscopy. They are reliable, compact, have low power consumption, and are simple in operation. They can be operated in combination with frequency multiplyers, which allows to cover the frequency range up to a few hundred GHz. Recently, based on integrated planar GaAs Schottky-diode circuits, Virginia Diodes Inc. has developed a series of broadband frequency multipliers with high transformation coefficient. Virginia Diodes Inc. have designed a multiplier chain system (hereafter VDI), schematically shown in Fig. 2.11. This setup generates radiation with high output power (Table. 2.3) and can be easily tuned electronically.

VDI is driven by the yttrium-iron-garnet (YIG) source generating microwave frequencies. YIG is a ferrite material that resonates at a microwave frequency, that can be changed by the application of a magnetic field. The resonance frequency is directly proportional to the applied field. The oscillator contains a tiny YIG sphere, fixed inside a two-coil electromagnet. The main

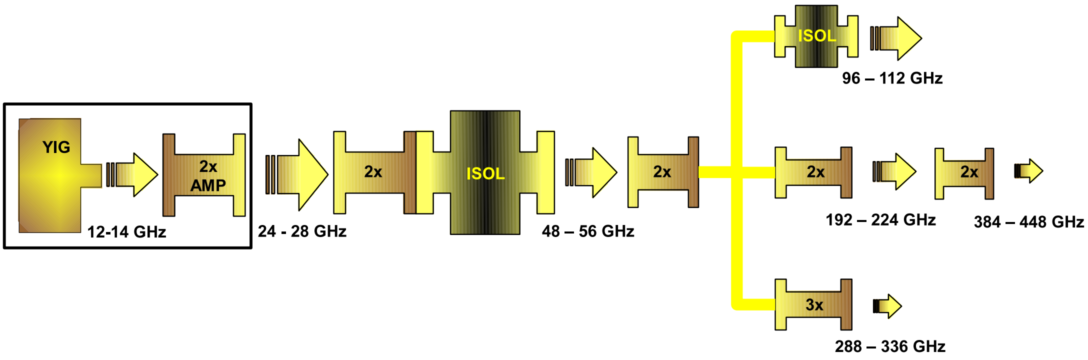

Figure 2.11.: *Schematic sketch of VDI microwave sources.*

coil of the magnet is used for frequency tuning by changing the applied current. The second coil is used to stabilize the output frequency. A specially designed resonant circuit extracts energy from the sphere. YIG has its best performance when the temperature is kept constant, requiring a good temperature stability. In recent years, due to the progress in YIG technology, several lines of YIG - tuned oscillators with high power (up to 100 mW), low phase noise (-130 dBc/Hz offset 100 kHz), large frequency range (6 to 20 GHz), and moderate tuning speed became available.

The frequency of the VDI system can be tuned using a TTL control within the frequency range of 12 - 14 GHz with a 100 MHz stepwidth. Microwave radiation generated by the YIG oscillator ($\approx$ 20 mW) is amplified by an active doubler, producing an output power of ca. 1 W for further multiplication. Typical output-power-frequency dependences of VDI-diode-based microwave sources are shown in Fig. 2.12. Each multiplication reduces the

Frequency range GHz	Output power (maximal) mW
24 - 28	1460
48 - 56	475
96 - 112	115
192 - 224	26
288 - 336	4
384 - 448	3.2

Table 2.3.: *VDI millimeter- and submillimeter-wave sources used in ESR experiments.*

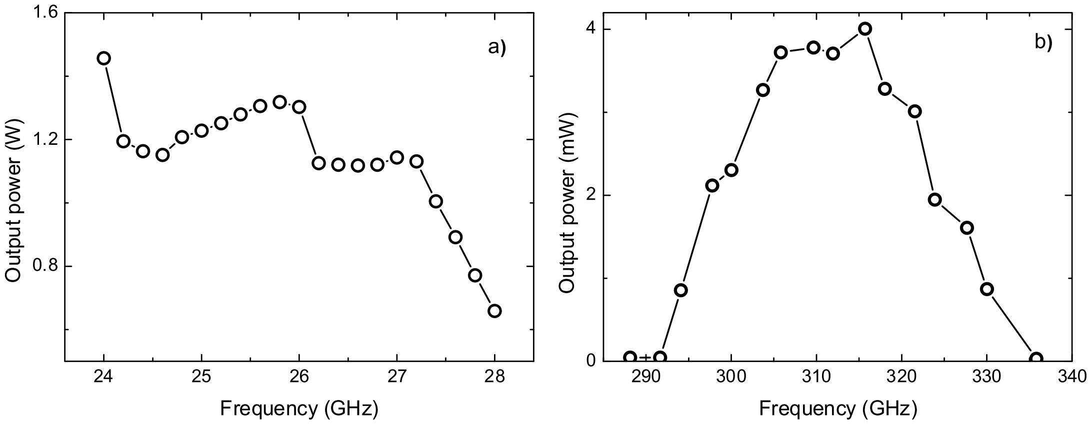

Figure 2.12.: *Spectral output-power distribution in the frequency range* 24 − 28 *GHz (a) and after a 12 times frequency multiplication (b).*

output power, even more at the spectral wings than at the central frequency, resulting in a peak-like shape of the spectral-power distribution. To prevent the reflection of the radiation from the load to the microwave generator, Faraday isolators are placed after the multipliers with central frequencies of 52 and 104 GHz (Fig. 2.11). Based on the Faraday effect in ferrite, these devices significantly improve the frequency stability. The generated frequency can be tuned within each band by changing the fundamental YIG oscillator frequency from 12 to 14 GHz. The VDI radiation source (Fig. 2.13) produces high-quality radiation of an excellent spectral purity, frequency and power stability, and low noise.

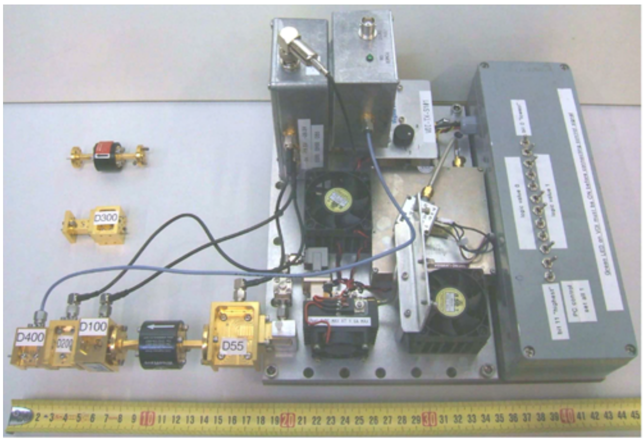

Figure 2.13.: *Photograph of the VDI radiation source available at HLD.*

Gunn diode

Gunn diodes (Fig. 2.14) are another solid-state radiation source used in ESR experiments. Gunn diodes are highly reliable devices with practically no restrictions in lifetime. Small size, light-weight, and small voltage-bias requirements make them superior to the electron-gun vacuum-tube generators. Besides applications in experimental science, Gunn diodes are extensively used as a local oscillator in radar-related applications and communication systems.

The operation of a Gunn diode is based on the transferred electron phenomena, which takes place in highly *n*-doped GaAs layers with multi-valley structure in their conduction band. For the radiation generation, the device should be operated in a regime with a negative differential resistance in the voltage-current dependence. Such behavior is found to be associated with the carrier transfer from a high-mobility (low effective electron mass at the central valley) to a low mobility edge (high effective mass at a satellite valley). Because of the difference in the mobility, the fast moving electrons get slowed down and form a mobile domain (comprising accumulation/depletion of electrons). The domain normally nucleates at the cathode end and after traversing the whole length of the sample, annihilates at the anode giving a current spike. A new domain is again nucleated and the cycle is repeated. The active element should be placed in a cavity or resonant circuit, which drastically increase the efficiency of the generation process.

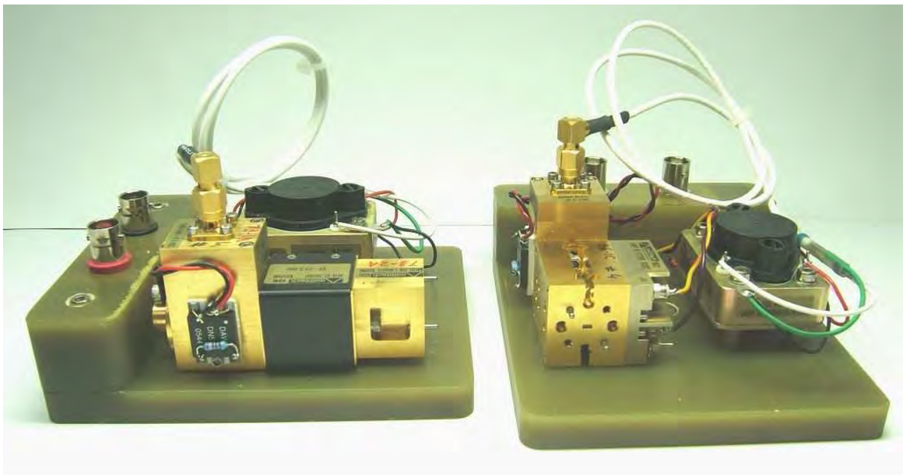

Figure 2.14.: *Photographs of the Gunn diodes available at the HLD.*

Frequency GHz	Output power mW
73.3	40
85	52
96	40
146.6	1.8
192	3.5
219.9	1.8
288	1.5

Table 2.4.: *Frequency and output radiation power of the Gunn oscillators available at the HLD.*

The fundamental frequency f of a Gunn oscillator is inversely proportional to the domain transit time, τ, across the active length, L^{eff}, so $f \propto 1/\tau = V/L^{eff}$, where V is the velocity of the domain (for GaAs it is about $1 \cdot 10^5$ m/s and depends on the applied voltage). Each Gunn diode is designed for a particular frequency. Its properties are determined by a few parameters (including, the layer thickness, carrier concentration, and device geometry). In the present study a set of the Gunns diodes and multipliers producing microwave radiation with frequencies shown in Table 2.4 was used.

Millimeter-wave vector network analyzer

A millimeter-wave vector network analyzer (MVNA, product of „ABmm“, France) can be used in ESR experiments covering the frequency range from 8 GHz to approximately 1 THz. The photograph of the MVNA available at HLD is shown in Fig. 2.15. In this device the Schottky diode is used as a harmonic generator producing radiation with a frequency

$$F_{GHz} = N_1 F_1 \ ,$$

where N_1 is an integer number and F_1 is the tunable frequency generated by an internal source S_1 (YIG oscillator with frequency range of $8 - 18$ GHz). The radiation is detected by a second Schottky diode used as a harmonic mixer. This Schottky diode converts the high-frequency signal F_{GHz} down to a low frequency F_{MHz} by mixing it with a frequency $N_2 F_2$,

$$F_{MHz} = |N_1 F_1 - N_2 F_2| \ ,$$

where F_2 is the frequency generated by the second source S_2, and the integer N_2 is the harmonic rank determined by the harmonic mixer. Then, a narrow-

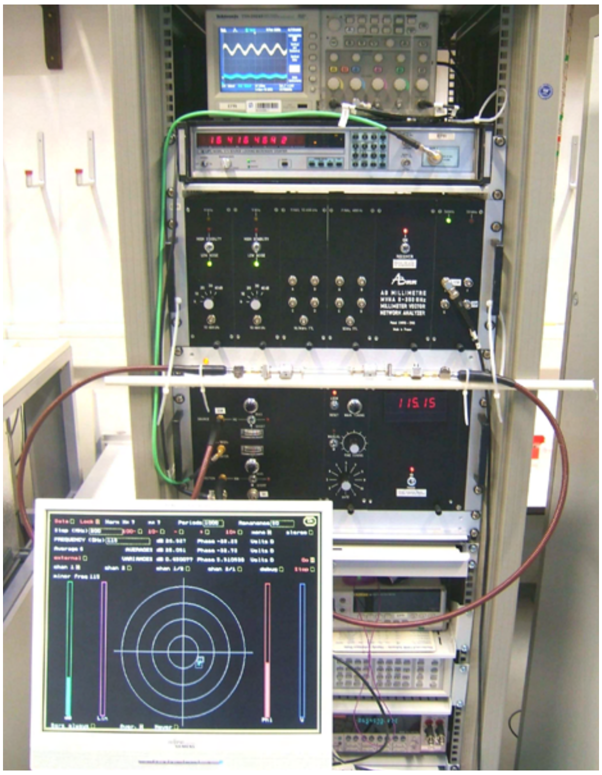

Figure 2.15.: *Photograph of the MVNA radiation source available at HLD.*

band heterodyne vector receiver registers both the amplitude and phase of the beat frequency F_{MHz}. The amplitude of the MHz signal is proportional to the amplitude of the high-frequency signal used in experiment, while its phase preserves the phase of the F_{GHz} relative to the local oscillator S_2. The phase noise of the MHz signal is

$$\varphi_{low} = |N_1\varphi_1 - N_2\varphi_2| \ ,$$

where φ_1 and φ_2 are a phase noise associated with the frequency F_1 and F_2, respectively.

Such signal detection becomes efficient, when the same harmonic ranks are chosen, $N_1 = N_2$, and the sources S_1 and S_2 are phase locked and produce the identical phase noise, $\varphi_1 = \varphi_2$. If these conditions are accomplished, the phase noise is avoided and the frequency F_{MHz} is equal to the frequency difference between the sources S_1 and S_2 multiplied by the harmonic rank N. The frequencies F_1 and F_2 are selected so that the detection frequency is 9 MHz (or 34 MHz for N>4). The phase lock between S_1 and S_2 provides the high sensitivity to the phase changes in F_{GHz}.

Band	Harmonic	Frequency GHz	Output power mW
Q	3	29 - 50	5
V	4	42 - 72	1
W	5-6	70 - 110	12
D	7-8	110 -142	1-9

Table 2.5.: *Frequency bands provided by the MVNA.*

Using different pairs of Schottky diodes it is possible to generate any frequency in the range from 8 to 200 GHz. Typical frequency bands available when using the MVNA are shown in Table 2.5. In order to reach higher frequencies, different extensions are required. The External Source Association option additionally permits the connection with a higher-frequency Gunn-diode source, providing enhanced signal-to-noise characteristics in the 150 - 250 GHz range, as well as measurements up to 700 GHz. A big advantage of the MVNA compared to other devices is that it allows not only to tune the frequency, but also to control and monitor the phase.

2.3. Far-infrared detectors

Far-infrared detectors are used to transform the power of the millimeter- and submillimeter-wave radiation to an electrical signal. There is a number of far-infrared detectors, such as photoconductor, pyroelectric, drag detectors, hot-electron bolometers, Schottky diodes, and quantum-well devices [28]. The usefulness of each detector is determined by several parameters: the frequency range, sensitivity, and response time. Because of their fast response and high sensitivity, a hot-electron n-InSb bolometer is of particular importance for high-field ESR experiments. The detector is operated at liquid-helium (LHe) temperature, allowing to significantly increase the signal-to-noise ratio.

Indium antimonide (InSb) is a III-V semiconductor with high intrinsic electron mobility and small effective mass ($m^* = 0.014\ m_e$) and the smallest band gap (0.17 eV at RT) of all binary III-V compounds. Relatively easy growth conditions allow to achieve good-quality large-area homogeneous crystalline layers on various substrates. The following absorption mechanisms are of importance for the FIR detection in semiconductors [29]: intrinsic and extrinsic photoconductivity as well as free charge carriers and their response on an applied magnetic field (Fig. 2.16). In case of the intrinsic photoconductivity, photons of sufficient energy produce transitions between the valence and

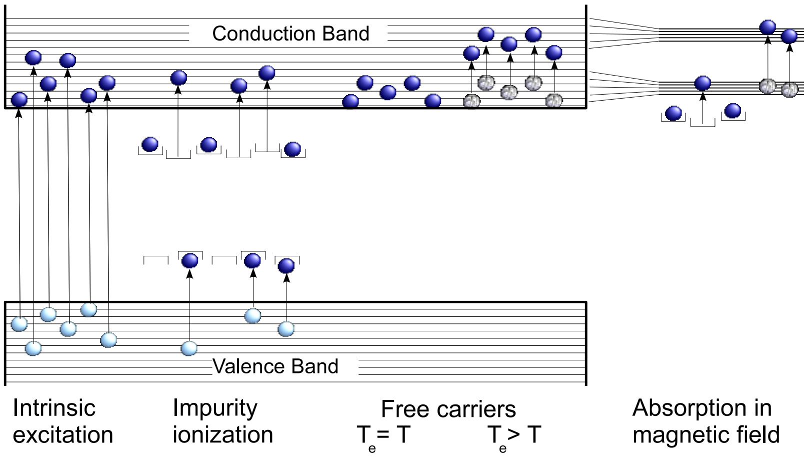

Figure 2.16.: *An example of the photoconductive mechanism responsible for the absorption of radiation in semiconductors.*

conduction band of a semiconductor, creating free electrons and holes. Because these transitions occur at frequencies above the threshold energy [equal to the gap between the conduction and valence bands ($\sim$ 43 THz or for wavelengths below $\sim$ 6 μm for InSb)], this mechanism is out of interest for the millimeter- and submillimeter-wave range.

In case of the extrinsic photoconductivity, transitions from the donor-impurity states to the conduction band are important. The impurity ionization energy is much smaller than that of the intrinsic energy gap, that is why this mechanism allows detection of radiation at a much longer wavelength (40 - 120 μm for a Ge-doped Ga detector). In case of a hot-electron InSb bolometer (which almost always contain hydrogenic impurities) the the Bohr radius of the impurity ground state is large $\sim$ 60 nm, resulting in an effective interaction between the hydrogenic centers and causing metallic behavior of a such material. Even the purest InSb crystals contain uncontrolled impurity with a concentration of about 10^{14} cm^{-3}. The best sensitivity of the Ga:Ge and n-InSb detectors can be achieved only at liquid-helium temperatures, when the coupling between the the carriers and lattice becomes very weak. The radiation absorption changes the effective electron temperature and mobility of carriers increased, $\mu \sim T^{3/2}$, resulting in a change of the conductivity. Interestingly, since at long wavelengths the free-electron absorption is maximal and independent on the wavelength, hot-electron bolometers do not have a long-wave threshold since. Fast response time is determined by the electron-lattice relaxation and is about 300 ns. Below 500 μm the electron absorption efficiency falls rapidly (Fig. 2.17) reducing the detector performance. Such reducti-

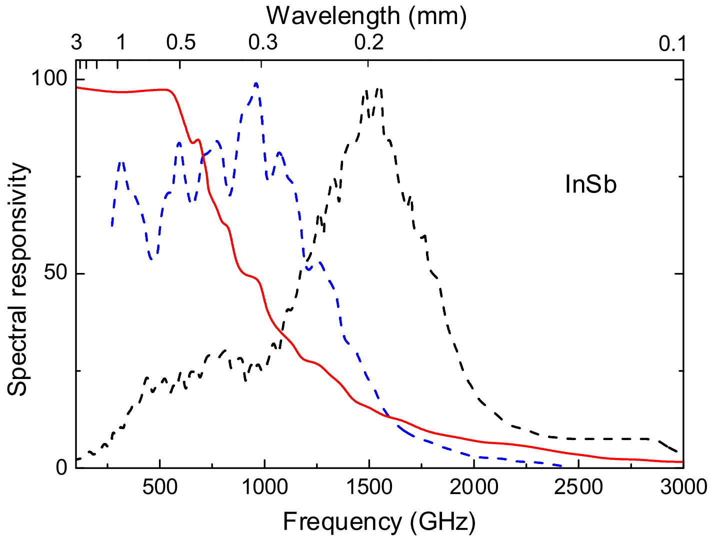

Figure 2.17.: *Spectral response of n-InSb detectors used in ESR experiments at different magnetic fields. Red, blue, and black lines represent the spectral response of the detector in typical magnetic fields of 0, $\sim$ 0.4, and $\sim$ 1 T, respectively.*

on can be explained by the classical Drude conductivity and some photon-phonon-electron processes reducing the detector response below 200 μm.

The spectral range of n-InSb bolometers can be extended using a magnetic field. The magnetic field decreases the Bohr radius of impurity states, reducing the interaction between them. A field of $\sim$ 0.4 T reduces it so much that discrete impurity levels are situated now below the conduction band. The ionization energy depends upon the magnetic field and the purity of the sample. This type of detector, known as the Putley detector, has significant advantages over ordinary electron bolometers. Such a detector still operates as an electron bolometer (but with somewhat reduced performance) at very long wavelengths, while significantly improving the efficiency below 500 μm (blue, dashed curve in Fig. 2.17).

Application of higher magnetic fields splits the conduction band of InSb into Landau levels; in such a case the radiation detection is determined by cyclotron-resonance transitions between the Landau levels. The resonance frequency can be tuned by magnetic field. A broader spectral response can be achieved using an inhomogeneous magnetic field. Transitions within the impurity levels can play also an important role (in particular in magnetic fields above 0.5 T), extending the spectral response of such a detector down to 100 μm.

Figure 2.18.: *The InSb detector used in ESR experiments at HLD.*

In our ESR experiments, both types (standard and magnetically-detuned) of such liquid-He cooled InSb hot-electron bolometers (product of „QMC Instrument Ltd") were used. The n-InSb detector we used is shown in Fig. 2.18. Spectral ranges of theses detectors are shown in Fig. 2.17. These detectors have a high detection sensitivity (≈ 4 kV/W at $\lambda = 1.1$ mm) and fast response ($\sim 1\mu$s). In order to prevent a parasitic background coming from the room-temperature environment, low-pass optical filters with a cut-off frequency of 120 cm^{-1} and 55 cm^{-1} are used for magnetically-tuned and standard detectors, respectively. A Winston cone with 15 mm aperture diameter is used to focus the radiation to the active element. A low-noise preamplifier (with a noise parameter 5 nV/Hz$^{1/2}$ above 1 kHz) is used to amplify the absorption signal up to about 1 V. The amplifier is fed with ±20 V. The used cryogenic dewar should be refilled with nitrogen approximately every 24 hours, while the liquid-helium hold time is about two weeks.

As mentioned, for the shorter wavelength range (down to $\sim$200 - 30 μm) a Ge:Ga photoconducting detector (product of „QMC Instrument Ltd") is used. This detector has a larger time constant (of the order of milliseconds), but is suitable for ESR experiments in combination with superconducting and mid- and long-pulse magnets (with a full-pulse duration of several hundreds of milliseconds). For operations in the wavelength range of 4 - 30 μm a liquid-nitrogen cooled HgCdTe (MCT) photovoltaic detector (model J15D26-M204-S01M-60, product of „Teledyne Judson Technologies") with a time constant of 80 ns is used.

2.4. Magnets

Two types of magnets were used in ESR experiments. Fields up to 16 T were produced by a liquid-helium cooled superconducting magnet with a vertical bore (product of „Oxford Instruments Ltd“, UK). This magnet has a high homogeneity [better than 10^{-5} over a 1 cm DSV (diameter spherical volume)]. ESR spectra can be recorded with sweeping the magnetic field with rates up to 0.7 T/min (0 - 7 T), and 0.5 T/min (7 - 16 T). To extend the measurement range to higher magnetic fields one can use pulsed fields, where a short pulse of a high electric current is applied to the coil. In ESR experiments two coils were used. In both cases, the current through the coil was produced by discharging a capacitor bank. The pulse duration is determined by the values of the capacitance and the coil inductance, while the magnetic-field strength depends on the applied energy and the coil design. As the inductance of the pulsed magnet is proportional to the number of wire turns, a higher maximum voltage of the capacitor bank is advantageous to obtain higher currents for higher fields.

HLD is equipped with a 50 MJ/24 kV capacitor bank [30]. The power supply consists of twenty modules: fifteen modules with a maximum electric energy of 2.88 MJ, four 1.44 MJ modules and one 0.9 MJ module. The modules can be operated in a variety of combinations, depending on needs (including feeding of multi-coil magnets).

It is important to mention that pulsed-field magnets are subject to extremely high electrical, thermal, and mechanical stresses. The voltage between adjacent layers of the coil can be as high as several kV, requiring special measures for wire insulation. The coils are cooled by liquid nitrogen. During pulses the magnets undergo a mechanical and thermal shock. Because of the Joule heating, the wire temperature increases from 77 K to above room temperature within fractions of a second. But the most serious problem is the huge mechanical stress, which arises in the coil at peak field due to the Lorentz force. Since pulsed-field magnets are operated close to the destruction limit, the magnet design and choice of materials are of crucial importance.

Determined by various applications, several types of pulsed-field magnets have been designed and fabricated at the HLD [31, 32]. As mentioned, for the ESR experiments, two types of pulsed-field magnets, 8.5 MJ/70 T and 1.4 MJ/60 T, were used. The magnet 8.5 MJ/70 T is used for numerous high-field experiments in fields up to 70 T [31, 33]. The coil has a bore with a diameter of 24 mm. The outer diameter of the coil is 320 mm. A schematic view of the 8.5 MJ/70 T magnet is shown in Fig. 2.19. The coil (1) contains 18 conducting layers, each layer has 36 turns. The calculated field homogenei-

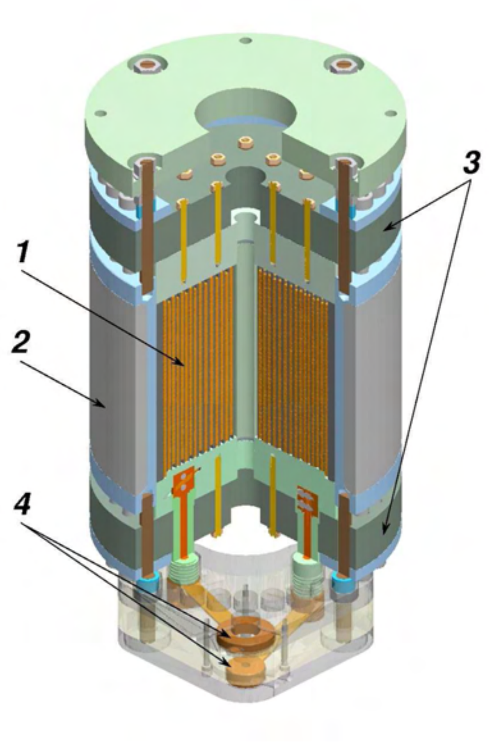

Figure 2.19.: *Schematic view of a 8.5 MJ/70 T pulsed-field magnet. Main parts of the magnet are: coil (1), reinforcement cylinder (2), G-10 end flanges (3), and current leads (4).*

ty in the center of the field is better than 7x10^{-4} over 1 cm DSV (diameter spherical volume). High-copper-content alloy wire, Wieland-K88 [34], with a cross-section of 4x6 mm^2 and Kapton-tape insulation is used. The coil is reinforced by a Zylon-stycast 1266 composite, (Zylon is a trademark name of the high-performance fiber poly-(p-phenylene-2,6-benzobisoxazole) produced by „Toyobo Corporation“, Japan). The insulated wire is additionally covered with a braided S2-glass sleeve. A stainless-steel cylinder (2) with outer diameter of 320 mm is used for external reinforcement of the coil. The G-10 end flanges (3) of the magnet are tightened to the windings with M16 bolts which are screwed into the steel cylinder. A separate assembly provides transitions from copper connectors to the coaxial current leads (4). The coil inductance is about 15 mH. This magnet has a pulse-field rise time of 35 ms, while the full-pulse duration can be changed from approximately 150 to 300 ms by using different crowbar resistors [30] (Fig. 2.20).

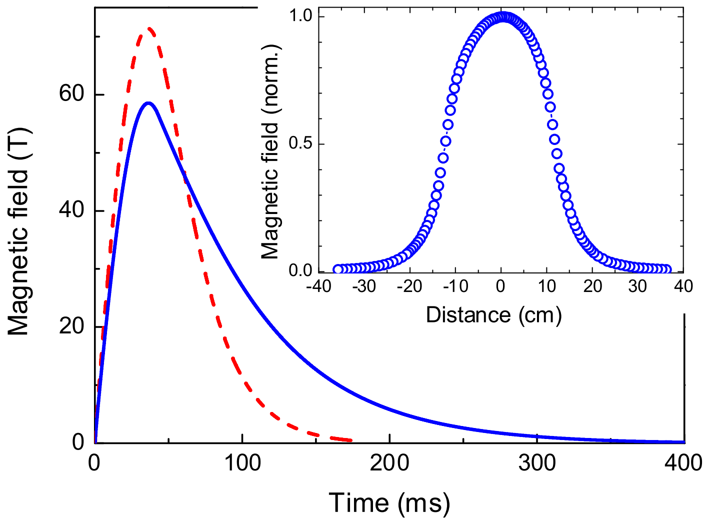

Figure 2.20.: *Magnetic field vs time for a 8.5 MJ/70 T magnet. The solid blue line was obtained with a 0 Ohm crowbar resistor, while the dashed red line corresponds to a 0.33 Ohm crowbar resistor. The inset shows the strength of the magnetic field along its axial direction.*

The maximum peak current is 23.5 kA [31]. As mentioned, during pulses the wire temperature increases from 77 K to above room temperature. The typical waiting time between high-field pulses required for temperature relaxation of this coil is about 3 hours. Alternatively, the ESR experiments can be performed with smaller, 60 T, coils (1.4 MJ/60 T), with the bore diameter of 24 mm and with a typical full-pulse duration of 40 - 50 ms. The advantage of using smaller coils is the shorter temperature-relaxation time (about 1 hour).

2.5. ESR probes

The ESR experiments were performed using resonator-free spectrometers equipped with oversized (9.4 mm inner diameter) wave-guides. Such a construction allows for operation in a very broad frequency range (50 GHz and higher). A schematic view of the 16 T ESR spectrometer is shown in Fig. 2.21. As mentioned, in our experiments BWOs, MVNA, Gunn- and VDI-diodes, and FELs can serve as radiation sources. The radiation propagates through oversized waveguides to the sample, which is located in the center of the magnetic-field coil. The waveguides are made from stainless-steel tubes (10 mm outer diameter). The magnet is equipped with a variable

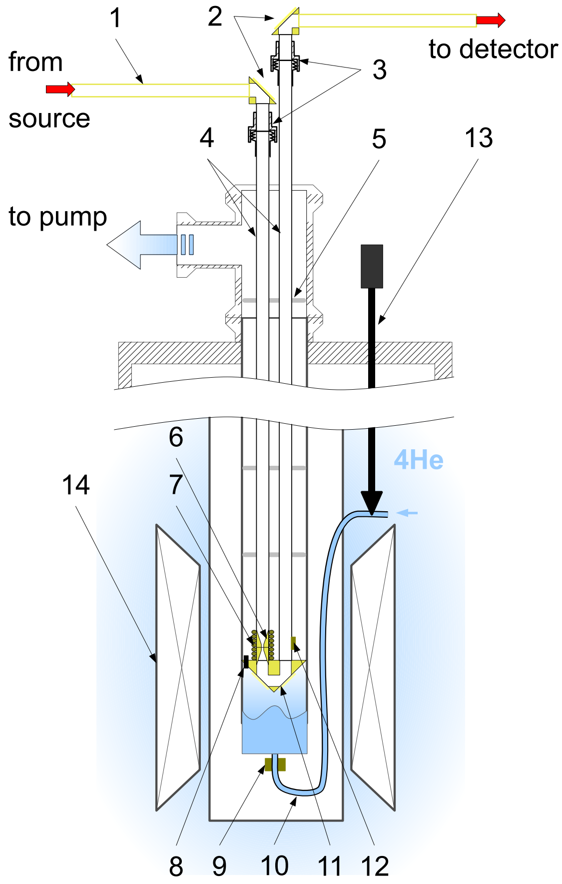

Figure 2.21.: *Schematic drawing of the 16 T ESR spectrometer. 1 - external brass waveguides, 2 - mirrors, 3 - mylar windows, 4 - waveguides, 5 - fins, 6 - focusing horns, 7 - modulation coil, 8 - thermometer, 9 - VTI heater, 10 - capillary, 11 - reflecting joint, 12 - probe heater, 13 - needle valve, 14 - superconducting magnet.*

temperature insert (VTI), allowing for experiments in a temperature range of 1.4 - 300 K. Mylar windows and O-rings are used to seal the VTI inset. The waveguides are coupled by joints to two mirrors which redirect the radiation from the radiation sources to the detector. In case of small samples, the radiation can be focused using two gold-coated brass horns with minimal diameter of 1.5 mm. Silicone grease or GE varnish is used to fix the sample inside the sample-holder. In case of narrow ESR lines (less than 10 mT), a field-modulation technique can be used. For that, a modulation coil (2000 turns over 50 mm) is installed on the waveguide, close to the sample place. The probe is equipped with a heater and thermometer (Cernox, CX-1050-SD, product of „Lake Shore Cryotronics, Inc.“, USA) located close to the sample. Using lock-in technique the spectrometer can work in two modes: either the radiation is modulated optically (using a mechanical chopper) or by employing a field-modulation technique. The later produces the derivative of the transmission signal, and, as mentioned, is preferable when the ESR line is relatively narrow. The modulation frequencies can be varied in the range between 1 and 500 Hz (optical modulation) and 3 Hz and 10 kHz (field modulation).

A second ESR probe has been built for use in pulsed magnetic fields. It has a very similar design, with a few variations. That probe is made using two stainless-steel waveguides with 5.6 mm inner diameter to fit the available sample space with a diameter of 14 mm. A cryostat („KONTI-IT-Cryostat", product of „CryoVac mbH & Co KG") equipped with VTI allows for ESR experiments in a temperature range between 1.4 and 300 K. A cryogenic temperature controller (model 340, product of „Lake Shore Cryotronics, Inc.", USA) in combination with standard Cernox^{TM} temperature sensors are used to monitor the temperature. A digital oscilloscope (model DL750, product of „Yokogawa Electric Corporation", Japan) is used to register the ESR signal and the signal from the pick-up coil. DPPH (2,2-diphenyl-1-picrylhydrazyl) is used to calibrate the magnetic field that is monitored using the integrated signal from pick-up coil. A calibration accuracy better than 0.2% can be achieved.

The pulsed-field probe can be used in combination with two free-electron lasers available at the FZD. These lasers produce a monochromatic radiation in the wavelength range between 4 and 250 μm, allowing ESR experiments with a spectral resolution of 0.5% [35]. To demonstrate the high spectral resolution, DPPH was chosen for our experiments. Due to the narrow line and the temperature-independent g-factor (2.0037) known with high accuracy DPPH is widely used as ESR standard. A powder sample with a mass of 9 mg was used in the experiment. The ESR spectrum of DPPH was obtained at a wavelength of 190.6 μm at a temperature of 7 K [35] (Fig. 2.22). Two very sharp peaks were resolved in the ESR spectrum at 56.1 T during the up and down field sweeps. The inset shows the ESR absorption in DPPH as function of magnetic field. The solid line represents a Gaussian fit. Our analysis reveals a resonance width at half maximum of $\Delta B = 0.3$ T in this measurement, which corresponds to a spectral resolution of about 0.5% determined by the spectral distribution of the FEL radiation power due to its bandwidth-limited pulsed nature.

A further example of an ESR spectrum obtained by use of the FEL beam is shown in Fig. 2.23. The hexagonal YMnO$_3$ is ferroelectric and antiferromagnetically ordered at temperatures below $T_N \sim 70$ K, exhibiting an antiferromagnetic gap of $\sim$ 1.3 THz in the magnetic excitation spectrum.

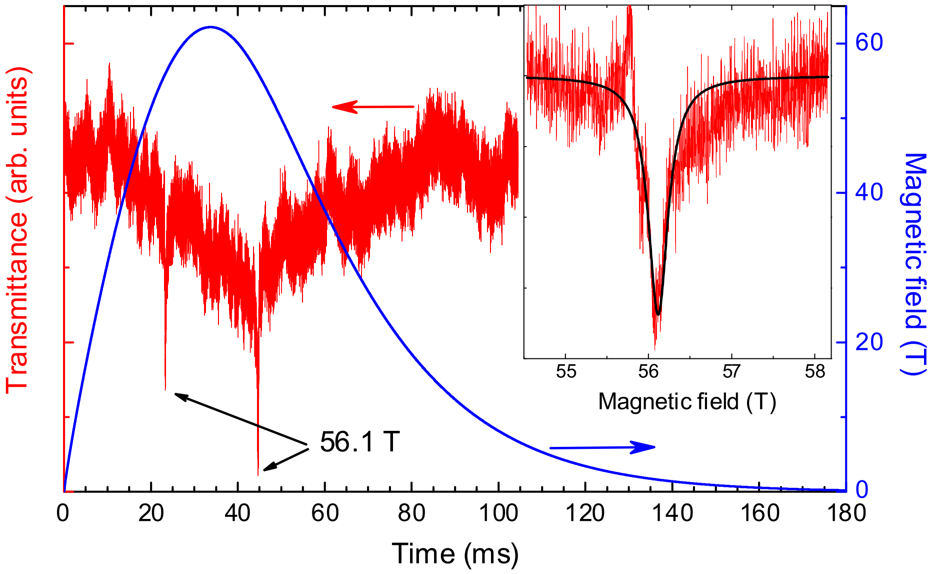

Figure 2.22.: *Time dependences of the magnetic field (blue line) and of the transmittance of FEL radiation through DPPH (red) obtained at a wavelength of 190.6 μm and a temperature of 7 K. The maximum of the field is 62 T. The inset shows the ESR absorption in DPPH vs magnetic field. The black line represents a Gaussian fit with* $\Delta B/B \approx 0.5\%$*. The 8.5 MJ/70 T magnet was used.*

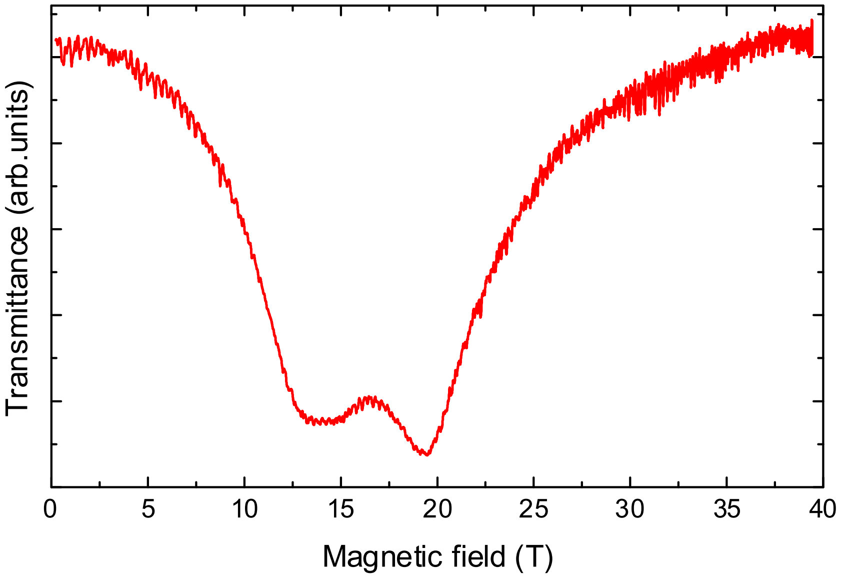

Figure 2.23.: *An example of the ESR spectrum in* $YMnO_3$ *obtained at a wavelength of 199.8 μm at a temperature of 2 K.*

In our experiments, single-crystalline samples of $YMnO_3$ with mass of 75 mg and an approximate size of 3x3x1 mm^3 were used. The sample was grown by the traveling-solvent floating-zone technique. Fig. 2.23 shows an example of an ESR spectrum obtained for $YMnO_3$ at a wavelength of 199.8 μm in fields up to 40 T and at a temperature of 2 K. A well-pronounced absorption corresponding to an antiferromagnetic resonance was observed for a magnetic field oriented along the *b* axis. The double-peak structure of the absorption (which can be an indication of a finite interaction between the triangular Mn sublattices from adjacent layers [36]) is nicely seen in the ESR spectrum.

In addition to the described ESR spectrometers, an X-band ($\approx$ 9.4 GHz, 1.8 T) ELEXSYS E500 spectrometer (product of „Bruker Corporation“) was used as well.

2.6. Summary

In conclusion, the ESR spectrometers (and their main components, including radiation sources, detectors, and probes) used in this thesis are described. The spectrometers allow to perform ESR experiments in a very broad frequency-field range (50 GHz - 1.4 THz using a 16 T superconducting magnet, and 100 GHz - 75 THz employing 70 T pulsed-field magnets). This equipment is of particular importance for studying magnetic excitation spectra in spin systems with large zero-field splitting (for instance single-molecular magnets, magnetically ordered materials, and gaped quantum-disordered antiferromagnets) and magnetic materials exhibiting field-induced phenomena (such as spin-reorientation transitions, quantum critical behavior, etc.).

3. (6MAP)CuCl$_3$: a spin-$\frac{1}{2}$ chain system with NNN interaction

3.1. Spin-$\frac{1}{2}$ chain systems: a brief description of the model

The isotropic $S = \frac{1}{2}$ Heisenberg chain with uniform nearest-neighbor exchange coupling represents one of the most fundamental models of quantum magnetism. The system can be described using the effective spin-Hamiltonian

$$H = J \sum \vec{S}_i \cdot \vec{S}_{i+1}, \tag{3.1}$$

where J is the nearest-neighbor interaction and $\vec{S}_i$ is the quantum spin operator. Noticeably, this model is one of the few quantum many-body problems which can be solved exactly. The theory [37] predicts that the ground state of the $S = \frac{1}{2}$ Heisenberg antiferromagnetic (HAF) chain ($J > 0$) is a spin singlet ($S_{tot} = 0$) with the spin-correlation function decaying algebraically. Interestingly, such a systems is not long-range ordered even at $T = 0$.

The fundamental carriers of energy in an $S = \frac{1}{2}$ HAF chain are quantum excitations known as spinons (Fig. 3.1). Spinons are fractional quasi-particles that possess spin values of $S = \frac{1}{2}$ and, generally, can be only created in pairs. As total spin in the isolated chain is conserved, only simultaneous flips of two opposite spins are permitted. The spinons can be regarded as mobile domain walls between two antiferromagnetic states.

Fractionalization of spin excitations into multi-spinon states is a fingerprint of the $S = \frac{1}{2}$ HAF chain. Through the magnetic interaction with a probing photon (ESR) or neutron (neutron scattering), a single spin in the middle of a chain can be flipped. This excitation carries $S = 1$ and separates into two spinon pairs, subsequently moving apart by consecutive two-spin-flips processes (Fig. 3.1c and d). Spinon pairs dominate the low-energy excited states of an $S = \frac{1}{2}$ HAF chain, forming a continuum band of allowed energies

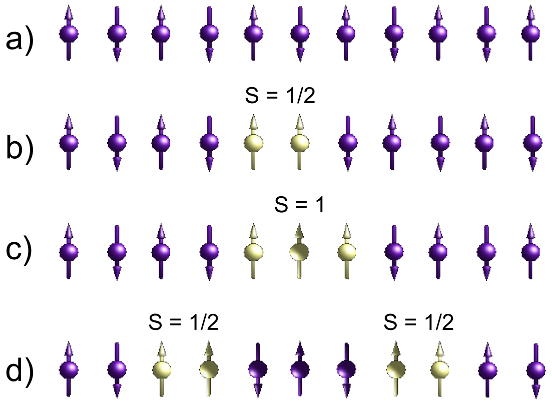

Figure 3.1.: *Lowest-lying eigenstates of a Heisenberg antiferromagnetic $S = \frac{1}{2}$ chain. a) Possible ground state $S = 0$. A second possible state is found by flipping all the spins b) The fundamental excitation is a mobile domain wall that consists of two parallel spins - collectively known as a spinon (shown in yellow) - separating the two possible ground states. c) Flipping a spin in the center of the chain produces an excited state with a total spin of 1. d) Further flipping of two spins on each side of the central spin produces a state with the same energy, so the spinons can propagate independently within the chain.*

whose upper and lower boundaries are determined by the spinon-dispersion law [38]. The continuum of excited states is a consequence of the fact that spinons with different momenta propagate independently from each other. The excitation spectrum is represented by a dynamical spin-correlation function, which can be probed by neutron scattering (over the whole Brillouin-zone as shown in Fig. 3.2 [39]) and by ESR (at zero momentum). It is noteworthy, that the excitation spectrum in such a system is gapless in zero magnetic field and at $B < B_{sat}$, where B_{sat} is the saturation field. A uniform external magnetic field causes a substantial rearrangement of the excitation spectrum, making the soft modes incommensurate [38, 39], although the spinon continuum remains gapless. In a sufficiently strong magnetic field, $B > B_{sat}$, the system is in a fully spin-polarized phase and the excitation spectrum is gaped and dominated by ordinary spin waves (magnons).

The gapless behavior is special for half-integer Heisenberg spin chains, while for integer ones, Haldane conjectured [40] that there exists a finite energy gap between the singlet ground state and the first excited triplet states, without any magnetic order at low temperatures. Experimental, numerical, and theoretical studies have confirmed this conjecture for $S = 1$ and some

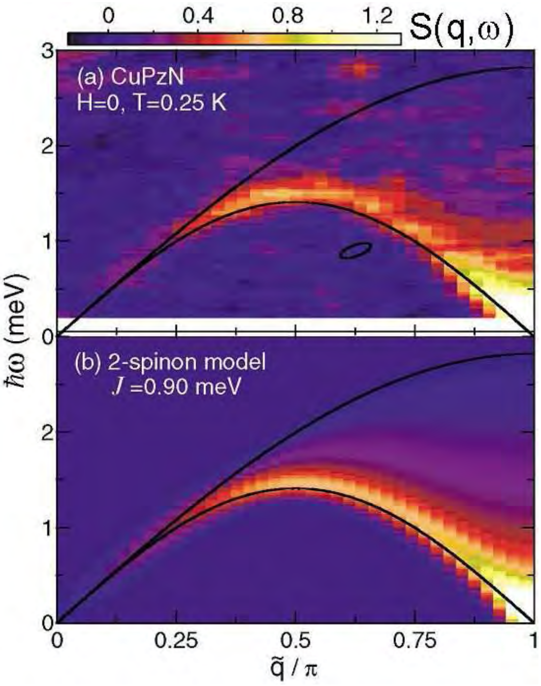

Figure 3.2.: *Magnetic inelastic neutron-scattering intensity for the* $S = \frac{1}{2}$ *HAF chain material CuPzN at* $T = 0.25$ *K in zero magnetic field [39]. (b) Calculated two-spinon contribution to* $S(q,\omega)$*. Solid lines are predicted lower and upper bounds of the two-particle spinon continuum [38]. After Ref. [39].*

other higher spin values. On the other hand, half-integer spin chains can be driven to a gaped phase by anisotropy or bond alternation.

The dynamical spin-correlation function and its evolution with temperature and magnetic field was successfully studied theoretically as well as experimentally [38–42]. Various experimental results are systematically and quantitatively understood within the isotropic one-dimensional Heisenberg AF chain model with nearest-neighbor (NN) exchange interactions. Further generalization of this is the inclusion of bond alternation and next-nearest-neighbor (NNN) interactions:

$$H = \sum J_1 \left(\vec{S}_{2i-1} \cdot \vec{S}_{2i}\right) + J_2 \left(\vec{S}_{2i} \cdot \vec{S}_{2i+1}\right) + J_{NNN} \left(\vec{S}_i \cdot \vec{S}_{i+2}\right), \qquad (3.2)$$

where J_1 and J_2 are NN and J_{NNN} is NNN exchange interactions. Such a system can also be considered as a zigzag spin ladder (Fig. 3.3) characterized by dimensionless parameters controlling the coupling strength: $\alpha = J_N/J_1$ corresponds to the next-nearest-neighbor exchange and $\beta = J_2/J_1$ to the bond alternation.

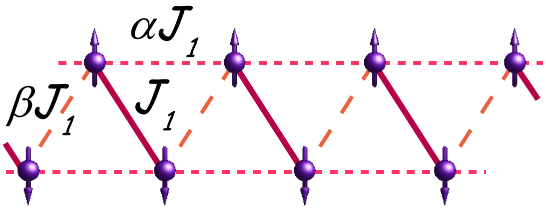

Figure 3.3.: *Bond connections in Hamiltonian (3.2). Here, J_1 is designated as the largest interaction, J and $\alpha = J_N/J_1$, $\beta = J_2/J_1$ are dimensionless parameters.*

Quantum effects and geometrical frustrations in such systems yield a rich phase diagram of non-magnetic ground states at zero magnetic field [43] (Fig. 3.4). When $J_N > 0$, frustrations are important, irrespective of the sign of J_1. When $\alpha = 0$ and $\beta = 1$, the system is equivalent to the Heisenberg chain exhibiting gapless excitations. The increase of the parameter α induces an infinite-order phase transition from a gapless state to a gaped dimerized state. The critical value for α is numerically estimated to be $\alpha_c = 0.241$. Then next remarkable peculiarity is the so-called Majumdar-Ghosh (MG) point at $\alpha = 0.5$, where the ground state has a twofold degeneracy and is composed by products of singlet pairs formed by nearest-neighbor spins. The MG point separates the commensurate dimer-gaped phase ($\alpha_c < \alpha < 0.5$) from incommensurate states ($\alpha > 0.5$). The latter phase, characterized by spi-

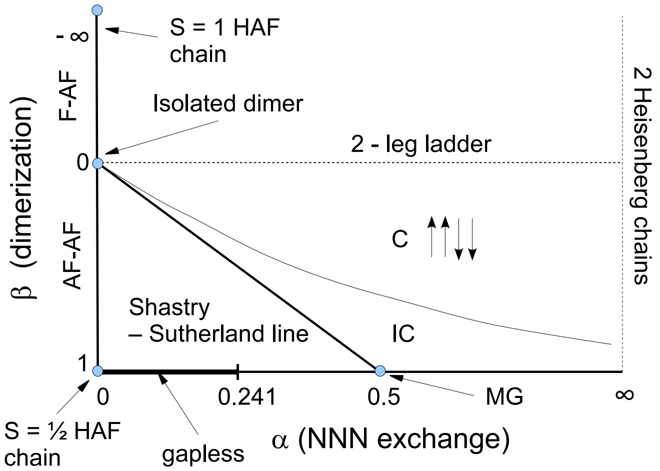

Figure 3.4.: *Schematic phase diagram of the parameter space for the Hamiltonian (3.2), spanned by the two dimensionless parameters α and β. Phases C and IC correspond to commensurate and incommensurate states, respectively. After Ref [43].*

ral spin correlations [44], is expected to extend up to the limit $\alpha \to \infty$, which corresponds to two decoupled Heisenberg chains for which the gap value decays exponentially, $\Delta \propto \exp(-const \cdot \alpha^{-1})$.

On the β axis ($\alpha = 0$) the Hamiltonian (3.2) represents AF-ferromagnetic bond-alternating chains for $\beta < 0$. In the limit of $\beta \to -\infty$, the Hamiltonian is reduced exactly to the $S = 1$ Heisenberg AF model, described by Haldane [40]. Spin-gap properties continue into the AF-AF alternating region ($\beta > 0$). In the gaped regime the spin-correlation function decays exponentially, however, in the vicinity of the α axes ($\beta \approx 1$) short-range correlations are described by a semi-algebraic decay. The particular case $\beta = 0$ corresponds to the two-leg ladder which turns into a number of isolated dimers at $\alpha = 0$. Shastry and Sutherland showed that a simple decoupled-dimer wave function is an exact eigenstate of Hamiltonian (3.2) and that it is the ground state over a restricted parameter regime $\alpha = 2\beta$ [45]. Above the Shastry-Sutherland line the IC region is situated (where the spin-correlation function decays with a quasi-periodic oscillation) with a neighboring commensurate region characterized by AF correlation, when alternating two spins point up and two spins point down ($\uparrow\uparrow\downarrow\downarrow$). As soon as $\beta = 1$ the spin polarization is delocalized to the whole system (corresponding to spinons) irrespective of the value of α and the free-spinon picture appears to be applicable for the low-lying excitations. When dimerization is introduced, two spinons create a bound state and an isolated magnon branch (and even multimagnon branches) appear below the spinon continuum becoming evident when $\beta < 0.98$.

Aside from the general aspect of theoretical interest, especially for understanding the role played by frustration and incommensurability in quantum spin systems, an additional motivation to study zigzag spin ladders is the fact that a large class of copper oxides can essentially be described by this model. The distinct magnetic behavior of zigzag ladders for different ratios of J_2/J_1 and J_N/J_1 is an important problem from both the theoretical and experimental sides.

As mentioned, the most important feature of the uniform $S = \frac{1}{2}$ Heisenberg-chain model is its integrability by means of the famous Bethe ansatz [37]. However, as revealed theoretically and experimentally, the uniform spin chains are unstable with respect to any perturbation, breaking the chain uniformity. Such instability gives rise to a rich variety of strongly correlated spin states and quantum phase transitions, making these objects an attractive ground for testing various theoretical concepts experimentally. A competition between NN and NNN interactions, as well as the presence of magnetic anisotropy can fundamentally modify the ground-state properties of quantum spin chains resulting in a large diversity of complex magnetic structures [46–53].

The experimental determination of these exchange interactions often is a challenging task. For that, magnetic and thermodynamic measurements (magnetization, magnetic susceptibility, and specific heat) are very helpful but do not give a detailed picture of the magnetic interactions. Inelastic neutron scattering is a more suitable tool, but it has certain serious limitations (including, for instance, requirements on the sample size and chemical composition of the material). That is why the search for new approaches (both theoretical and experimental) that are helpful in clarifying the microscopic structure of magnetic interactions appears to be of particular importance.

Electron spin resonance is traditionally recognized as one of the most sensitive techniques for probing magnetic excitations with high resolution in spin systems with collective ground states (see for instance [2, 54–56]). Recently, the dynamical mean-field-like theory for the ESR in $S = \frac{1}{2}$ chains with NN and NNN interactions has been developed [57]. It was shown that in the case of an alternation of NN interactions, two ESR modes at the frequencies $h\nu_{1,2} = |g\mu_B B + \Delta_{1,2}|$, where $\Delta_{1,2}$ are energy gaps, should emerge. According to Ref. [57] for a two-center $S = \frac{1}{2}$ Heisenberg AF chain with alternating NN interactions ($J_{1,2}$ denote the values of the isotropic antiferromagnetic couplings in the two-center model, and $A_{1,2}$ describe the magnetic anisotropy for those couplings), the absorbed power of the *ac* magnetic field with magnitude h_0 can be written as

$$Q = \frac{(g\mu_B h_0)2\nu h\gamma}{4}\left[\frac{I_1}{(g\mu_B B - \Delta_1 - h\nu)2 + (h\gamma)2} + \right.$$
$$\left. + \frac{I_2}{(g\mu_B B - \Delta_2 - h\nu)2 + (h\gamma)2}\right], \tag{3.3}$$

where

$$2\Delta_{1,2} = (J_1 + J_2 + A_1 + A_2)R_+ \pm \left[(J_1 + J_2 - 2A_N)^2 R_+^2 + \right.$$
$$\left. + (A_1 + A_2 - 2A_N)(2J_1 + 2J_2 + A_1 + A_2 - 2A_N)R_-^2\right]^{1/2}. \tag{3.4}$$

Here, γ is the relaxation rate, A_N is the magnetic anisotropy of the NNN interaction between spins in the chain, $R_\pm = \langle S_{0,1}^z \rangle \pm \langle S_{0,2}^z \rangle$ are the sum and the difference of the average values of the z-projections of the total spin, belonging to the first and second magnetic center (i.e., the doubled homogeneous and staggered magnetizations of the chain along the direction of the applied

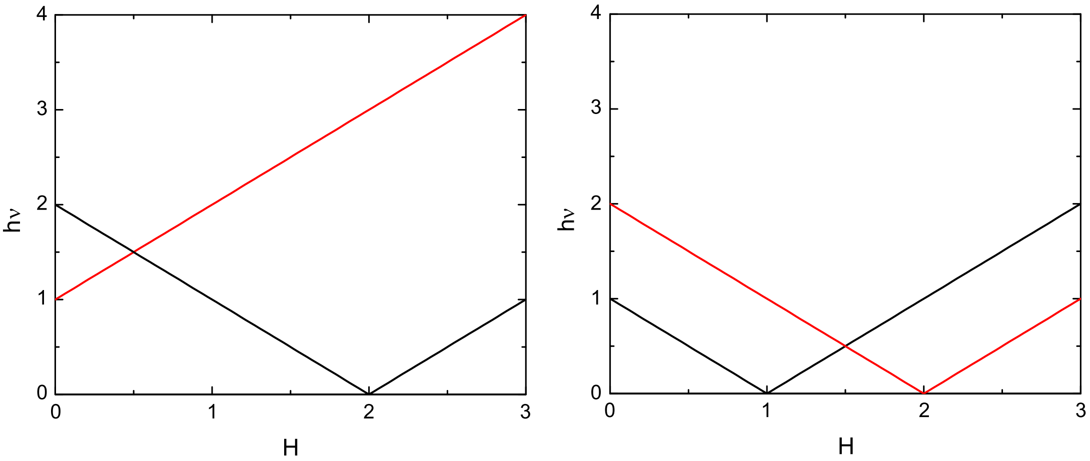

Figure 3.5.: *Magnetic-field dependence of the ESR resonance frequencies for an alternating antiferromagnetic spin-$\frac{1}{2}$ chain with strong (left) and small (right) NNN interactions. After Ref. [57].*

dc magnetic field). According to Eq. (3.3) the absorption has to show two maxima as function of the applied *dc* magnetic field B for the two-center model, whereas in the absence of magnetic anisotropy $A_{1,2,N} \to 0$, the absorption reveals only one maximum at $h\nu = g\mu_B B$. This results nicely agrees with those reported in Refs. [58–60]. The shifts of the resonance positions are determined by $\Delta_{1,2}$. In order to observe two different shifts $\Delta_1 < \Delta_2$ the NNN magnetic anisotropy has to satisfy the following inequality

$$A_N[\langle S^z_{0,1}\rangle 2 + \langle S^z_{0,2}\rangle 2] > (A_1 + A_2)\langle S^z_{0,1}\rangle\langle S^z_{0,2}\rangle.$$

Such an asymmetric shift of the resonance positions can be regarded as a robust signature of the presence of NN and NNN interactions.

Importantly, depending on the sign and strength of the NN and NNN interactions, the theory predicts different frequency-field diagrams of ESR magnetic excitations (Fig. 3.5). ESR experiments on the frustrated $S = \frac{1}{2}$ quasi-one-dimensional systems In_2VO_5 [61], Li_2ZrCuO_4 [62], and on the asymmetric spin-ladder compound IPA-$CuCl_3$ [63] revealed qualitative agreement with the theoretical predictions.

In what follows, the present work studies the magnetic properties and ESR in the low-dimensional compound $(C_6H_9N_2)CuCl_3$. This material had been expected to be an $S = \frac{1}{2}$ Heisenberg chain from the crystallographic structure, however, possesses properties that can be explained in frame of the spin-$\frac{1}{2}$ alternating Heisenberg chain with NNN interactions.

3.2. (6MAP)CuCl$_3$: crystal structure, magnetic and thermodynamic properties

The spin-chain complex $(C_6H_9N_2)CuCl_3$ [hereafter called (6MAP)CuCl$_3$] has an orthorhombic crystal structure belonging to the space group *Pnma*, with lattice constants $a = 11.4$ Å, $b = 6.6$ Å, and $c = 12.8$ Å (measured at room temperature [64]). $Z = 4$ is the number of formula units per unit cell [65]. The compound is built up from well-isolated, doubly-bridged linear chains of Cu^{2+} ions (Fig. 3.6). There are two types of crystallographically similar chains running along the b axis. Each copper ion has a square-pyramidal coordination geometry, with the axial bond substantially longer than the basal ones, and with the direction of the axial bond alternating along the chain axis b. The Cu-Cl-Cu bridging angle is well above 90 deg, which defines the AF nature of the next-neighbor exchange interactions, $J/k_B \approx 107$ K [64,65]. The individual chains are effectively isolated in the a and c directions by the 6-methyl-2-aminopyridinium $(C_6H_9N_2)^+$cations. A hydrogen-position disorder in the amino groups, which link the Cu chains, has been identified in earlier work [65]. Using the formula for the Néel temperature T_N from Ref. [66] and assuming $T_N < 100$ mK (as evident from muon-spin-relaxation experiments [67]), the interchain interaction J'/k_B is estimated to be less than 40 mK, suggesting $J'/J < 4 \times 10^{-4}$ and indicating an almost perfect one-dimensional nature of the magnetic correlations in (6MAP)CuCl$_3$.

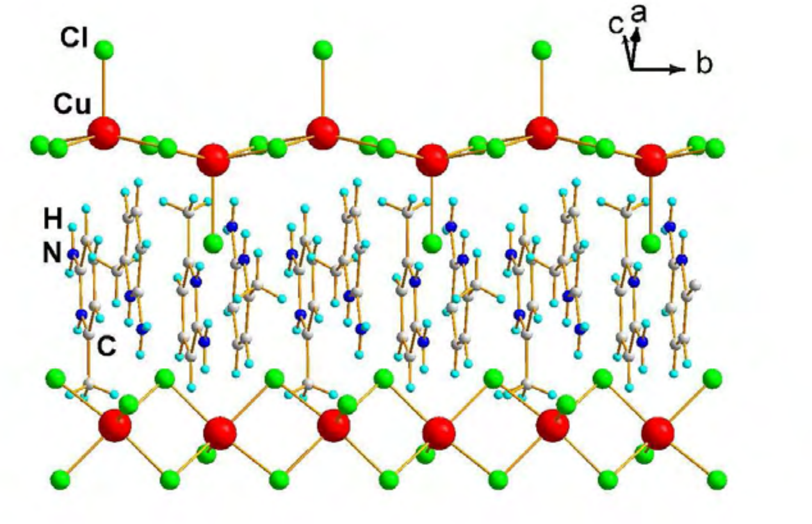

Figure 3.6.: *Crystal structure of (6MAP)CuCl$_3$.*

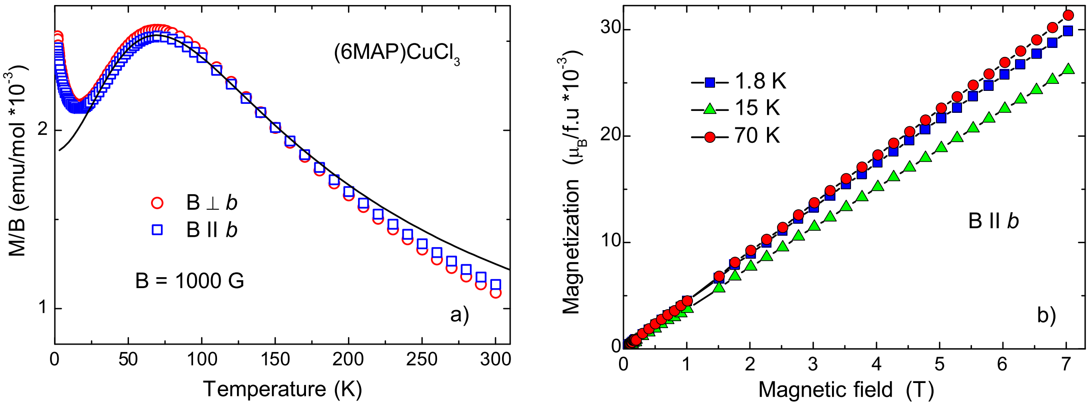

Figure 3.7.: *a) Temperature dependence of the magnetic susceptibility (M/B) in (6MAP)CuCl$_3$ at $B||b$ (circles) and $B \perp b$ (squares). The solid line represent $\chi(T)$ for the uniform $S = \frac{1}{2}$ Heisenberg AF chain [68] with $J/k_B = 107$ K. b) Magnetization data vs magnetic field applied at $B||b$ for different temperatures.*

Magnetization measurements of single-crystalline (6MAP)CuCl$_3$ samples were performed using a Quantum Design SQUID magnetometer in the temperature range between 1.8 and 300 K. High-quality single-crystalline (6MAP)CuCl$_3$ samples with sizes of approximately 1.5×1.5×3 mm^3 were used for magnetization as well as for specific-heat and ESR measurements. The magnetization measured as a function of temperature in a magnetic field of 0.1 T parallel and perpendicular to the b axis is shown in Fig. 3.7a. For both crystal orientations, χ exhibits a broad maximum at $\sim$ 70 K (which is a signature of the low-dimensional character of the magnetic interactions) and a Curie-like upturn is observed below $\sim$ 15 K. Overall, the data are similar to those measured by Liu *et al.* [64] in a field of 5 T. The results of magnetization measurements vs magnetic field at temperatures of 1.8, 15, and 70 K are shown in Fig. 3.7b. The magnetization exhibits a linear field dependence measured in fields up to 7 T. No saturation of the magnetization was observed up to 60 T in pulsed-field measurements at a temperature of 1.5 K. Whereas above $\sim$20 K, the susceptibility of (6MAP)CuCl$_3$ exhibits a behavior typical for an $S = \frac{1}{2}$ one-dimensional AF Heisenberg chain system [64], below $\sim$20 K a deviation from the expected behavior is observed [64, 65, 69], i.e., the low-temperature magnetic susceptibility shows a pronounced low-temperature upturn proportional to $1/T$. Very often, in spin-chain compounds such a low-temperature tail in the magnetic susceptibility originates from broken-chain effects and/or defects, overshadowing the intrinsic low-temperature suscep-

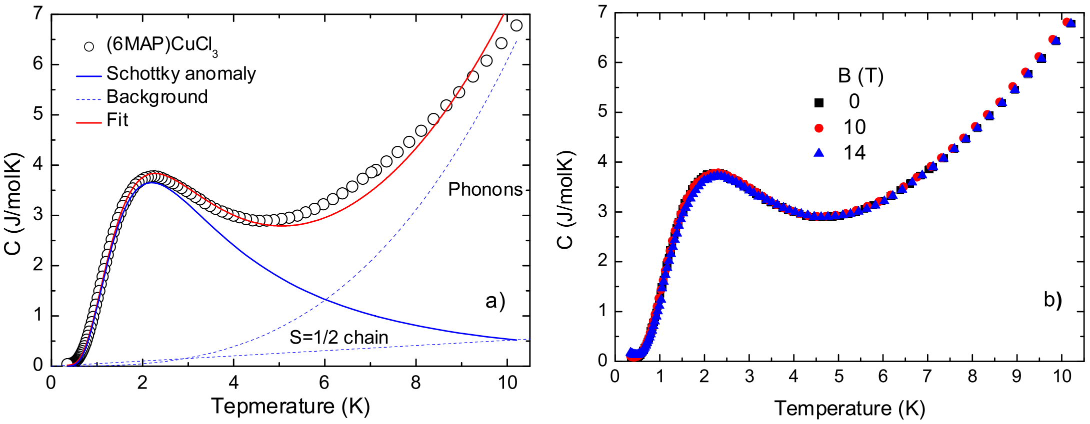

Figure 3.8.: *Temperature dependence of the specific heat of single crystalline (6MAP)$CuCl_3$ a) at zero magnetic field and b) at different magnetic fields of 0, 10 and 14 T. The magnetic field is applied along the b axis. The blue solid line in a) shows the specific heat for a two-level Schottky anomaly with energy gap of 5.3 K.*

tibility (which is of particular importance when describing the ground state of spin-chain materials).

The specific heat of a (6MAP)$CuCl_3$ was measured in the temperature range from 0.35 to 100 K by use of a thermal-relaxation method in a Quantum Design PPMS system. A relatively broad anomaly was observed at $T \approx 2.2$ K (Fig. 3.8a) [69]. The entropy under the anomaly, $\Delta S = 4$ J/molK, was calculated after subtraction of the lattice contribution and of the low-temperature part of the magnetic specific heat of an $S = \frac{1}{2}$ HAF chain. The shape of this anomaly appears to be reminiscent of a two-level Schottky-type specific heat. The low-temperature part of the specific heat for (6MAP)$CuCl_3$ was fitted by the following equation:

$$C = a \cdot T + bT^3 + R\left(\frac{E}{k_B T}\right)^2 \frac{g_1}{g_2} \frac{\exp\left(\frac{E}{k_B T}\right)}{\left[1 + \frac{g_1}{g_2}\exp\left(\frac{E}{k_B T}\right)\right]^2}, \tag{3.5}$$

where $R = 8.31$ J/molK is the universal gas constant, b and E are fitting parameters. In Eq. (3.5), the first term with $a = 0.0515$ J/molK^2 represents a contribution from the $S = \frac{1}{2}$ HAF chain with $J/k_B = 107$ K and the second term corresponds to the lattice contribution. The last term is a two-level Schottky specific heat [70] with a degeneracy ratio $g_1/g_2 = 1$. This fit allows to estimate the energy gap, $E/k_B \approx 5.3$ K.

In the case of a magnetically induced gap (occurring for instance in $[PM{\cdot}Cu(NO_3)_2(H_2O)_2]_n$ [71]), a significant shift of the anomaly with increasing magnetic field would be expected. Such behavior would correspond to the creation of a breather mode as shown in Ref. [56]. The specific heat of (6MAP)$CuCl_3$ was measured in magnetic fields up to 14 T. However, no changes in the anomaly position as well as in the overall specific heat were observed (Fig. 3.8b). This shows that the observed anomaly is not of magnetic origin. The magnetic-field independence suggests that the pronounced maximum at $T \approx 2.2$ K is caused by structural effects. Particularly, it can be regarded as a low-temperature signature of hydrogen-position disorder in the amino groups linking the Cu chains [65]. In order to better understand the magnetic properties we investigated the low-temperature excitation spectrum in (6MAP)$CuCl_3$ by means of ESR [72].

3.3. ESR studies of (6MAP)CuCl$_3$

Low-frequency ESR experiments were performed using the X-band Bruker E500 spectrometer operating at a frequency of 9.4 GHz. The ESR spectra appear as a single resonance line with a shape close to Lorentzian. Temperature dependences of the ESR linewidth and resonance field in (6MAP)$CuCl_3$ measured for $B \parallel b$ down to 7 K are shown in Fig. 3.9. With decreasing temperature, the ESR line becomes broader, accompanied by a pronounced shift of the resonance field.

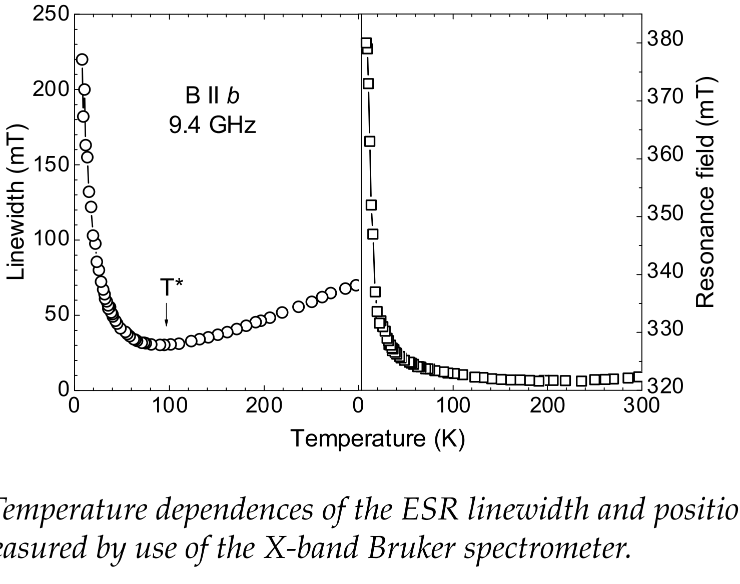

Figure 3.9.: *Temperature dependences of the ESR linewidth and position of the resonance field measured by use of the X-band Bruker spectrometer.*

Two temperature regions (below and above $T^* \approx J/k_B$) can be clearly distinguished. The observed behavior unambiguously confirms the incompatibility with the response from a simple uniform $S = \frac{1}{2}$ Heisenberg chain model. The low-temperature upturn ($T < T^*$) of the linewidth and of the position of the resonance field (Fig. 3.9) can only be explained by the presence of additional interactions (which are relevant perturbations for the critical Heisenberg chain from the viewpoint of renormalization group). They may originate from different factors, such as symmetric (exchange) or asymmetric (Dzyaloshinskii-Moriya) spin-spin interactions, or the g-tensor alternation, which would cause a multiplication of the unit cell [58–60]. Besides, in accordance with this theory [58–60], the linear increase of the linewidth above T^* can be explained by exchange anisotropy.

To study the frequency-field dependence of the magnetic excitations in (6MAP)CuCl$_3$, further experiments were made using the high-field tunable-frequency ESR spectrometer. The ESR measurements were performed in the frequency range between 100 and 400 GHz in magnetic fields up to 16 T. The magnetic field was applied along the b axis. A single ESR line (with $g = 2.06$ at 20 K) was observed at temperatures above 5 K. Below $\sim$ 5 K a second resonance mode appears (the mode B in Fig. 3.10).

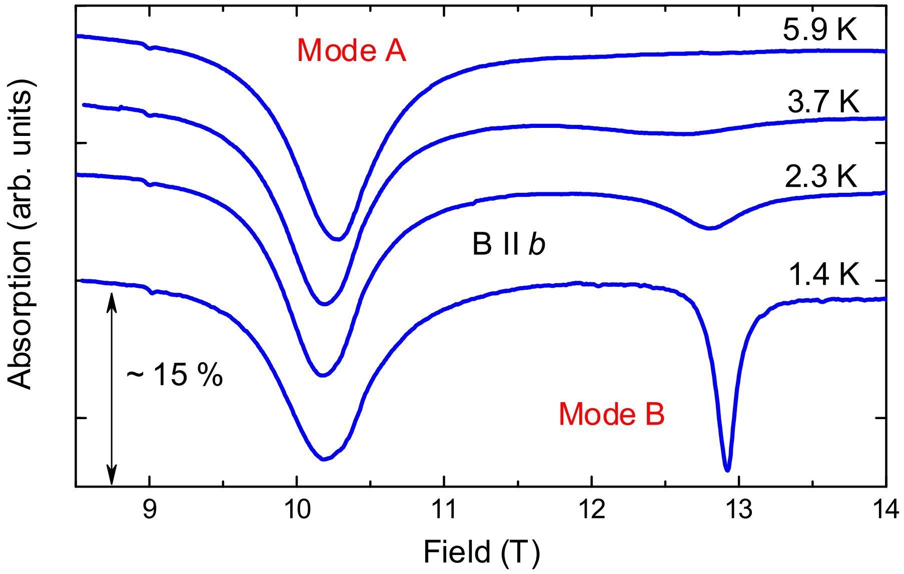

Figure 3.10.: *ESR spectra of (6MAP)CuCl$_3$ obtained at a frequency of 300 GHz for different temperatures.*

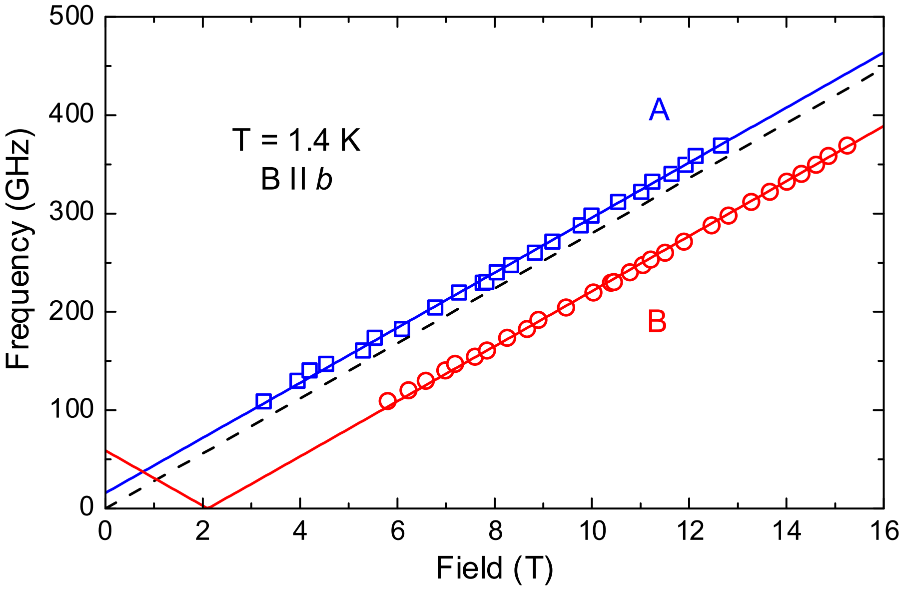

Figure 3.11.: *Field dependence of the magnetic-excitation frequencies in (6MAP)CuCl$_3$ at $T = 1.4$ K. Symbols denote experimental data, while solid lines correspond to theoretical results (see text for details). The dashed line denotes $h\nu = g\mu_B B$ for $g = 2$.*

The frequency-field diagram of the magnetic excitations in (6MAP)CuCl$_3$ obtained at 1.4 K is shown in Fig. 3.11. The resonance absorptions in the studied frequency-field range have a linear field dependence with $g \approx 2$. Linear extrapolations of the frequency-field dependences of the ESR modes A and B to zero field yield the resonance-field shifts $\Delta_A = 15.9$ GHz (0.76 K) and $\Delta_B = -59$ GHz (-2.83 K), respectively. No signatures of these low-energy gaps were observed in magnetization measurements (Fig. 3.7), since the lowest temperatures used in magnetizations experiments are comparable with the gap values.

It was shown theoretically [58–60], that the ESR response of an ideal uniform $S = \frac{1}{2}$ Heisenberg AF spin chain with magnetically isotropic interactions should reveal a single peak in the ESR absorption with zero linewidth (in the absence of spin-lattice and electron-nuclear couplings) and with the position of the resonance proportional to the applied magnetic field. The observation of two gaped modes clearly indicates the incompatibility with this simple model, suggesting the presence of additional interactions in this compound.

The ESR spectra in (6MAP)CuCl$_3$ can be consistently described by the theory presented in Ref. [57], assuming that the intrachain interaction is of

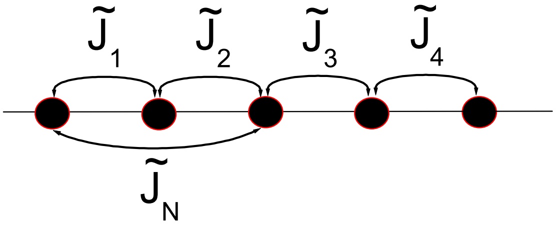

Figure 3.12.: *A schematic view of a spin-chain structure with four nearest-neighbor ($\tilde{J}_{1,2,3,4}$) and one next-nearest-neighbor ($\tilde{J}_N$) interactions proposed for (6MAP)CuCl$_3$ (see text for details).*

the order of the observed gaps. The combined effect of alternation and magnetic anisotropy is predicted to manifest itself in the opening of a gap in the ESR spectrum. Most importantly, the presence of the AF NN and of a large-enough NNN interaction (see Eq. 3.1) should result in asymmetric (with respect to $h\nu = g\mu_B B$) frequency-field dependences of the ESR peaks (Fig. 3.5a). This proposed frequency-field dependence nicely agrees with our observations in (6MAP)CuCl$_3$, strongly suggesting the presence of NNN interaction and alternation in this compound. On the other hand, the observation of a broad maximum in the susceptibility of (6MAP)CuCl$_3$ at $T \sim 70$ K implies the presence of short-range-order spin correlations at this energy scale, which is much larger than the observed gaps.

To describe both the magnetic susceptibility and the ESR data a more complex scenario has to be considered. The inclusion of additional magnetic interactions for a minimal model results in an effective tetramerization of the spin-spin couplings. Different values of exchange couplings (defined as $\tilde{J}_{1,2,3,4}$ in Fig. 3.12) between neighboring sites along the chain would yield the multiplication of the magnetic unit cell and, as a consequence, four ESR modes in the excitation spectrum.

Since no integrable model for (6MAP)CuCl$_3$ is available, the simplified four-center XY model [73] is applied to illustrate the effect of NNN interactions. Although no physical realization of the XY model (with $J = A$, where J and A are the exchange coupling and anisotropy parameters, respectively) is known, the exceptional usefulness of this model is determined by its exact solvability. The dispersion laws of the four excitation branches, A, B, C, and D, are shown in Fig. 3.13. In ESR experiments transitions between spin eigenstates with $\Delta S^z = 1$ should be observable, i.e., all four branches at $k = 0$ should be excitable in ESR measurements. In the present experiment only the two lowest-energy branches could be detected due to the restricted excitation frequencies available.

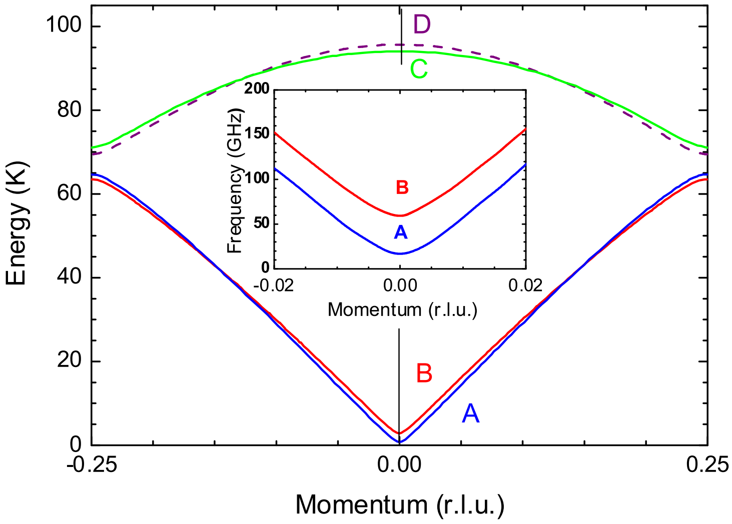

Figure 3.13.: *Dispersion relation of the magnetic excitations along the chain direction at $B = 0$. The inset shows the low-energy part of the magnetic-excitation dispersion in the vicinity of $k = 0$.*

The best agreement between the ESR data and calculations was obtained using the parameters $\tilde{J}_1 = \tilde{J}_3 = 105$ K, $\tilde{J}_2 = 110$ K, $\tilde{J}_4 = 96$ K, and $\tilde{J}_N = 0.8$ K for the alternating NN ($\tilde{J}_{1-4}$) and NNN ($\tilde{J}_N$) interactions, respectively. The values of the exchange integrals agree with the estimated values for the superexchange [65] in (6MAP)CuCl$_3$. In Fig. 3.14, the calculated frequency-field dependence of the resonance excitations for the four-center $S = \frac{1}{2}$ chain model with the chosen set of parameters is presented. One can see that the low-energy ESR branches of the model agree well with the observed experimental features (Fig. 3.11). The predicted high-energy ESR modes C and D (Figs. 3.13 and 3.14) may be the subject of future ESR experiments.

Interestingly, regardless of the microscopic origin of the alternation and of the exact values of the alternating parameters, the gap values between the lower (A and B) and upper modes (C and D) (Fig. 3.13) are mainly determined by the NNN interaction [57]. The value obtained for the NNN exchange interaction, $J_{NNN} = 0.8$ K, is about two orders of magnitude smaller than the NN exchange interactions. This value is well below the resolution limit of other spectroscopic techniques of this spectral range, but perfectly fits the resolution parameters of standard ESR techniques. Thus, ESR can serve as a very sensitive tool to detect details of the excitation spectrum in alternating spin chains due to NNN interactions.

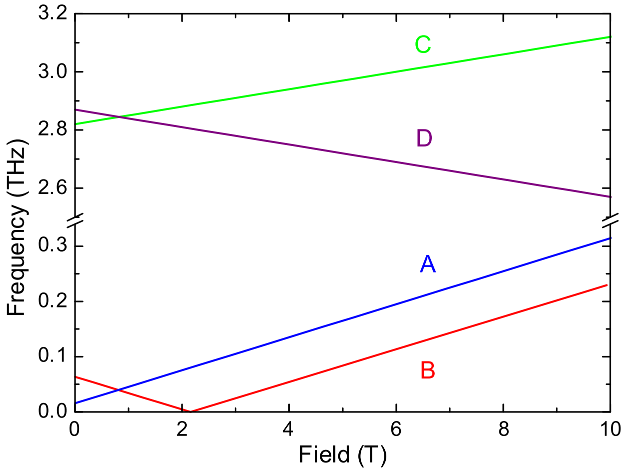

Figure 3.14.: *The frequency-field dependence of magnetic excitations of the four-center XY $S = \frac{1}{2}$ chain model.*

The appearance of the energy-gap in the low-energy ESR spectrum should manifest itself also in a peculiar behavior of the magnetic susceptibility at temperatures $T \propto \Delta_{1,2}$. The temperature dependence of the magnetic susceptibility (down to 1.8 K) is shown in Fig. 3.15 together with the calculated results (based on the four-center chain model, Fig. 3.12) using the obtained parameters. As follows from the model, the presence of the low-energy gaps, observed in our ESR experiments, should determine the low-T part of the magnetic susceptibility, while the high-energy branches (and the related gaps) determine the magnetic susceptibility at high temperatures. The main features of the calculated susceptibility (low-temperature maximum, a pronounced dip at $T \approx 13$ K, and a broad maximum at $T \approx 70$ K) are consistent with the experimental data, suggesting the validity of the four-center spin-chain model with NNN interaction. Notice that this simplified theoretical estimate for the temperature dependence of the magnetic susceptibility can serve only as illustration of the qualitative similarity of the experimental and model features. Detailed theoretical studies of the four-center AF spin chain with NN and NNN interactions, unfortunately, are not available now, but would be necessary to precisely determine the relevant parameters (exchange integrals, magnetic anisotropy, etc.) of the studied compound.

What is the origin of the proposed interaction alternations? A possible cause for that might be a spin-Peierls transition. However, a thorough search for possible superstructures by synchrotron x-ray diffraction, carried out at the MAGS beamline at the Helmholtz-Zentrum Berlin, gave no indication for

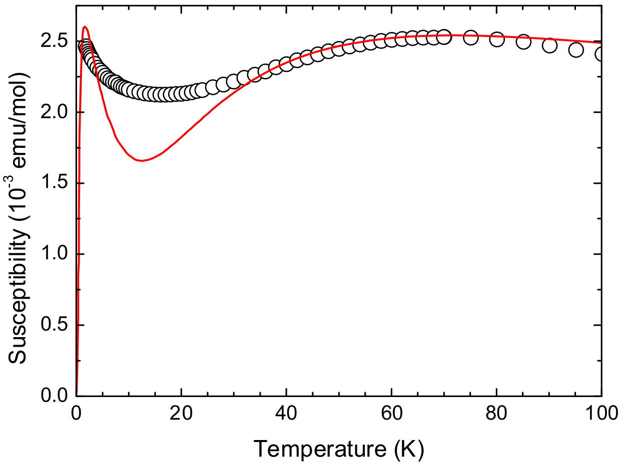

Figure 3.15.: *Temperature dependence of the magnetic susceptibility of (6MAP)$CuCl_3$. Experimental data are shown by open circles, while the solid line corresponds to the calculated result by use of the four-center XY model with the same set of parameters as in Figs. 3.13 and 3.14.*

a structural anomaly (which would suggest a spin-Peierls transition) down to 1.5 K.

There are two previously known compounds with an alternating $S = \frac{1}{2}$ Heisenberg-chain structure, that are structurally uniform at room temperature: Cu(4-methylpyridine)$_2$$Cl_2$ [$CuCl_2$(mepy)$_2$] [74] and Cu(N-methylimidazole)$_2$$Br_2$ [$CuBr_2$(midz)$_2$] [75]. The alternation parameter (ratio of weaker to stronger interactions strength was found to be 0.6(1) for $CuCl_2$(mepy)$_2$ and 0.4(1) for $CuBr_2$(midz)$_2$. Although due to the tendency of these materials to twin in neither case the methyl-hydrogen ions could be crystallographically located, the uniform nature of the chains at room temperature is verified. Studies of the dielectric constants of the two compounds clearly revealed anomalies near 50 K for $CuCl_2$(mepy)$_2$ [76] and at 50 and 105 K for $CuBr_2$(midz)$_2$ [77]. These data were interpreted as freezing of the methyl-group rotations which could induce a slight twisting of the copper octahedra so and produce an alternating variation of the exchange pathways. Magnetic studies of these materials [78, 79] revealed the characteristic maximum in the magnetic susceptibility as well as a gaped ground state [similar to that observed in (6MAP)$CuCl_3$].

While the methyl groups in (6MAP)$CuCl_3$ are ordered at room temperature, the hydrogen atoms of the amino groups are disordered [65], leaving open the possibility that the observed magnetic behavior arises from a similar freezing transition. A potential signature of the proposed scenario is the pronounced field-independent maximum in the specific heat at ~ 2.2 K (Fig. 3.8), which would correspond to a low-temperature Schottky anomaly due to the hydrogen-position order. This assumption is supported from the estimated value of the barrier energy which correlates with the characteristic temperature, $T \approx 5$ K, at which the second ESR mode appears. It is notable that the variations of the exchange strengths in (6MAP)CuCl$_3$ are much smaller than those observed in CuCl$_2$(mepy)$_2$ and CuBr$_2$(midz)$_2$.

3.4. Summary

In this work, ESR studies of the low-energy excitation spectrum in the $S = \frac{1}{2}$ chain system (C$_6$H$_9$N$_2$)CuCl$_3$ are presented. Two gaped modes with asymmetric (with respect to the $h\nu = g\mu_B B$ line) resonance positions have been observed in the low-temperature ESR spectrum, reflecting the discrepancy with the simple $S = \frac{1}{2}$ Heisenberg AF chain model employed for this compound previously [65]. The unusual ESR spectrum is interpreted in the frame of the recently developed theory for $S = \frac{1}{2}$ chains [57], strongly suggesting a multiplication of the magnetic unit cell and the presence of NNN interactions in this compound. This suggestion is supported by model calculations for the magnetic susceptibility of (C$_6$H$_9$N$_2$)CuCl$_3$, revealing a good qualitative agreement with experiment.

4. High-field spin dynamics in the sine-Gordon spin-$\frac{1}{2}$ chain material Cu-PM

4.1. Spin dynamics in spin-$\frac{1}{2}$ chains with alternating g-tensor or DM interaction

As mentioned in Chapter 3, the fundamental properties of the isotropic $S = \frac{1}{2}$ HAF chain can be drastically changed in the presence of small perturbations. The effect of an alternating g-tensor and/or the Dzyaloshinskii-Moriya (DM) interaction is worthy to attention. In the presence of such interactions, the application of a uniform external magnetic field B induces an effective staggered field $h = \mathbf{c}B$, which is approximately perpendicular to B. The coefficient $\mathbf{c}$ depends on the orientation of the applied magnetic field and the direction and magnitude of the DM interaction. The Hamiltonian of a spin-$\frac{1}{2}$ HAF chain in a staggered magnetic field can be written as

$$H = \sum J(\vec{S}_i \cdot \vec{S}_{i+1} - g\mu_B B S_i^z - (-1)^i \mu_B h S_i^x), \tag{4.1}$$

where the first term is the nearest-neighbor exchange interaction, the second term describes the spin interaction with the external magnetic field B, and the last term is the spin interaction with the effective transverse staggered field h [80]. It was shown, that the effective transverse staggered field in the presence of a magnetic field results in the opening of an energy gap, $\Delta \sim B^{2/3}$. The field-induced energy gap leads to a number of prominent features incompatible with a simple spin-$\frac{1}{2}$ HAF chain model. A number of physical realizations of the sine-Gordon spin system are known up to date [3, 71, 81–84]. Among others, copper benzoate [81] and copper pyrimidine dinitrate [71] are the most intensively studied materials.

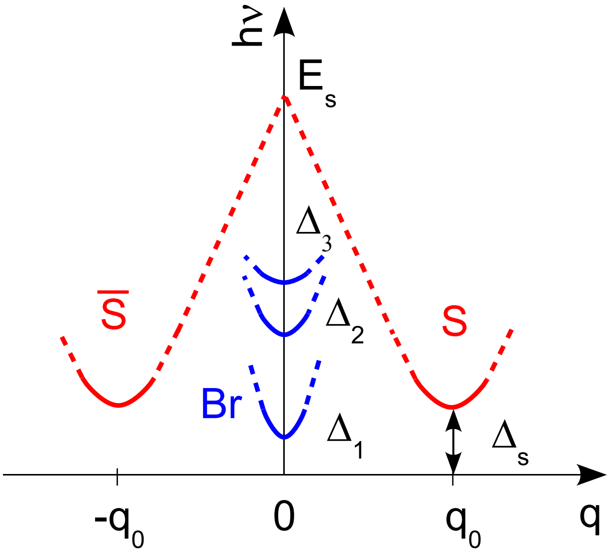

Figure 4.1.: *Illustration of low-energy excitations in the quantum SG model. Soliton, antisoliton, and breathers are labeled as S, $\bar{S}$, and Br, respectively.*

Using a low-energy effective theory, Oshikawa and Affleck [80,85] demonstrated that the system described by Eq. (4.1) can be mapped onto the quantum sine-Gordon (SG) model in a magnetic field with the Lagrangian density

$$L = \frac{1}{2}\left[\frac{\partial^2\phi}{\partial t2} - v_s^2\frac{\partial^2\phi}{\partial x^2}\right] + \lambda(h)\cos(2\pi R\tilde{\phi}), \tag{4.2}$$

where ϕ is a canonical Bose field, $\tilde{\phi}$ is the dual field, R is the compactification radius, v_s is the dimensionless spin velocity, and $\lambda(h)$ is a coefficient which cannot be calculated exactly [86]. Fields ϕ and $\tilde{\phi}$ are scalar fields, which relate to the density and to the current of quasi-particles in the bosonization method [87], respectively. Both R and v_s are known exactly as functions of $\widetilde{H} = g\mu_B B/J$ from the solutions of Bethe-ansatz equations [80].

The sine-Gordon theory, Eq. (4.2) is of interest as an integrable nonlinear differential equation featuring soliton solutions. On the quantum level the SG model is exactly solvable resulting in the precise theoretical description of many observable properties and physical parameters of sine-Gordon-like magnetic materials. In particular, it predicts that the excitation spectrum of a sine-Gordon system consists of solitons, antisolitons, and bound states of solitons and antisolitons, so-called breathers. The energy structure of these elementary excitations contributing to the low-energy spin dynamics is sketched in Fig. 4.1. Because of the staggered field h the excitation spectrum exhibits incommensurate and commensurate gaped modes, which is in contrast to the pure Heisenberg case where the spectrum remains gapless.

The incommensurate shift $q_0 = 2\pi m(B)$ is determined by the total magnetization per spin m, exactly known as a function of the external field. The quantum sine-Gordon field theory provides an expression for the soliton gap Δ_s, which is applicable in a wide magnetic field range up to $g\mu_B B \propto J$ [80]:

$$\Delta_s = J \frac{2\Gamma(\frac{\xi}{2})v_F}{\sqrt{\pi}\Gamma(\frac{1+\xi}{2})} \left[\frac{g\mu_B B}{Jv_F} \frac{\pi\Gamma(\frac{1}{1+\xi})\mathbf{c}A_x}{2\Gamma(\frac{\xi}{1+\xi})} \right]^{\frac{1+\xi}{2}} \propto B^{2/3}. \tag{4.3}$$

Here, the parameter $\xi = \left(2/(\pi R^2) - 1\right)^{-1}$ [80]. The amplitude A_x is a function of $\widetilde{H}$ and has been computed numerically [88].

The breathers correspond to commensurate modes at $q = 0$ and have a hierarchical structure, where the gap of the n-th breather is described as

$$\Delta_n = 2\Delta_s \sin\left(\frac{n\pi\xi}{2}\right). \tag{4.4}$$

The number N of breather branches is limited by $N < [\xi^{-1}]$. At zero magnetic field, the first breather Br_1 is degenerate with the soliton-antisoliton doublet S, $\bar{S}$. At finite field this degeneracy is lifted so that Br_1 becomes the lowest excitation and gives the strongest contribution to the magnitude of the gap observed in specific-heat experiments [71]. The sine-Gordon model predicts two more „heavy“ breathers Br_2 and Br_3 to exist in the relevant frequency-field range.

This picture appears to be reasonable as long as the induced field h is very small so that it affects the parameters R and v_s negligibly. With the application of a high magnetic field, comparable to the exchange constant, one approaches the incommensurate-commensurate transition to the saturated state and the spin velocity thus tends to zero [80]. Unlike the weak-field regime, for which analytical results have been obtained, the saturation region has so far been studied only numerically [89–91]. The calculated magnetic-field dependence of the gap is shown in Fig. 4.2 for different values of the proportionality constant **c** [91]. The numerical data reveal a nonmonotonic dependence of the field induced gap with a pronounced minimum near the saturation field. Curiously, this minimum is pronounced only for small values of **c** and disappears when it is above some critical value. Such nonmonotonic behavior of the gap is due to the competition between the applied field and the induced staggered field. Above the saturation field, the field dependence of

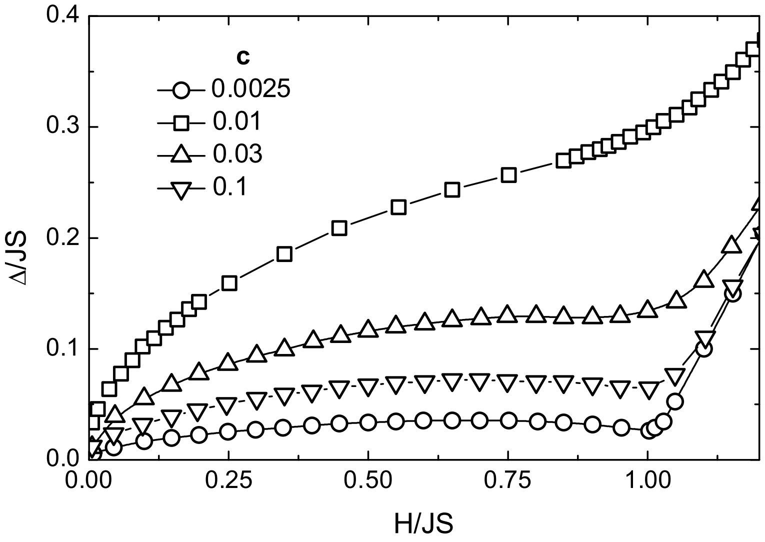

Figure 4.2.: *The lowest spin gap in the spin-$\frac{1}{2}$ sine-Gordon chain as a function of B for several values of the proportionality constant **c**. The data were obtained using exact diagonalization technique. After Ref. [91].*

the gap tends asymptotically to the linear behavior $\Delta \propto (B - B_{sat})$, which corresponds to ordinary spin waves (magnons) in the fully polarized spin state.

For the first time, the remarkable changes in the excitation spectrum of the sine-Gordon spin chain in the vicinity of the saturation field have been experimentally observed by Nojiri et al. [92]. The frequency-field dependence of ESR excitations in copper benzoate was measured at $B\|c$, revealing only qualitative agreement with results of density matrix renormalization group (DMRG) calculations (available for copper benzoate at $B\|c''$ [89]).

In this work, the excitation spectrum of $[\mathrm{PM{\cdot}Cu(NO_3)_2(H_2O)_2}]_n$, a spin-$\frac{1}{2}$ Heisenberg chain with alternating g-tensor and DM interactions, has been probed in magnetic fields up to 63 T. Pronounced changes in the ESR spectrum are observed in the vicinity of the saturation field, $B_{sat} = 48.5$ T [93], clearly indicating a transition from the soliton-breather to the magnon state. Experimental data are compared with corresponding results of DMRG calculations. Excellent qualitative agreement is found.

4.2. Crystal structure, magnetic, and thermodynamic properties of the sine-Gordon spin chain material $[\mathrm{PM{\cdot}Cu(NO_3)_2(H_2O)_2}]_n$

As mentioned, copper pyrimidine dinitrate $[\mathrm{PM{\cdot}Cu(NO_3)_2(H_2O)_2}]_n$ (hereafter Cu-PM; PM = pyrimidine $C_4H_4N_2$) is one of the best realizations of the quantum sine-Gordon spin-chain model known to date. Cu-PM crystallizes in a monoclinic structure belonging to the space group $C2/c$ with four formula units per unit cell [71]. The lattice constants obtained from single-crystal X-ray diffraction are $a = 12.404$ Å, $b = 11.511$ Å, $c = 7.518$ Å, and $\beta = 115.0$ deg. The low-temperature crystal structure is essentially the same as at room temperature. The crystal structure suggests that the exchange interaction between neighboring Cu^{2+} ions should have a one-dimensional nature (Fig. 4.3).

The Cu^{2+} ions form chains running parallel to the ac diagonal. The magnetic exchange, J, between nearest-neighbor Cu^{2+} spins are formed by the N-C-N moieties of pyrimidine. The Cu^{2+} environment is a distorted octahedron, built from an almost square N-O-N-O equatorial plane and two oxygens in the axial positions (Fig. 4.3). In this approximately tetragonal local symmetry, the local principal axis of each octahedron is tilted alternately from the ac plane by 29.4 deg. This leads to the staggered inclination of the principal axes of the g-tensor. Since there is no inversion symmetry at the middle point of two adjacent spins along the chain direction, the DM interaction can exist.

Single crystals of Cu-PM have been grown by slow evaporation of the equimolar aqueous solution of copper nitrate and pyrimidine [95]. For the

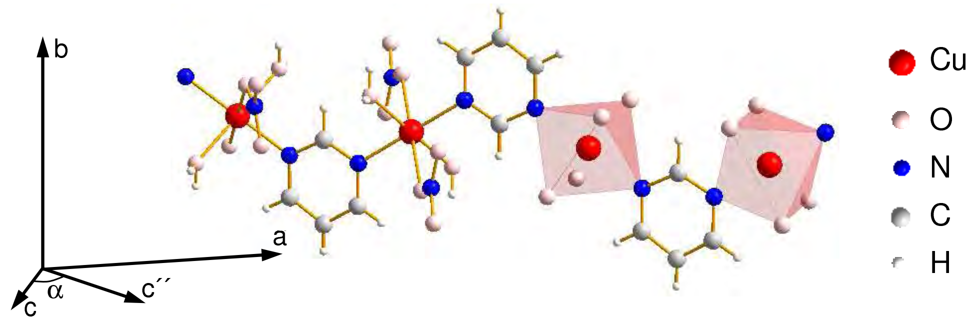

Figure 4.3.: *Schematic view of the room-temperature crystal structure of* $[\mathrm{PM{\cdot}Cu(NO_3)_2(H_2O)_2}]_n$ *[94]. Local principal axes of octahedrons surrounding the central* Cu^{2+} *ions alternate along the chain direction resulting in a staggered g-tensor.*

ESR measurements the samples were oriented along the characteristic orientation c'', which is characterized by the maximal value of the staggered magnetization for Cu-PM [71]. The effective value of the g-factor along the c'' direction was determined at room temperature, $g = 2.24$ [56]. High-quality single-crystals of Cu-PM with typical sizes of 3x3x5 mm^3 were used.

Cu-PM is magnetically described as an $S = \frac{1}{2}$ HAF spin chain with the exchange constant $J/k_B = (36 \pm 0.5)$ K, extracted from the single-crystal susceptibility [71] and confirmed by magnetization measurements [93]. No indications are found for three-dimensional long-range ordering down to 0.3 K. Because of that it was concluded that the interchain interaction is smaller than the intrachain interaction by at least a factor of 10^{-2}. The crystal structure (namely the tilted local anisotropy axis of octahedrons) of Cu-PM constitutes the prerequisite for the appearance of a staggered field, when an external magnetic field B is applied. Consequently, the Hamiltonian of the present system in magnetic field can be described by Eq. (4.1).

In accordance with the SG model, the magnetic susceptibility is represented as

$$\chi = \chi_i + \chi_s \, . \tag{4.5}$$

χ_i is the uniform magnetic susceptibility for a spin-$\frac{1}{2}$ HAF spin chain without a staggered field [68] and χ_s is the staggered susceptibility given by

$$\chi_s \approx 0.27 \left(\frac{N_A g^2 \mu_B^2}{4 k_B T} \right) \left[\ln \left(\frac{J}{k_B T} \right) \right]^2 . \tag{4.6}$$

The staggered susceptibility can be well approximated by a Curie law for $T \ll J$ where the logarithmic term is almost constant $\chi_s \propto C_s/T$. Thus, a Curie term in the magnetic susceptibility of a SG spin chain arises from the temperature dependence of the staggered susceptibility, i.e., a Curie term is intrinsic to the present system.

The temperature dependence of the magnetic susceptibility for Cu-PM was measured at different orientations of the magnetic field [71]. Typical curves of the magnetic susceptibility are shown in Fig. 4.4. The susceptibilities exhibit broad peaks at $T_{max} \approx 23$ K indicating the low-dimensional character of the spin interactions in the material, whereas χ for $\alpha = 53$ deg (which is close to $c'' \approx 48$ deg) increases rapidly below 7 K, obeying a Curie law. For $\alpha = 143$ deg only a slight increase at lowest temperatures occurs. Such behavior of the magnetic susceptibilities χ is nicely described by Eq. (4.5). The Curie constant C_s depends strongly on the field direction when applied in the ac plane. Two characteristic directions a'' and c'' were determined corresponding to the minimal and maximal values of C_s, respectively. Such anisotropy of the

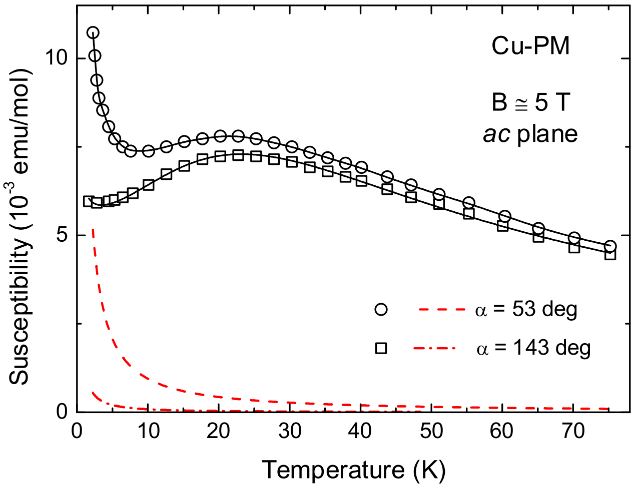

Figure 4.4.: *Temperature dependence of the magnetic susceptibility for orientations close to* a'' *(*$\alpha \approx 138$ *deg) and* c'' *(*$\alpha \approx 48$ *deg) directions and corresponded fits according to Eq. (4.5). The angle* α *is the angle between the applied magnetic field and the c axis. The staggered susceptibilities shown by dashed lines are very pronounced for one direction, and vanishes almost completely for the other. After Ref. [71].*

magnetic susceptibility implies that the staggered field becomes maximum for $B\|c''$ and minimum for $B\|a''$ in the *ac* plane. Therefore, the favourable direction c'' at an angle of about 48 deg with respect to the *c* axis was selected for further investigating field-induced effects.

If an external magnetic field induces an energy gap in the excitation spectra, it should be observable in specific-heat measurements. Indeed, this statement was supported by specific-heat data [71]. The temperature dependence of the specific heat for Cu-PM is shown in Fig. 4.5a. In finite fields and at low temperatures, C_m is suppressed below its zero-field value. As the temperature increases, $C_m(B,T)$ rises above the zero-field curve, before settling back down to it at high temperatures. Such behavior indicates a transfer of spectral weight from low to higher energies, and is a clear signature of a field-induced gap Δ. These temperature dependences of the specific heat for Cu-PM are in very good agreement with the sine-Gordon model [86] and were well fitted using only two parameters, namely the magnetic-field dependent spin-wave velocity v_s and the gap Δ [71].

As it is shown in Fig. 4.5b, the dependence of the energy gap on the magnetic field is well described by $\Delta \propto B^{2/3}$, proving the expectation. A similar set of parameters describes the field and orientation dependence of the susceptibility and the specific heat very well, providing clear experimental evidence for

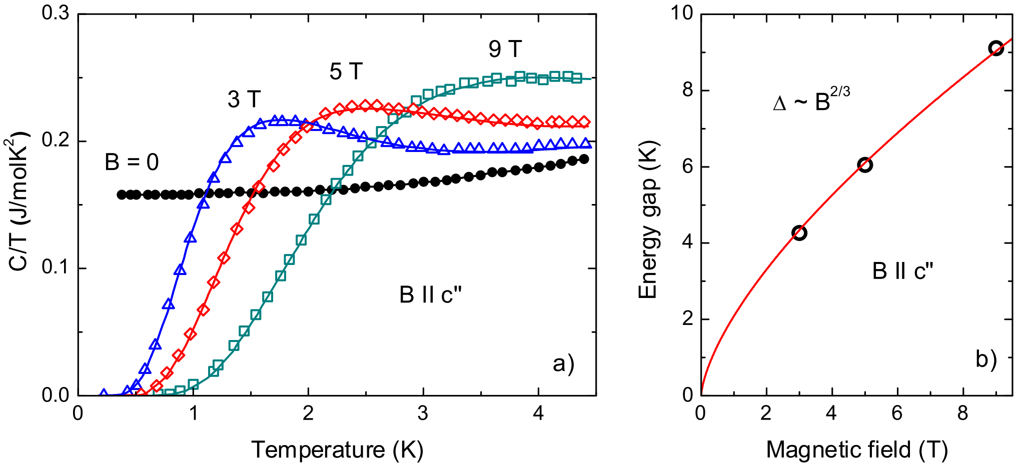

Figure 4.5.: *a) Temperature dependence of the specific heat of Cu-PM for different values of the applied magnetic field* $B \| c''$ *i.e., along the orientation with maximum staggered field. b) Energy gap in Cu-PM vs magnetic field as determined from specific-heat measurements. Red line corresponds to results of the sine-Gordon model [86]. After Ref. [71].*

the direct relation between the field-induced gap and the staggered susceptibility predicted by theory.

A detailed information about the magnetic-excitation spectrum can be precisely obtained by high-resolution ESR spectroscopy. Since ESR measurements test excitations only at $q = 0$, the breathers can be observed by ESR, whereas the soliton and antisoliton corresponding to the excitations at $q = q_o$ cannot be observed directly. Nevertheless, in previous ESR experiments the soliton resonance labeled E_s in Fig. 4.1 could be observed [56]. This corresponds to the excitation energy at $q = 0$ that connects to the soliton and antisoliton at $q = \pm q_o$. The energy of the soliton resonance is given by

$$E_s \approx \sqrt{\Delta_s^2 + (g\mu_B B)^2}\,. \tag{4.7}$$

The soliton resonance and the breathers up to the third order are the main excitations that are predicted by the quantum SG field theory. ESR measurements performed in magnetic fields up to 25 T gave a more detailed picture of the low-energy excitation spectrum of Cu-PM [56]. The frequency-field dependences of observed ESR modes in Cu-PM are shown in Fig. 4.6. A signature of soliton and three breathers were revealed. In addition to the soliton and breather modes, a few more modes were resolved, labeled C1 − C3 (which correspond to the edges of the soliton-breather continuum) and mo-

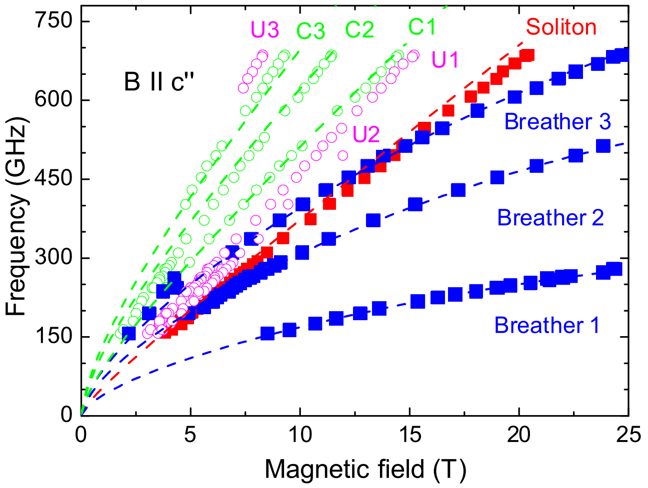

Figure 4.6.: *Field dependence of the observed ESR modes in Cu-PM. Experimental data are denoted by symbols, and lines correspond to results of calculations using the sine-Gordon theory. After Ref. [56].*

des $U1 - U3$. The origin of the modes $U1 - U3$ is not clear at the moment. It might be related to bound states due to topological edge effects [96, 97]. Noticeably, the experimental results are successfully described by the quantum SG field theory with only one adjustable parameter **c** (Fig. 4.6).

An experimental observation of the crossover to the regime where the SG model breaks down is an important problem in view of its relevance to a confirmation of the theoretical predictions. The previous ESR study of Cu-PM has been performed in magnetic field up to 25 T [56], which is below the critical field. In this work, ESR measurements were extended in higher fields up to 63 T.

4.3. Excitation spectrum in Cu-PM in the vicinity of the saturation field

ESR experiments of Cu-PM were performed using the pulsed-field ESR spectrometer equipped with VDI diodes as tunable sources of millimeter-wave radiation. A 8.5 MJ/70 T magnet was employed to generate pulsed magnetic fields with pulse-field rise time of 35 ms and full-pulse duration of about 200 ms. DPPH was employed for calibration of the magnetic field, which was applied along the c'' direction of Cu-PM. A typical ESR spectrum taken in Cu-PM at temperature of 1.9 K and frequency of 297.6 GHz is shown in Fig. 4.7.

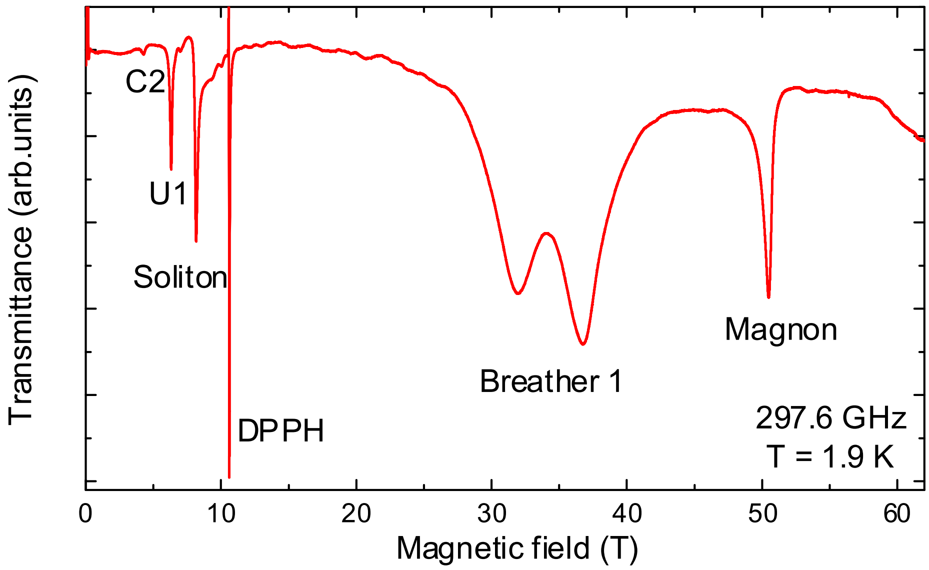

Figure 4.7.: *The ESR transmission spectrum of Cu-PM, taken at a frequency of 297.6 GHz at* $T \approx 1.9$ *K. The magnetic field was applied along the* c'' *axis, which is characterized by the maximal value of the staggered magnetization.*

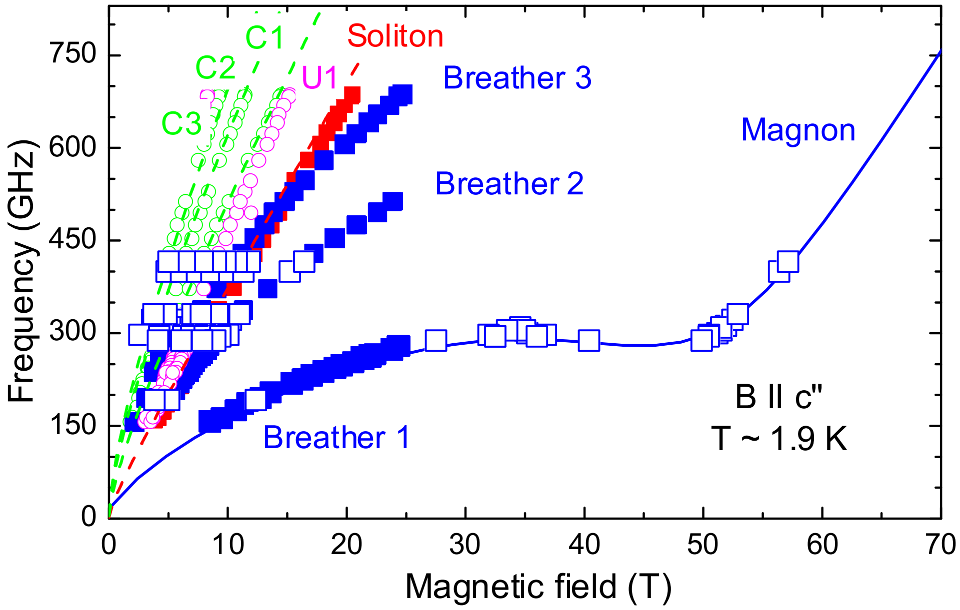

Figure 4.8.: *The frequency-field dependence of ESR modes observed in the present study (open squares) shown together with the data from Ref. [56]. The solid line corresponds to the result of DMRG calculations.*

The low-field part of the spectra agrees nicely with the previously observed modes [56]. For fields $B > 25$ T, a nonlinear behavior in the frequency-field diagram (Fig. 4.8) was observed for the first breather mode. The magnetic-field dependence of the field-induced gap in Cu-PM was studied numerically by means of DMRG techniques. The calculations (number of sites $L = 200$) were performed by S. Manmana (group of Prof. F. Mila, Institute of Theoretical Physics, Lausanne, Switzerland). The used model is a HAF spin-$\frac{1}{2}$ chain in the magnetic field Eq. (4.1) with staggered transverse field $h = 0.083B$. Results of the calculations are shown in Fig. 4.8 by the solid line. Excellent agreement with our experimental data is found. As mentioned, the application of a uniform external field induces an effective transverse staggered field $h \propto H$, which opens an energy gap $\Delta \propto B^{2/3}$. At $B \approx J/g\mu_B$ the frequency-field dependence of the first breather mode exhibits a change of its slope, resulting in a broad maximum at approximately 35 T. This behavior can be explained by a reduction of the effective transverse staggered field at high magnetic fields and, correspondingly, by an increase of the uniform magnetization [89, 91]. At $B > B_{sat} = 48.5$ T, the system is in the fully spin-polarized state and the excitation spectrum is formed by ordinary magnons. Interestingly, the effective transverse staggered field does not vanish completely at $B = B_{sat}$, preventing the excitation gap from closing even at very high magnetic fields, when the sine-Gordon model does not hold any longer. This property appears to be a general feature of the high-field excitation spectrum of quantum spin-$\frac{1}{2}$ chain systems with alternating g-tensor and/or Dzyaloshonskii-Moriya interactions.

4.4. Summary

In summary, the frequency-field diagram of magnetic excitations in Cu-PM, a material containing $S = \frac{1}{2}$ AF chains with alternating g-tensor and DM interaction, has been studied in pulsed magnetic fields up to 63 T. A minimum of the energy gap in the vicinity of the saturation field associated with a transition from the sine-Gordon region (with soliton-breather elementary excitations) to a spin-polarized state (with magnon excitations) was observed. This interpretation is fully confirmed by the quantitative agreement over the entire field range of the experimental data with the DMRG investigation of the spin-$\frac{1}{2}$ Heisenberg chain with staggered transverse field.

5. Magnetic excitations in the spin-$\frac{1}{2}$ ladder compound $(C_5H_{12}N)_2CuBr_4$

5.1. Spin-ladder model: a brief introduction.

The experimental realization of quantum spin-$\frac{1}{2}$ systems with a ladder-like structure has stimulated intense interest in low-dimensional magnetism. Apart from the possible relevance to high-temperature superconductivity [98, 99], the interest in spin ladders was motivated by their rich temperature-field phase diagram affected by quantum fluctuations.

Generally, spin ladders consist of parallel chains with intrachain (leg) exchange strengths $J_{\|}$, which are linked to each other by a second (rung) interaction $J_{\perp}$. A two-leg spin ladder (Fig. 5.1) can be described using the Hamiltonian

$$\mathcal{H} = J_{\|} \sum_{i,j=1,2} \mathbf{S}_{i,j}\mathbf{S}_{i+1,j} + J_{\perp} \sum_{i} \mathbf{S}_{i,1}\mathbf{S}_{i,2} + g\mu_B B \sum_{i,j=1,2} \mathbf{S}_{i,j}\,, \tag{5.1}$$

where $J_{\perp}$ and $J_{\|}$ are isotropic exchange interactions along the ladder rungs and legs, respectively, and B is an applied magnetic field.

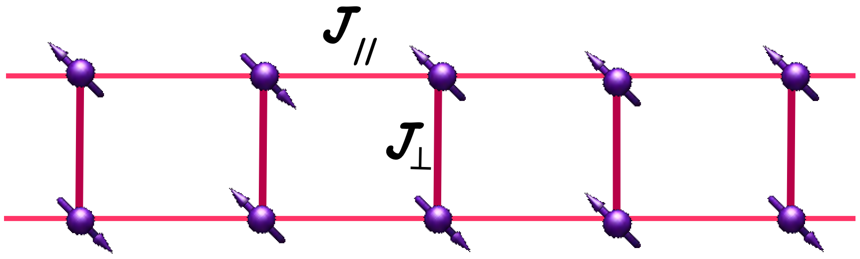

Figure 5.1.: *Schematic sketch of a two-leg spin ladder with leg and rung exchange coupling $J_{\|}$ and $J_{\perp}$, respectively.*

In the case of strong coupling, $J_\perp \gg J_\parallel$, the two-leg ladder can be mapped onto a single spin-$\frac{1}{2}$ chain in the following way [100]. At each rung two spins $S_{i,1}$ and $S_{i,2}$ are either in a singlet state $|s\rangle = (|\uparrow\downarrow\rangle - |\downarrow\uparrow\rangle)/\sqrt{2}$ or in one of the triplet states: $|\downarrow\downarrow\rangle$, $(|\uparrow\downarrow\rangle + |\downarrow\uparrow\rangle)/\sqrt{2}$, $|\uparrow\uparrow\rangle$. Applying a magnetic field moves the $|\uparrow\uparrow\rangle$ component of the triplet closer to the singlet ground state $|s\rangle$, such that for a strong-enough magnetic field these states create a new effective spin-$\frac{1}{2}$ state. It is thus possible, for $J_\perp \gg J_\parallel$, to retain only these two states for all the magnetic field range between B_c, when the gap is closed, to B_{sat}, when the ladder is completely magnetized (fully spin polarized state).

Then, the original Hamiltonian (5.1) can be projected on the new singlet-triplet subspace [100]:

$$|\tilde{\downarrow}\rangle = (|\uparrow\downarrow\rangle - |\downarrow\uparrow\rangle)/\sqrt{2}\,,$$

$$|\tilde{\uparrow}\rangle = |\uparrow\uparrow\rangle\ .$$

This leads to the definition of the effective $\tilde{S} = \frac{1}{2}$ operators

$$\tilde{S}_i^{x,y} = -\frac{1}{\sqrt{2}}\left(S_{i,1}^{x,y} - S_{i,1}^{x,y}\right)\ ,$$

$$\tilde{S}_i^z = S_{i,1}^z + S_{i,2}^z + \frac{1}{2}\,.$$

Expressed in term of the effective spin operators, $\tilde{S}_i$, the original Hamiltonian (5.1) becomes

$$H_{eff} = J_\parallel \sum_i \left(\tilde{S}_i^x \tilde{S}_{i+1}^x + \tilde{S}_i^y \tilde{S}_{i+1}^y + \gamma \tilde{S}_i^z \tilde{S}_{i+1}^z\right) - g\mu_B \tilde{B} \sum_i \tilde{S}_i^z + const\,. \tag{5.2}$$

The Hamiltonian (5.2) describes a single spin-$\frac{1}{2}$ chain with a fixed XY anisotropy of $\gamma = 1/2$ in an effective magnetic field

$$\tilde{B} = B - J_\perp - \frac{J_\parallel}{2}\,.$$

The gaped phase ($B < B_c$) for the spin ladder corresponds to the negatively saturated magnetized phase for the effective spin chain, whereas the gapless phase ($B > B_c$) for the ladder corresponds to the finite magnetization phase for the effective spin-$\frac{1}{2}$ chain. The field B_{sat}, where the ladder is totally magnetized, corresponds to the fully magnetized phase for the effective spin-$\frac{1}{2}$ chain. Since the critical fields, $\tilde{B}_s$, for the anisotropic spin-$\frac{1}{2}$ chain are known [101], particularly $\tilde{B}_s = \pm 3J_{\|}/2$ for $\gamma = 1/2$, one can convert them to the critical fields for the ladder and obtains

$$B_c = J_\perp - J_{\|}, \qquad B_{sat} = J_\perp + 2J_{\|} \, . \tag{5.3}$$

The single-chain Hamiltonian (5.2) can be expressed in terms of fermion operators using the Jordan-Wigner transformation. The absence of a fermion means a spin state $\left|\tilde{S}_i^z\right\rangle = -\frac{1}{2}$, whereas the presence of a fermion means $\left|\tilde{S}_i^z\right\rangle = \frac{1}{2}$. The magnetic field acts as a chemical potential for fermions, whereas the anisotropy parameter γ represents an interaction between fermions.

A one-dimensional system of interacting fermions has been shown to be well described as a Tomonaga-Luttinger liquid (LL). Although originally the Tomogama-Luttinger model [102–104] was developed for one-dimensional conductors, this formalism can be also applied for low-dimensional magnets. Some properties of the LL are the same as for Fermi liquids (for instance, the existence of a well-defined Fermi surface and the scaling behavior of the thermodynamic quantities, particularly, a linear specific-heat - temperature dependence). On the other hand, there are important differences between these models, particularly, in the presence of a two-body interaction between fermions, the ground state is no longer the filled Fermi sea but has admixtures of particle-hole-pair excitations. As a consequence, whereas elementary excitations of the Fermi liquid are quasi-particles, elementary excitations of the LL are collective modes, emerging due to the coupling of the quasi-particles. Typical signatures of the LL phase are that the correlation function exhibits a power-law decay and the excitation spectrum is gapless, i.e., there is no energy costs to excite a particle-hole pair. Low-energy excitations of the noninteracting as well as the interacting system of fermions can be described in terms of noninteracting bosons. An essential feature of the LL model is that only two parameters, the spin velocity v_s and the correlation exponent K_s, completely determine the low-energy physics.

For spin ladders in the field-induced gapless phase, the Tomonaga-Luttinger model can be applied both in the strong- and weak-coupling limit. In a fermionic language, the effect of magnetic field is considered as follows. For $B < B_c$, the spin-ladder model results in a gap and corresponds to empty fermionic bands. Above $B > B_c$, the system enters the gapless phase and fermions start to fill the energy band. This process continues until the upper critical field, B_{sat}, is reached. Increasing the field beyond B_{sat}, reopens the gap and the band is then completely filled. Close to an empty or a full band, the number of excitations compared to the fully polarized ground state becomes very small and thus, the correlation exponent K_s takes the value for noninteracting particles $K_s \to 1$ [100]. The Luttinger-liquid parameters K_s and v_s vary with the magnetic field. There are analytic expressions known for $\tilde{B} = 0$. For arbitrary values of $\tilde{B}$, exact expressions can be calculated by solving an integral equation obtained from the Bethe ansatz [37]. Using the bosonization technique one can determine a spin-spin correlation function of the ladder, which is incommensurate for $B_c < B < B_{sat}$ and exhibits a quite distinctive spectrum compared to single-chain systems. The gap and the dispersion of the excitations in the ladder are controlled by two different energy scales, $J_\perp$ and $J_\parallel$. Thus, the spin ladder is a good candidate for studying the LL phase and quantum phase transitions, where the spin gap is destroyed by the application of a magnetic field.

Ideally, spin-ladder compounds [105–113] are described in terms of a standard Heisenberg ladder Hamiltonian, including only isotropic interactions. Nevertheless, anisotropy is *always* present in real materials at some energy scale, and can be often observed, for instance, in the g factor anisotropy. Since the anisotropy can significantly modify the ground-state properties and low-energy excitation spectrum of spin ladders [114–120], theoretical and experimental studies of the anisotropy effects in spin ladders appear to be an important topic in low-dimensional magnetism. This work is devoted to ESR investigation of anisotropy in the spin-ladder material BPCB.

5.2. Crystallographic structure and magnetic properties of $(C_5H_{12}N)_2CuBr_4$

$(C_5H_{12}N)_2CuBr_4$ [$(Hpip)_2CuBr_4$ or BPCB] is known as a good realization of a two-leg spin-$\frac{1}{2}$ ladder system with antiferromagnetic interactions [108]. The optimal energy scale of the exchange interactions make $(C_5H_{12}N)_2CuBr_4$ unique, and allow a detailed investigation of quantum critical phenomena across the full phase diagram in temperature and in field up to magnetic saturation.

Bis-piperidinium copper bromide, BPCB, crystallizes in a monoclinic lattice (space group $P2_1/c$, number of formula units per unit cell $Z = 4$) with spin-$\frac{1}{2}$ Cu^{2+} ions arranged in a ladder-like structure [121]. $(C_5H_{12}N)_2CuBr_4$ has been shown to undergo a first-order structural transition near 260 K to a low-temperature structure with lattice constants $a = 24.111(5)$ Å, $b = 8.089(2)$ Å, $c = 18.448(4)$ Å, and $\beta = 99.3$ deg, that corresponds to a spin ladder packing of the $CuBr_4^{2-}$ anions [122]. The ladder extends along the a axis with 6.934 Å between Cu^{2+} spins on the same rung and 8.597 Å between rungs (Fig. 5.2). The rungs of the ladder are oriented along the c' axis with an azimuthal angle of 19.8 deg in ac plane and a polar angle of 66.6 deg from b axes [121]. They are

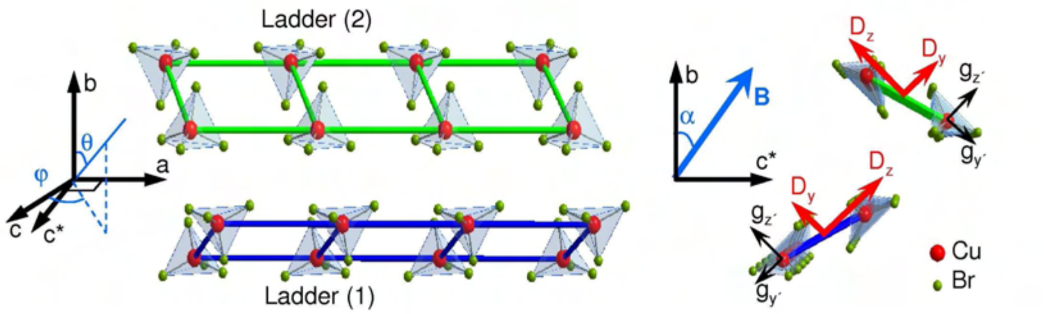

Figure 5.2.: *Schematic view of the crystal structure of BPCB [121]. Axes a, b, and c^* are mutually perpendicular. The ladders (1) and (2) are highlighted by thick blue and green lines, respectively. Black arrows define the directions of the principal axes of the g-tensors and red arrows the vectors of the effective anisotropy (see the text for details). Piperidinium groups are omitted for clarity.*

formed by adjacent flattened $CuBr_4^{-2}$ tetrahedra. Each unit cell contains two rungs of two crystallographically equivalent ladders, related by the c-glide symmetry operation. Due to the different orientations of the g-tensor, the principal axes of the two sets of ladders become magnetically inequivalent when an external magnetic field is applied along an arbitrary direction.

The magnetic exchange $J_\perp$ between the Cu^{2+} spins on the same rung are formed by two equivalent Cu-Br-Br-Cu superexchange paths with a center of inversion symmetry, while the magnetic exchange along the legs, $J_\parallel$, is mediated by a combination of hydrogen bonds and nonoverlapping Br^- orbitals, and, therefore, should be weaker. The ladder units $(Cu_2Br_8)^{4-}$ are separated by the organic $(C_5H_{12}N)^+$ cations, which are much weaker involved in the magnetic exchange interactions $J_\perp$ and $J_\parallel$ [123]. Any frustrating diagonal interaction J_F or $J_{F'}$ would involve traversing the $C_5H_{12}N$ molecule. Besides, J_F and $J_{F'}$ being associated with different bond lengths of 8.96 and 12.64 Å, respectively, suggests that J_F is larger than $J_{F'}$. The strongest interaction between the ladders, J', is expected along the direction c, and it is mediated by hydrogen bonding through the same $C_5H_{12}N$ molecules involved in the leg exchange. Besides $J_\parallel$, all another magnetic exchange interactions are expected to be sufficiently small with respect to $J_\perp$.

Exchange couplings along the rungs and legs of the ladder have been estimated as $J_\perp/k_B \approx 12.7 - 13.3$ K and $J_\parallel/k_B \approx 3.3 - 3.8$ K, respectively, depending on the experimental conditions and used technique [108–111, 123–126]. No evidence of long-range ordering was observed down to 100 mK at zero field. A signature of a very weak inter-ladder interaction ($J' < 100$ mK) were reported, leading to a transition into a field-induced magnetically-ordered phase at temperatures below 110 mK [109,110].

Crystals of $(C_5H_{12}N)_2CuBr_4$ were grown by evaporation of an aqueous solution containing a 2:1 ratio of $(C_5H_{12}N)Br$ and $CuBr_2$. A few drops of HBr were added to the solution to avoid hydrolysis of the Cu^{2+} ion [122]. High-quality single crystals of $(C_5H_{12}N)_2CuBr_4$ and its deuterated analog $(C_5D_{12}N)_2CuBr_4$, were used in our experiments.

The magnetic susceptibility of $(C_5H_{12}N)_2CuBr_4$ between 2 and 110 K is shown in Fig. 5.3, with the data below 20 K shown in the inset [122]. The behavior is dominated by a rounded maximum near 8 K and a rapid decrease at lower temperatures. The general shape of the curve is typical for low-dimensional magnetic systems with antiferromagnetic Heisenberg exchange interactions. The attempt to ascertain a possible magnetic structure of the compound has been done in Ref. [108], where the magnetic behavior was compared to theoretical predictions for a uniform spin-$\frac{1}{2}$ HAF chain, an isolated antiferromagnetic dimer, and spin ladder. Excellent agreement with the data was achieved at all temperatures using the spin-ladder model with best-fit parameters $J_\perp/k_B = 13.3$ K, and $J_\parallel/k_B = 3.8$ K.

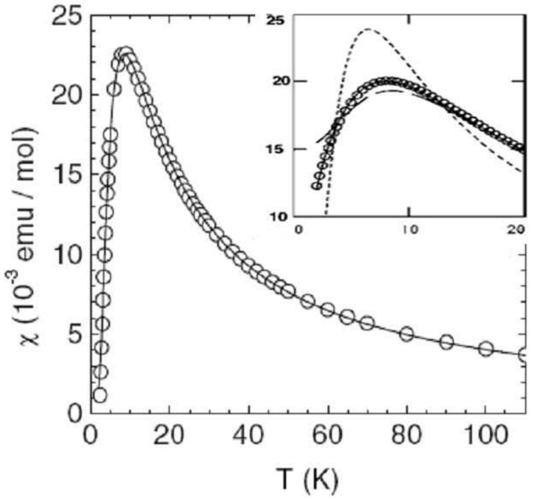

Figure 5.3.: *Magnetization vs temperature of* $(C_5H_{12}N)_2CuBr_4$ *measured in a magnetic field of 0.1 T. The solid line corresponds to a fit for a spin ladder with the parameters* $J_\perp/k_B = 11.6$ *K and* $J_\parallel/k_B = 5.5$ *K. In the inset, the dashed and dotted lines correspond to the fits to a linear-chain* ($J/k_B = 13.3$ *K) and dimer model* ($J/k_B = 10.4$ *K), respectively. After Ref. [108].*

The magnetization of BPCB measured at temperatures 0.75, 1.75, and 3.31 K is shown in Fig. 5.4. One clearly can distinguish three phase. In the low-field phase (up to 6.99 T) the ground state of BPCB is a gapped spin singlet. In fields above $B_{sat} = 14.4$ T, the systems is in a fully spin-polarized saturated state. The system is in a intermediate canted-antiferromagnetic phase at $6.99 < B < 14.4$ T. In these fields at sufficiently low temperatures BPCB appears to be in a gapless Luttinger-liquid phase with fermionic excitations, where the magnetization is proportional to the fermion density. The overall agreement between the spin-ladder model (using $J_\perp$ and $J_\parallel$) and experiment, including the symmetric double bump structure in the derivative $d(M/M_s)/dH$ is excellent.

Because both critical fields, B_c and B_{sat}, can be reached using conventional superconducting magnets, BPCB offers the unique opportunity for the detailed investigation of the field-controlled evolution of the ground-state properties in spin ladders across different regions of their phase diagram. Results of thermodynamic measurements on $(C_5H_{12}N)_2CuBr_4$ are shown Fig. 5.5 [112]. The contour plot represents the specific heat C_m/T of single crystals in magnetic fields applied parallel to the crystallographic a axis. Three regimes are clearly distinguished: the quantum-disordered (QD), the quantum-critical (QC), and the Luttinger-liquid region. The first quantum critical point at

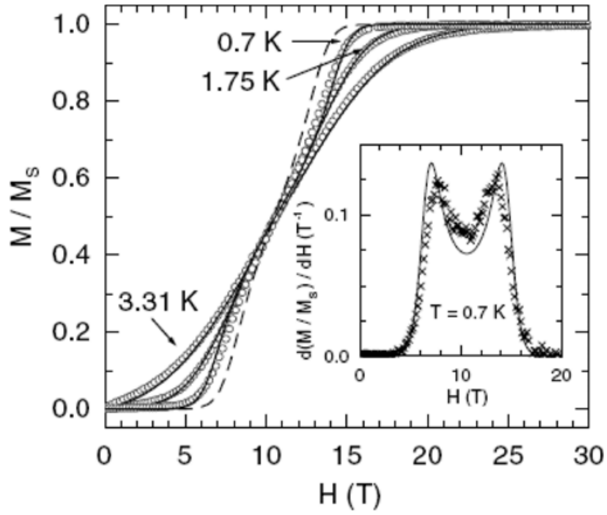

Figure 5.4.: *Field dependence of the normalized magnetization, M/M_s, of a BPCB powder sample. The lines depict the expected magnetization for a spin ladder with $J_\perp/k_B = 13.3$ K and $J_\parallel/k_B = 3.8$ K. At $T = 0.7$ K, the inflection point at $M_s/2$ is clearly visible. The inset shows the derivative of this data. After Ref. [108].*

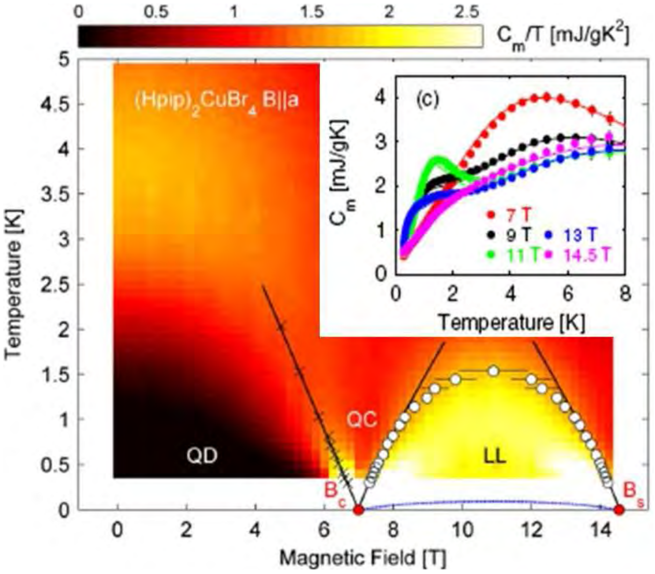

Figure 5.5.: *Temperature-field phase diagram of BPCB, showing quantum disordered (QD), quantum critical (QC), and Luttinger-liquid (LL) phases. Quantum critical points occur at B_c (closing of the spin-triplet gap Δ) and at B_{sat} (a transition into the fully spin-polarized state). The contour plot shows the magnetic specific heat as $C_m(B,T)/T$. Local maxima from the reduction of the triplet gap by the Zeeman effect are indicated by crosses. Circles denote the LL crossover based on measurements of the magnetocaloric effect, black lines are fits to extract the critical fields, and the dashed blue line indicates the onset of long-range order below 100 mK [109]. The inset shows the specific heat $C_m(T,H)$ at different magnetic fields in the range of $B_c < B < B_{sat}$. Lines are based on exact diagonalization and DMRG calculations. After Ref. [112].*

$B_c = 6.99$ T for $T = 0$ separates the low-field QD phase, with gaped triplet excitations, from a gapless phase described by the LL model with algebraically decaying spin correlations. The second quantum critical point at $B_{sat} = 14.4$ T corresponds to the transition into the fully polarized spin state. The field-induced transition from the QD state into the LL state [102–104] has been observed between B_c and B_{sat} and studied by means of nuclear magnetic resonance (NMR) [109], magnetocaloric effect [110], and thermal conductivity [113], for the first time giving comprehensive insight into the Luttinger-Liquid paradigm in spin ladders.

In the QD regime at $B < B_c$, the specific heat shows a single broad peak ($T \approx 5$ K), which is attributable to the triplet excitations in the ladder, and is exponentially activated at lower temperatures due to the presence of the spin gap Δ. For $B > B_c$, when the formation of the LL phase occurs, an additional peak develops at low temperature [112]. Well below the peak temperature, the temperature dependence of the specific heat is linear up to $B_{sat} = 14.5$ T with a field-dependent slope. For fields near the maximum of the LL dome ($\sim 9 - 13$ T), the ratio C_m/T measured appears to be the same. This temperature dependence is consistent with the presence of gapless spinon excitations with a finite velocity v_s and the slope of C_m being inversely proportional to v_s. The first peak thus occurs when the temperature is large enough to probe deviations from this linear regime. It can be taken as an estimate of the crossover to enter the LL, and is visible in Fig. 5.5 for $B_c < B < B_{sat}$ [112]. At lower temperatures, BPCB undergoes the transition into the field-induced magnetically-ordered phase [109–112], which can effectively be described employing the Bose-Einstein condensation (BEC) formalism [100, 127, 128]. The phase diagram and field variation of the order parameter determined from NMR measurements [109] are perfectly described in the framework of the LL model with no adjustment or fitting of the LL parameters. At $B > B_{sat}$, the specific heat becomes exponentially activated again due to the opening of a field-induced spin gap in the fully spin-polarized phase. Comprehensive measurements of the specific heat identify an extended region of spin Luttinger-liquid behavior over at least one order of magnitude in temperature, lying clearly above any three-dimensional physics triggered by residual interladder interactions [112]. Thus, the thermodynamic and magnetic properties of $(C_5H_{12}N)_2CuBr_4$ are in a good agreement with the model calculations, confirming the validity of the two-leg spin-ladder model.

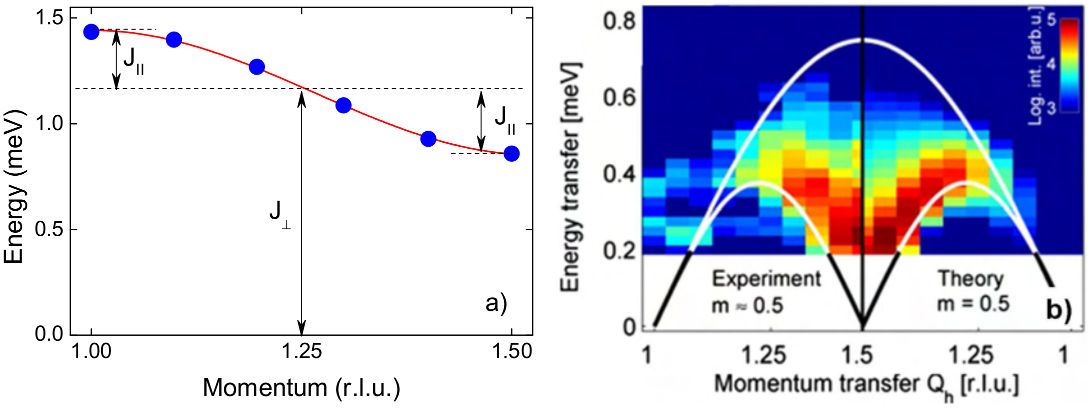

Figure 5.6.: *a) Dispersion of magnetic excitations in BPCB along the ladder axis measured at* $T = 50$ *mK in zero magnetic field. b) Excitation spectrum of BPCB in the LL phase for* $T = 250$ *mK at* $B = 10.1$ *T. The colorbar represents measured (left) and simulated (right) inelastic neutron scattering intensities. After Ref. [111].*

As a sensitive technique to probe spin correlations in the singlet ground state, inelastic neutron scattering allowed to elucidate the magnetic structure of deuterated $(C_5H_{12}N)_2CuBr_4$ [111, 123]. The observed dispersion in the QD phase is in a perfect agreement with the triplet dispersion (Fig. 5.6a), directly yielding the rung exchange $J_\perp/k_B = 12.6$ K and the leg exchange $J_\parallel/k_B = 3.2$ K. Moreover, at $B_c < B < B_{sat}$ inelastic neutron-scattering measurements [111] revealed a broad continuum of spinons excitations (Fig. 5.6b), which is strongly different from the QD and fully saturated phases. This proved the occurrence of the field-induced fractionalization of magnons into spinons entities when the system enters the LL phase. The effective inter-ladder exchange was estimated to $J'/k_B < 70$ mK [123]. This is more than two orders of magnitude smaller than $J_\perp$, confirming that $(C_5H_{12}N)_2CuBr_4$ consists of well-isolated spin ladders. This value of J' is consistent with low-temperature NMR measurements by Klanjšek et al. [109], revealing 3D magnetic order below 110 mK.

5.3. ESR experiments

The angular dependence of ESR signals measured by us at a frequency of 9.4 GHz at room temperature was found to be in good agreement with results reported by Patyal *et al.* [121], revealing the existence of two types of excitation centers with different principal axes of the g-tensor. A much more complex excitation spectrum with four ESR lines has been observed by us at low temperatures (Fig. 5.7).

In Fig. 5.8, the angular dependence of the resonance fields measured at 3.3 K with the magnetic field applied in the bc^* plane ($c^* \perp a, b$) is presented [129]. The lines have the same angular dependence both in hydrogenated as well as in deuterated crystals. Four ESR modes were observed, which is in contrast to a simple isotropic spin-ladder model. The observation of two pairs of ESR modes with a very pronounced angular dependence of their resonance positions is a clear signature of the presence of additional (anisotropic) interactions in BPCB. With decreasing temperature the ESR intensity of the modes exhibits a behavior similar to one measured at frequency of 73 GHz (Fig. 5.9). Such temperature dependence of the integrated intensity indicates that these excitations correspond to transitions inside the thermally populated triplet, which allows to apply a simplified spin-triplet model with axial and in-plane anisotropy terms (D' and E', respectively) [130].

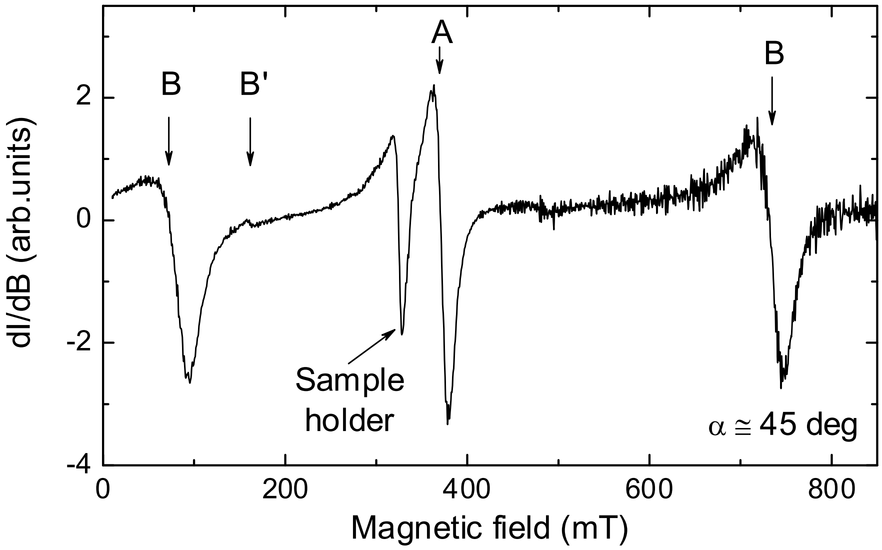

Figure 5.7.: *ESR spectrum (derivative signal) measured at 3.3 K using the X-band spectrometer with a frequency of 9.4 GHz. The magnetic field was applied at an angle $\alpha = 45$ deg to the b axes in the bc* plane (Fig. 5.11). The labels correspond to resonance positions denoted in Fig. 5.14, inset, by diamonds.*

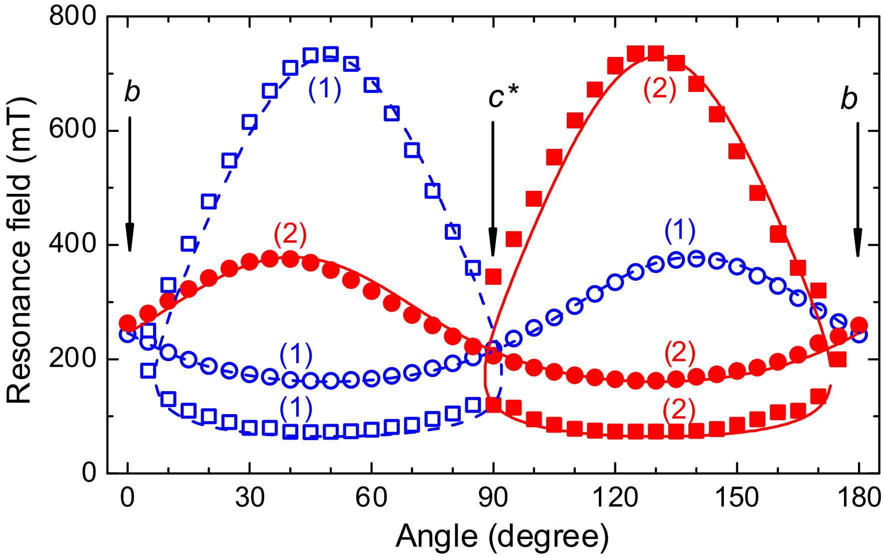

Figure 5.8.: *Angular dependence of ESR resonance fields (symbols) corresponding to the modes shown in Fig. 5.7. Symbols labeled (1) and (2) correspond to excitations originating from the ladders (1) and (2), respectively (Fig. 5.2), while the lines represent the simulation results described in the text.*

This model is based on an effective spin Hamiltonian for the triplet states in a magnetic field given by

$$\mathcal{H}_{eff} = D_x S_x^2 + D_y S_y^2 + D_z S_z^2 - \mu_B \mathbf{B} \hat{g} \mathbf{S}\,, \tag{5.4}$$

where $\hat{g}$ is the g-tensor. The effective anisotropy parameters follow from $D' = \frac{3}{2}D_z$ and $E' = \frac{1}{2}(D_x - D_y)$ [131]. The ESR angular dependence has been analyzed by employing the above Hamiltonian in the „EasySpin“ simulation package [132]. The results of the simulation are presented in Fig. 5.8 by solid lines. Good agreement with the experimental data was found for $g_{x'} = 2.065$, $g_{y'} = 2.045$, $g_{z'} = 2.29$, $D'/k_B = 0.55$ K, and $E'/k_B = -0.05$ K. The anisotropy axis D_z is tilted by 49.5 deg counterclockwise from the b axis in the bc^* plane for the ladder (1) and clockwise for the ladder (2) as shown in Fig. 5.2. The observed anisotropy is $\sim 5\%$ of the rung interaction $J_\perp$ (which is the dominating interaction in this compound) and $\sim 16\%$ of the leg interaction.

High-frequency ESR experiments were performed with the magnetic field tilted about 45° away from the b axis in the bc^* plane, where the best resolution can be achieved (Fig. 5.8). The typical spectrum of the $(C_5H_{12}N)_2CuBr_4$ at $T = 1.3$ K and the corresponding frequency-field diagram of the magnetic excitations in BPCB are shown in Figs. 5.10 and 5.11, respectively. Several important observations have been made.

First, the spin gap in the excitation spectrum was observed directly. The frequency-field diagram of the modes **E**, **F**, **G**, and **H** can be described by $h\nu = \Delta_0 \pm g\mu_B B$, where Δ_0 is the energy gap (the modes **A**, **B**, **C**, and **D** will be discussed later). This energy gap corresponds to transitions from the spin-singlet

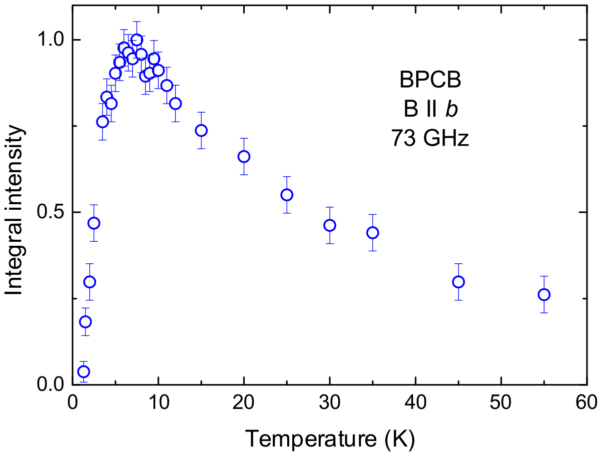

Figure 5.9.: *Temperature dependence of the integrated intensity obtained from ESR data measured at $\nu = 73$ GHz for $B \| b$.*

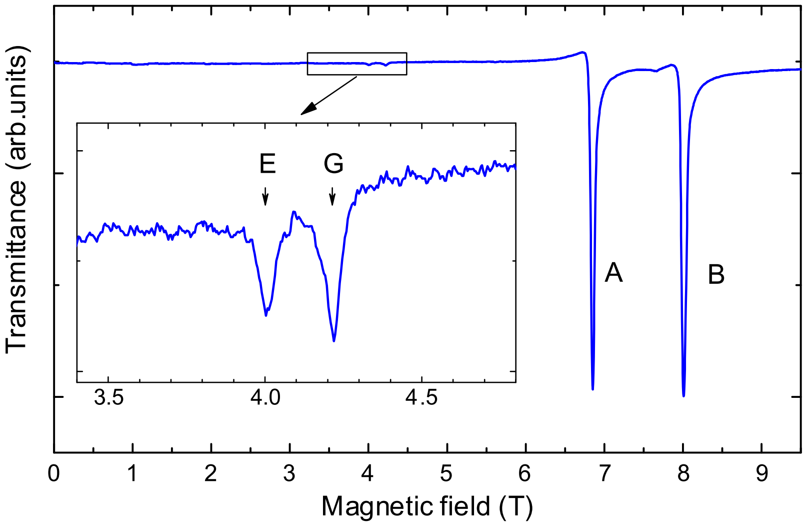

Figure 5.10.: *ESR spectrum of* $(C_5H_{12}N)_2CuBr_4$ *measured at a frequency of 220.8 GHz at* $T = 1.3$ *K for* $\alpha \approx 45$ *deg.*

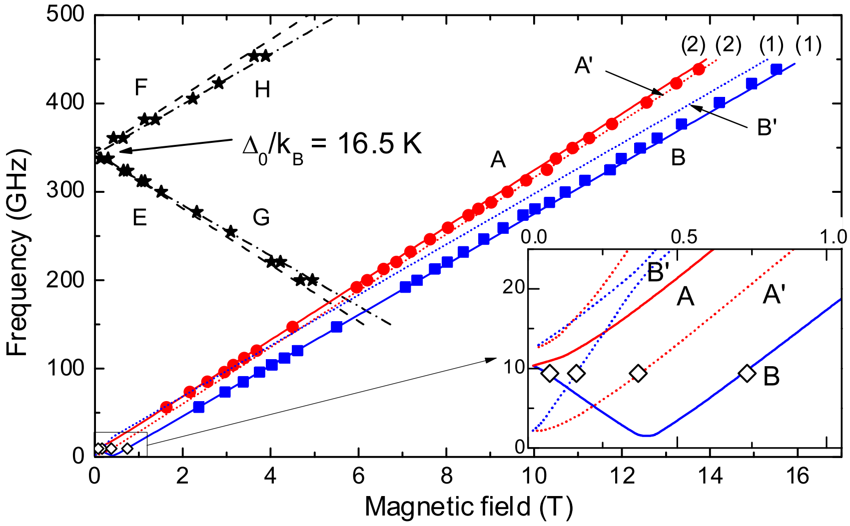

Figure 5.11.: *Frequency-field diagram of the ESR excitations in BPCB for* $\alpha \approx 45$ *deg. The modes* ***E***, ***F***, ***G***, *and* ***H*** *(dashed lines) correspond to transitions from the spin-singlet ground state to the first excited triplet states at* $k = 0$. *Lines (1) and (2) are results of calculations for transitions between the excited triplet levels corresponding to different ladders (1) and (2), respectively, using the set of parameters as described in the text. The inset shows the low-frequency low-field part of the calculated excitation diagram and the experimental data from Fig. 5.7 (shown by rhombs).*

ground state to the first excited spin-triplet states (Fig. 5.12). Such ESR transitions are normally forbidden by selection rules if the axial symmetry is preserved [131] (which is not the case of the chosen magnetic field orientation). The value of the gap at zero field is 343 GHz ($\Delta_0/k_B = 16.5$ K), which agrees well with the value measured at the center of the Brillouin zone ($k = 0$) by inelastic neutron scattering (Fig. 5.6a) [111, 123]. In most gaped spin-$\frac{1}{2}$ systems, these transitions are not observable by ESR due to an overlap of the spin-triplet excitations with the two-magnon continuum. In BPCB the onset of the two-magnon continuum (with the lowest-energy boundary estimated as $2\Delta_\pi/k_B \approx 19.2$ K, where Δ_π is the one-magnon energy gap at $k = \pi$) is at a higher energy than the one-magnon gap at $k = 0$. This difference prevents scattering of one-magnon excitations by the two-magnon continuum and allows for the observation of the gap at $k = 0$.

Second, the resonances were slightly split, yielding $g = 2.28$ and $g = 2.04$ for the mode pairs **F**, **E** and **G**, **H**, respectively. A fit of the frequency-field dependences of the observed modes revealed a zero-field splitting difference of about 3 GHz ($\sim$ 140 mK), which is a direct indication for the presence of inter-ladder interaction and consistent with results of NMR and neutron-diffraction experiments [109, 110].

Third, two well-resolved modes, **A** and **B**, with g factors 2.28 and 2.04, respectively (measured at 1.4 K), were observed in the ESR spectra at low temperatures (Fig. 5.11). Noticeably, the extrapolated field dependence of neither mode **A** nor mode **B** intersects zero at zero magnetic field. The calculated

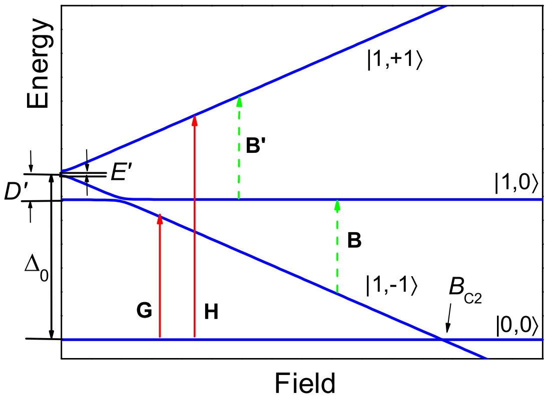

Figure 5.12.: *Schematic energy-field diagram of ESR transitions in BPCB for the ladder (1). Excitations from the ground state are represented by solid red lines (modes* ***G*** *and* ***H****), while transitions within excited triplets (modes* ***B*** *and* ***B'****) are shown as dashed green lines. The field orientation is the same as in Fig. 5.11.*

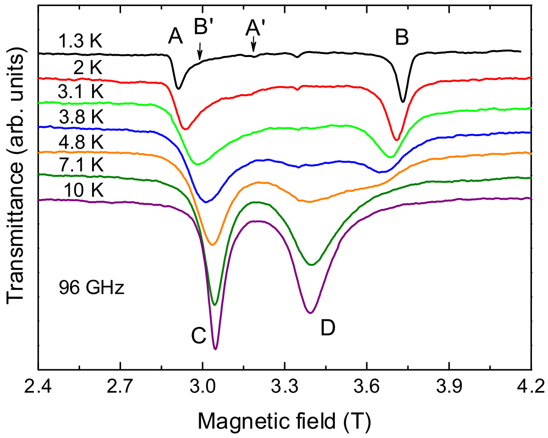

Figure 5.13.: *ESR spectra measured at 96 GHz with the same field orientation as in Fig. 5.11 and at temperatures as indicated. Calculated positions of the modes* $\mathbf{A}'$ *and* $\mathbf{B}'$ *are shown.*

low-temperature ESR excitation spectrum in BPCB, using the anisotropy parameters as obtained from the analysis of the angular dependence (Fig. 5.8), are shown in Fig. 5.11 by solid and dotted lines. A schematic energy-field diagram of the ESR transitions in BPCB (for one ladder) is shown in Fig. 5.12. Please note, that due to their weak intensity, the modes $\mathbf{A}'$ and $\mathbf{B}'$ (dotted lines in Fig. 5.11) were not observed in these high-frequency ESR experiments. For frequencies above 150 GHz the calculated intensity of the transitions shown by the dotted lines is less than 0.5% of that for the modes **A** and **B**.

The temperature evolution of the ESR absorptions measured at 96 GHz is shown in Fig. 5.13. With increasing temperature, the low-temperature modes **A** and **B** vanish above $\sim$ 7 K, while two new modes, **C** and **D**, emerge above $\sim$ 3 K. This unusual temperature dependence of the ESR spectra is consistent with previous observations [133] on BPCB crystals from the same batch as used by Watson *et al.* [108]. The temperature dependences of the integrated ESR intensities of the modes **A**, **B**, **C**, and **D** showed that the observed excitations correspond to transitions between excited states (Fig. 5.12). It is worth to mention that the effect of the observed anisotropy (resulting in the gaped nature of the modes **A** and **B**) is particularly distinct at low temperatures (when thermal fluctuations are suppressed) and disappears with increasing temperature. The frequency-field dependence of the high-temperature modes **C** and **D** as measured at $T = 10$ K (Fig. 5.14) can be described by the formula $h\nu = g\mu_B B$ with $g = 2.28$ and $g = 2.04$, respectively, where *no* anisotropy is included. In accordance with the exchange-narrowing theory [134],

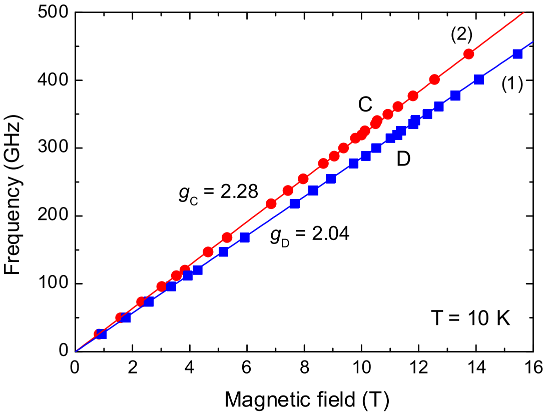

Figure 5.14.: *Frequency-field diagram of the ESR excitations measured at* $T = 10$ *K with the same field orientation as in Fig. 5.11. Lines denote results of calculations using the formula* $h\nu = g\mu_B B$.

for thermally activated spins the hopping probability (or exchange frequency) is temperature dependent. At a fixed frequency at low temperatures, the concentration of excited triplets is small, while the hopping probability is high, resulting in a fast-exchange regime and well-resolved narrow ESR absorptions (the modes **A** and **B**). At higher temperatures, the concentration of triplets increases, the probability of hopping along the ladder legs becomes smaller, and the low-temperature ESR resonances merge in a single line (slow-exchange regime). The crossover from the fast- to slow-exchange limit was observed in a number of quantum magnets with spin-singlet ground state, for instance, in $TlCuCl_3$ [135] and $BaCuSi_2O_6$ [136, 137]. More details about the exchange narrowing phenomenon in magnetic resonance can be found in Ref. [138].

What can be the origin of the observed anisotropy in BPCB? Although dipole-dipole interactions can contribute to the anisotropy they are too small to explain the splitting of the modes extracted from our ESR experiments, and suggesting spin-orbit interactions as the main source of the anisotropy. This anisotropy can be caused by the antisymmetric Dzyaloshinskii-Moriya (DM) interaction, symmetric anisotropic (sometimes called Kaplan-Shekhtman-Entin-Wohlman-Aharony [KSEWA]) interaction [139, 140], or by their mixture. In BPCB, the DM interaction is forbidden on the rungs of the ladder by symmetry, but it is allowed along the ladder legs. The absence of ESR transitions from the singlet ground state to the excited triplet state at $k = \pi$ suggests that the DM vector alternation along the legs is not present. The effect of the antisymmetric DM and symmetric KSEWA interactions in spin ladders has been studied theoretically [116]. It was shown that in spin systems with SU(2) symmetry the DM term breaks SU(2) symmetry, opening a gap in the excitation spectrum above B_c. On the other hand, the effect of KSEWA interactions is to recover the SU(2) symmetry, leaving the excitation spectrum incommensurate but gapless. No sign of a gap in the excitation spectrum has been detected by NMR [109] in the vicinity of B_c and B_{sat} down to 40 mK. The presence of KSEWA interactions (or the combined effect of the DM and KSEWA interactions) would explain the experimental results. Our ESR observations call for further development of the theory [116] towards the strong-coupling limit, which is relevant for BPCB.

The effects of the anisotropy undeniably need to be taken into account when describing the phase diagram of BPCB. For example, B_c and B_{sat} are found to be more sensitive to the direction of the applied magnetic field than expected from the anisotropy of the g-tensor only, possibly explaining variations in the values of the critical fields reported in the literature [108–112, 123–125]. The observation of the relatively large biaxial anisotropy (which breaks the U(1) rotational symmetry) can be of particular importance when applying the magnon BEC formalism for the description of the field-induced antiferromagnetically ordered phase in BPCB at lower temperatures [109, 110].

5.4. Summary

This work provides a direct evidence for a pronounced (5% of the dominant exchange interaction) biaxial anisotropy in BPCB, that is in contrast to a fully isotropic spin-ladder model employed for this system previously. We argued that the effects of the anisotropy need to be taken into account when describing critical properties of BPCB. Understanding the role of anisotropy and its experimental consequences in spin ladders itself is of fundamental interest, having a broader impact, and offering $(C_5H_{12}N)_2CuBr_4$ as a well suited model system for investigating the anisotropy effects in spin ladders.

6. Dimensional crossover in the quasi-2D spin-$\frac{1}{2}$ compound $[\mathrm{Cu(pyz)_2(HF_2)}]\mathrm{PF_6}$

6.1. Properties of quasi-2D spin systems

The discovery of high-temperature superconductors in the two-dimensional copper-oxide compounds gave rise to a strong interest in the properties of two-dimensional (2D) spin-$\frac{1}{2}$ Heisenberg antiferromagnets. They have a layered crystal structure where magnetic ions form parallel planes and interact strongly within the plane. Such spin systems can be described by the 2D spin Heisenberg antiferromagnetic model. In the case of an ideal 2D Heisenberg magnet quantum fluctuations prohibit a long-range magnetic order (LO) at any non-zero temperature [141]. However, due to a finite interlayer coupling J', real quasi-2D spin systems undergo a transition to a 3D-ordered state when $T \neq 0$. In such a case the system can be described using the Hamiltonian

$$H = J \sum_{nn} \left[S_i^x S_j^x + S_i^y S_j^y + (1-\lambda) S_i^z S_j^z \right] + J' \sum_{i,j'} \mathbf{S}_i \mathbf{S}_{j'} - g\mu_B \mathbf{B} \sum_j \mathbf{S}_i \,. \tag{6.1}$$

Here, J corresponds to the in-plane antiferromagnetic exchange coupling and J' is the coupling constant between spins in adjacent layers, and λ is the exchange-anisotropy parameter and B is the applied magnetic field. This quasi-2D HAF Hamiltonian can be transformed to isotropic form by setting $J' = 0$, $\lambda = 0$, and $B = 0$. To date, theoretical calculations fail to describe the magnetic properties of the Hamiltonian (6.1) taking into account arbitrary values of J', B, and λ simultaneously, however, are successful if one considers the influence of J', B, and λ separately [142–144].

As mentioned, the interlayer interaction J' (which is always present in real materials) can significantly modify the ground-state properties of quasi-2D systems, inducing, for instance, a phase transition to a three-dimensional (3D) long-range magnetically ordered state at the temperature T_N. In accordance with the theory [66] for the isotropic case ($\lambda = 0$) in the absence of a magnetic field ($B = 0$), the interlayer coupling J' can be estimated using simple empirical formula:

$$\frac{J'}{J} = \exp\left(d - \frac{4\pi\rho_s}{T_N}\right) , \tag{6.2}$$

where ρ_s is the spin stiffness ($\rho_s = 0.183J$ for the 2D HAF system [145]) and $d = 2.43$ for $S = \frac{1}{2}$.

Depending on the sign of the anisotropy constant λ, two main cases can be distinguished: easy-plane anisotropy ($0 < \lambda \leq 1$) and easy-axis anisotropy ($\lambda < 0$) with its extreme case $\lambda \ll 0$ (Ising anisotropy) [146]. The theory of Kosterlitz, Thouless, and Berezinskii (BKT) [147–150] predicts a vortex-like spin configuration and a topological phase transition to take place in the classical ($S \to \infty$) XY model ($\lambda = 1$). In accordance with the theory, the high-temperature disordered phase can be described as a gas of non-linear topological vortex excitations, which at $T < T_{BKT}$ are bound in vortex-antivortex pairs coupled to each other via a short-range-order interaction [151]. The region of critical fluctuations in the vicinity of T_{BKT} is predicted to be much broader ($\Delta T/T_{BKT} \approx 0.6$) than that for the classical XY model ($\Delta T/T_N \approx 0.1$) [152].

The qualitative behavior of the BKT-type transition is preserved in the 2D quantum HAF model with easy-plane anisotropy, with only quantitative modifications of the critical parameters due to the quantum fluctuations. A good probe of the BKT phase transition is the correlation function, because the divergence of the correlation length ξ at the critical temperature T_c constitutes the clearest evidence of a phase transition and the corresponding critical exponent for classifying the transition. Quantum Monte Carlo simulations for large lattices [153] showed, that the critical behavior in the quantum case is of BKT type since the correlation length and the susceptibility diverge exactly as for the BKT theory,

$$\xi(T) \propto \exp\left(\frac{b_o}{\sqrt{(T/T_{BKT} - 1)}}\right) . \tag{6.3}$$

Quantum fluctuations are capable to reduce the transition point from $T_{BKT} = 0.898J/k_B$ in the large-spin case down to $T_{BKT} = 0.35J/k_B$ in the quantum $S = \frac{1}{2}$ case, although not strong enough to push it down to zero. These fluctuations also reduces the constant b_o in the Eq. (6.3) from

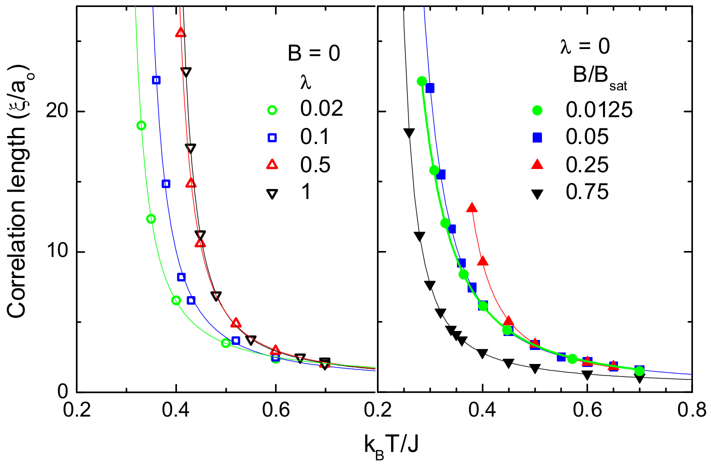

Figure 6.1.: *Correlation length ξ as function of the normalized temperature k_BT/J for different anisotropies (left) [143] and magnetic fields (right) [154].*

$\pi/2$ to 1.18 [153]. As consequence, it extends the critical region to $\Delta T/T_{BKT} \approx 0.8$, defined by the correlation length $\xi(T) \geq 3a$. The specific heat exhibits a steep rise in the vicinity of T_{BKT} and a finite asymmetric peak around $T \sim 0.45J$.

Furthermore, Monte Carlo simulations [143] indicate, that the critical regime for 2D HAF systems is unstable toward any additional perturbation. As result, 2D HAF systems can be driven to the BKT-type transition by the presence of an in-plane exchange anisotropy λ. The topological ordering appears to be at T_c, rising from 0 to T_{BKT} with increasing anisotropy, as it follows from the divergence of the correlation length $\xi(T)$ well described by Eq. (6.3), as shown in Fig. 6.1. The phase diagram is drastically affected even by a small anisotropy (Fig. 6.2), since the critical temperature has a nontrivial dependence with respect to the anisotropy energy scale: $T_c \sim 1/\ln(1/\lambda)$ [143].

The effective easy-plane anisotropy can also be induced by an external magnetic field which causes a reduction of the full rotational symmetry of the isotropic model $O(3)$ to a $O(2)$ symmetry in the xy plane [155, 156]. While an applied magnetic field suppresses fluctuations of the spin z component [157], this does not hold for the x and y components. Therefore, the xy plane acquires an effective field-induced easy-plane anisotropy. For infinitesimally small fields one, hence, expects the spins to orient antiparallel within the xy plane, and progressively cant out of the plane as B is increased. The thermal and quantum fluctuations of the spin z components become smaller with increasing field. For large enough fields the average projection of the spins onto the

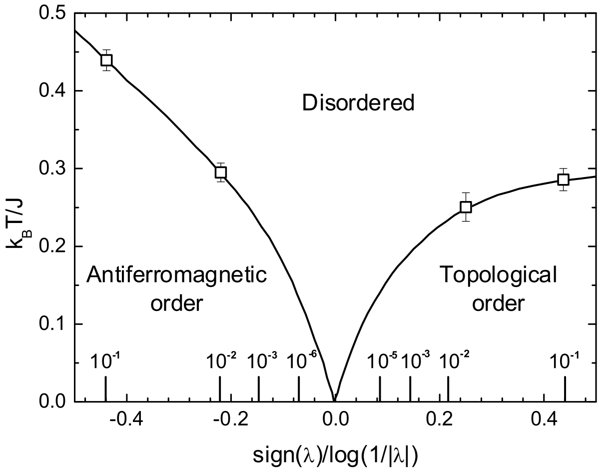

Figure 6.2.: *Phase diagram found by Ding in his Monte Carlo simulation of a 2D HAF systems with small in-plane exchange anisotropy [143].*

xy plane is strongly reduced. The saturation occurs at the critical value B_{sat}, above which the ground state displays a uniform ferromagnetic alignment along the field direction. Assuming that the saturation field depends only on the exchange strength, the mean-field equation for B_{sat} of a spin-$\frac{1}{2}$ system is given by

$$B_{sat} = \frac{ZJ}{g\mu_B}, \tag{6.4}$$

where Z is the number of nearest neighbors [158].

Recently, numerical studies revealed that an isotropic 2D HAF system in an applied external magnetic field shares common features (for instance, a critical behavior) with that of an easy-plane system (Fig. 6.1), suggesting the occurrence of a topological-order phase transition as long as $B < B_{sat}$ [156,159]. In this case, the magnetic field can be considered as a tuning parameter. The phase diagram (Fig. 6.3) obtained from large-scale Monte Carlo simulations shows a nonmonotonic field dependence, which is regarded as a signature of a field-induced easy-plane anisotropy (or XY behavior).

However, due to transitions into 3D ordered state, an unambiguous observation of the topological order anticipated for ideal 2D systems with XY-type anisotropy failed in real materials. Particularly, it was shown, that for any finite interlayer coupling J' the 3D long-range order occurs *always* at higher temperatures, than topological ordering induced by a magnetic field, $T_N > T_c$ [156]. As consequence, the XY critical behavior is masked by the onset of 3D long-range order. However, since the XY critical region is broa-

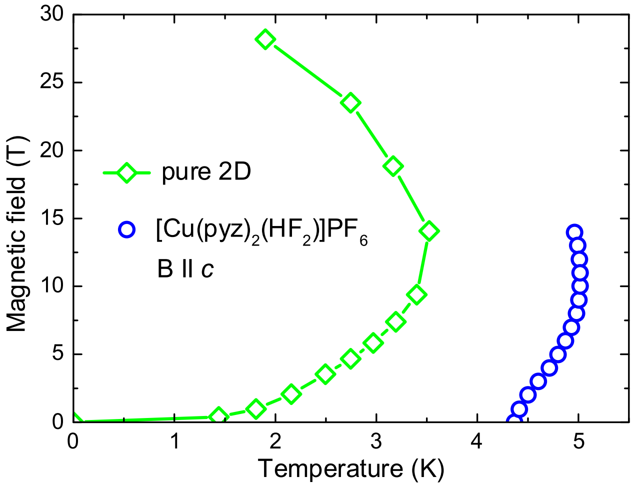

Figure 6.3.: *Magnetic phase diagram for an ideal and quasi-2D HAF system. The green diamonds represent the data for the ideal case J' [156] and blue spheres show the data for $[Cu(C_4H_4N_2)_2(HF_2)]PF_6$ obtained from specific-heat measurements (Fig. 6.6) [160]. Lines are guides to the eye.*

der than for 3D long-range order, XY spin correlations would exhibit itself in magnetic properties in the vicinity of T_N.

To get a better understanding of the properties of 2D antiferromagnets, it is necessary to find materials with suitable exchange constants J and J'. Copper pyrazine compounds are known to form linear chains [161–163] and layered structures [164, 165] with the pyrazine molecule ($C_4H_4N_2$) linking Cu atoms in large coordination polymers. Recently, the syntheses of a family of crystal structures with the general chemical formula $[Cu(pyz)_2]A_2$ (where A represents a noncoordinating or poorly coordinating anion) was reported [166, 167]. These materials are good examples of quasi-2D Heisenberg antiferromagnets with $J'/J \sim 10^{-3} - 10^{-4}$ and moderate exchange interaction, J, small enough to reach full polarization with accessible fields ($B_{sat} < 50$ T) [106, 166, 168]. It is worth to mention, that a non-monotonic field dependence of the ordering temperature was observed in the quasi-2D square-lattice Heisenberg antiferromagnet $[Cu(C_4H_4N_2)_2(HF_2)]BF_4$ [156, 169]. In this work, magnetic properties and the low-energy excitation spectrum of $[Cu(C_4H_4N_2)_2(HF_2)]PF_6$, belonging to the same family of compounds, is reported [160].

6.2. Magnetic properties of $[Cu(pyz)_2(HF_2)]PF_6$

$[Cu(C_4H_4N_2)_2(HF_2)]PF_6$ (hereafter $[Cu(pyz)_2(HF_2)]PF_6$) crystallizes in a tetragonal lattice (space group $P4/nmm$; $Z = 1$) with spin-$\frac{1}{2}$ Cu^{2+} ions arranged in a planar square-lattice structure (Fig. 6.4). Cu^{2+} ions are bridged by pyrazine groups in the *ab* plane and the planes are connected by HF_2 groups along the *c* axis. The planes of the pyrazine groups are nearly orthogonal to the Cu^{2+} planes. The non-coordinating PF_6 groups pack in between the planes, in the center of almost cubic units [166]. In the experiments described below single crystals with a typical size of $4 \times 3 \times 1$ mm^3 were used, synthesized by aqueous reaction of stoichiometric amounts of ammonium bifluoride, pyrazine, and copper(II) hexafluorophosphate hydrate (using the same procedure as reported in Ref. [169, 170])

Pulsed-field magnetization of $[Cu(pyz)_2(HF_2)]PF_6$ was measured by Y. Skourski, HLD. The data obtained at 1.5 K in magnetic fields up to 50 T applied parallel and perpendicular to the *c* axis are shown in Fig. 6.5 [160]. The calculated magnetization for an spin-$\frac{1}{2}$ 2D square-lattice Heisenberg AF is shown by the solid line.

The fully spin-polarized state was observed at $B^{ab}_{sat} = 37.5$ T and $B^{c}_{sat} = 33.8$ T for $B \parallel ab$ and $B \parallel c$, respectively. A similar magnetization dependence was found for both magnetic-field orientations. Our analysis revealed that the magnetization anisotropy is solely determined by the *g*-factor

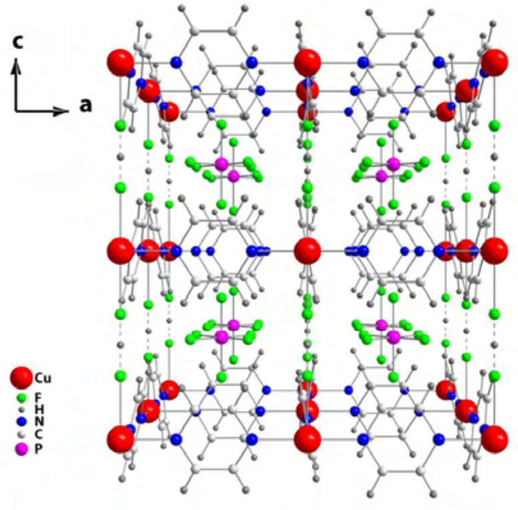

Figure 6.4.: *Schematic view of the crystal structure of* $[Cu(pyz)_2(HF_2)]PF_6$ *along the b axis.*

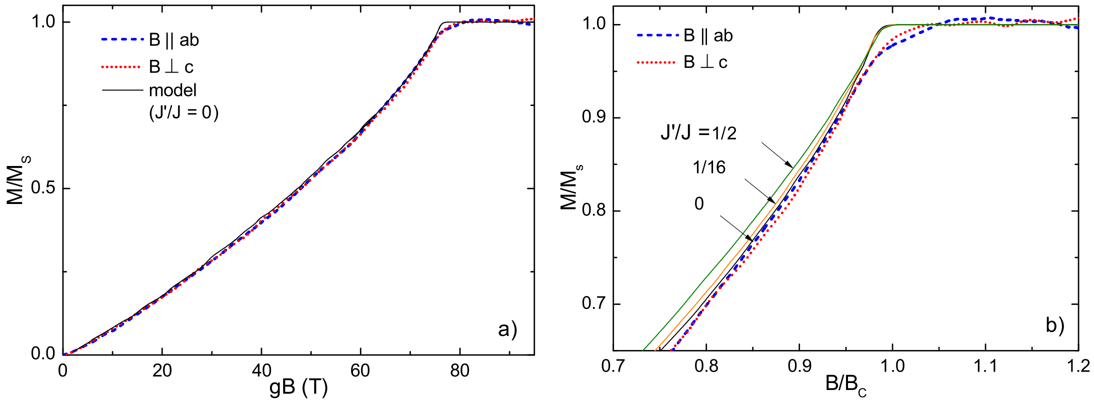

Figure 6.5.: *a) High-field magnetization of $[\mathrm{Cu(pyz)_2(HF_2)}]\mathrm{PF_6}$ (dashed and dotted lines correspond to $B\perp c$ and $B \parallel c$, respectively). The experimental data are shown as a function of gB, where B is the applied magnetic field and the g-factors are $g_c = 2.28$ and $g_{ab} = 2.05$, as determined by X-band ESR measurements. b) The same data in an expanded scale close to saturation with additional model calculations assuming a finite interplane interaction.*

anisotropy. The numerically calculated magnetization for a spin-$\frac{1}{2}$ 2D HAF on a square-lattice with an intraplane exchange interaction $J/k_B = 12.8$ K [166, 171] is in very good agreement with the experimental data (Fig. 6.5). In order to estimate the ratio J'/J, calculations using this model with different interplane interactions have been made (Fig. 6.5b) [160]. By comparison with the measured data it can be concluded that J'/J must be less than 1/16.

The specific-heat measurements were performed using a continuous relaxation-time technique [172, 173] by R. Beyer, HLD. The high-resolution specific-heat measurements allowed to clearly resolve the 3D AF ordering temperature in zero and applied magnetic fields up to 14 T (Fig. 6.6). Using the local maximum of the specific-heat anomaly, the $B-T$ phase diagram has been extracted. Figure 6.3 shows the result together with data calculated for an ideal 2D Heisenberg AF system ($J' = 0$) with $J/k_B = 12.8$ K [156]. For small magnetic fields, the critical temperature T_N increases due to the induced effective easy-plane anisotropy. For sufficiently strong magnetic fields, T_N decreases, since the spin-canting effect prevails, and vanishes eventually at the saturation field, when the fully spin-polarized state is reached. The observed non-monotonic $B-T$ behavior of $[\mathrm{Cu(pyz)_2(HF_2)}]\mathrm{PF_6}$ can be nicely explained by modifying above model with a weak interplane interaction. As a threshold for the observation of a λ-like anomaly in the specific heat, $J'/J < 0.015$ has been given in Ref. [142]. This ratio is very close to that, $J'/J = 0.01$, esti-

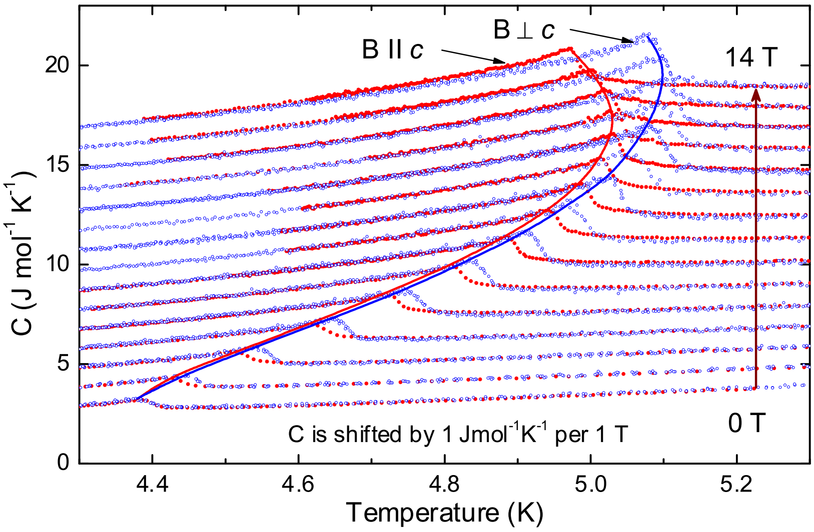

Figure 6.6.: *Temperature dependence of the specific heat of $[Cu(pyz)_2(HF_2)]PF_6$ for $B \parallel ab$ (blue symbols) and $B \parallel c$ (red symbols).*

mated from the zero-field μSR measurements on powdered samples [166]. In the range $0.001 \leq J'/J \leq 1$ the interplane coupling can be estimated employing Eq. (6.2) [66]. Using the exchange coupling, obtained from the high-field magnetization data, and $T_N = 4.38$ K the ratio $J'/J = 0.014$ was determined, which is in excellent agreement with the previous estimate.

6.3. ESR experiments

Low-frequency ESR data on $[Cu(pyz)_2(HF_2)]PF_6$ were reported previously [174]. In this work here, the frequency range of ESR measurements was extended up to 260 GHz. At room temperature, a single ESR line was observed for all field orientations with a typical sinusoidal angular dependence of the g-factor expected for a Cu^{2+} ion in an octahedral surrounding with an axial symmetry due to the Jahn-Teller effect. The results confirm that the main exchange paths between the magnetic ions are formed in the ab planes by $d_{x^2-y^2}$ orbitals [131], which directly overlap with orbitals of pyrazine ligands, creating a quasi-2D network of exchange coupled Cu^{2+} ions.

The temperature evolution of the ESR spectra in $[Cu(pyz)_2(HF_2)]PF_6$ measured at 90 GHz for $B \parallel c$ is shown in Fig. 6.7a. The temperature dependence of the resonance field, the linewidth, and the integrated intensity of the ESR lines in fields applied parallel and perpendicular to the ab plane are shown in

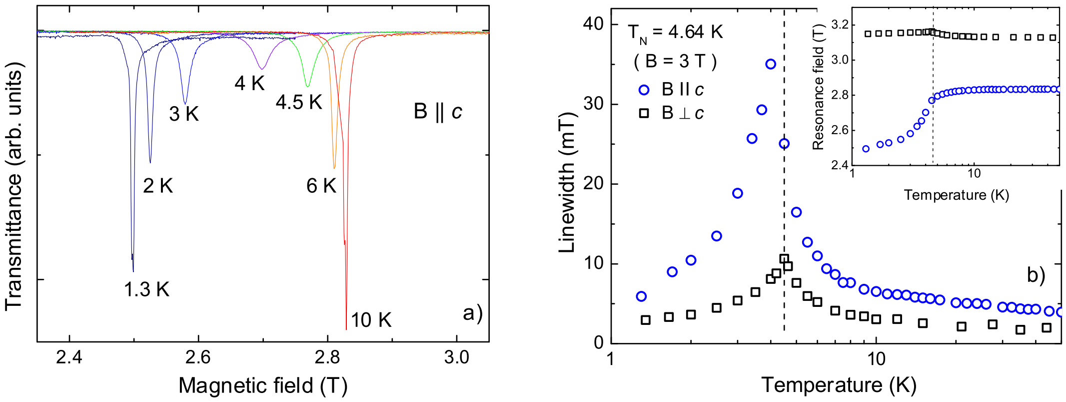

Figure 6.7.: *a) ESR signal (transmission) measured at 90 GHz in the temperature range of 1.3 - 10 K for $B \| c$. b) Temperature dependence of the linewidth obtained from the ESR data measured at 90 GHz for a magnetic field aligned parallel (squares) and perpendicular (circles) to the ab plane. The transition temperature, $T_N = 4.64$ K, as obtained from specific-heat measurements at 3 T for $B \perp c$ is indicated by the dotted vertical line. The inset shows the temperature dependence of the resonance field.*

Figs. 6.7b and 6.8. It is evident that in the vicinity of the ordering temperature ($T_N \approx 4.6$ K at 3 T), a region of enhanced short-range spin correlations is entered and both the resonance field and the linewidth change dramatically. It is important to mention that the integrated ESR intensity is proportional to the dynamic spin susceptibility.

In Fig. 6.8, the temperature dependence of M/B (measured using a SQUID magnetometer with applied magnetic field $B = 3$ T), the integrated ESR intensity, and the magnetic susceptibility calculated for a 2D Heisenberg AF system [171, 175] are presented. The results of the calculations are in good agreement with the experimental data above T_N for $J/k_B = 12.8$ K, proving the important role of 2D spin correlations in $[\mathrm{Cu}(\mathrm{C_4H_4N_2})_2(\mathrm{HF_2})]\mathrm{PF_6}$.

Well above the critical temperature ($T = 15$ K), only one resonance mode for each orientation was observed, $B \parallel c$ and $B \perp c$. The frequency-field dependence of the these modes corresponds to transitions between the energy levels of the $S = \frac{1}{2}$, Cu^{2+} ions and can be described by $h\nu = g\mu_B B$ with $g_c = 2.28$ and $g_{ab} = 2.05$. The ESR excitation spectrum changes dramatically below T_N. Two modes, ω_1 and ω_2, are observed in $[\mathrm{Cu(pyz)_2(HF_2)}]\mathrm{PF_6}$, when the magnetic field is applied in the *ab* plane (Fig. 6.9).

The frequency-field diagram of the magnetic excitations obtained at 1.3 K is shown in Fig. 6.10. For $B \parallel c$, a nonlinear dependence of the mode ω_4 was observed. Most importantly, in the ESR excitation spectrum the AF

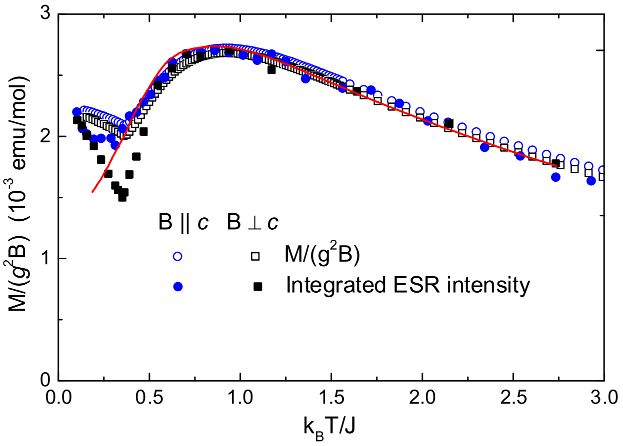

Figure 6.8.: *Temperature dependence of* M/B *measured at* $B = 3$ *T (open symbols) and the integrated intensity obtained from ESR data measured at* $\nu = 90$ *GHz (closed symbols). The data are presented together with the calculated results (solid line) for a 2D square-lattice Heisenberg AF system with* $J/k_B = 12.8$ *K [171, 175].*

resonance gap was determined directly, $\Delta = 43$ GHz (≈ 2 K) at $B = 0$. Such a frequency-field diagram is a textbook example for magnetic excitations in a system with collinear 3D AF long-range order and easy-plane anisotropy [176]. The frequency-field dependence of the antiferromagnetic resonance modes can be calculated using the mean-field approximation [177]:

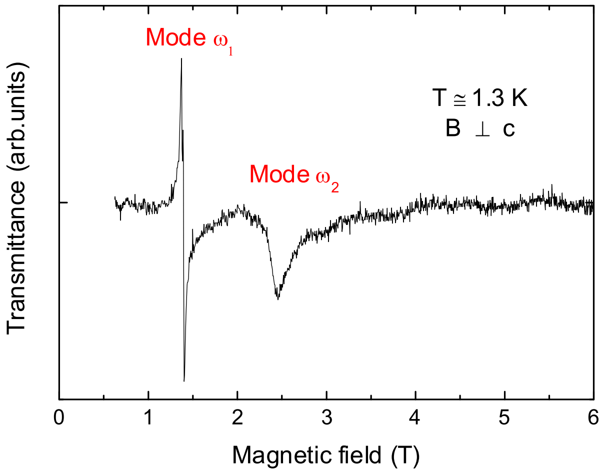

Figure 6.9.: *The ESR transmission spectrum of* $[Cu(pyz)_2(HF_2)]PF_6$*, taken at a frequency of 39.486 GHz and* $T \approx 1.3$ *K.*

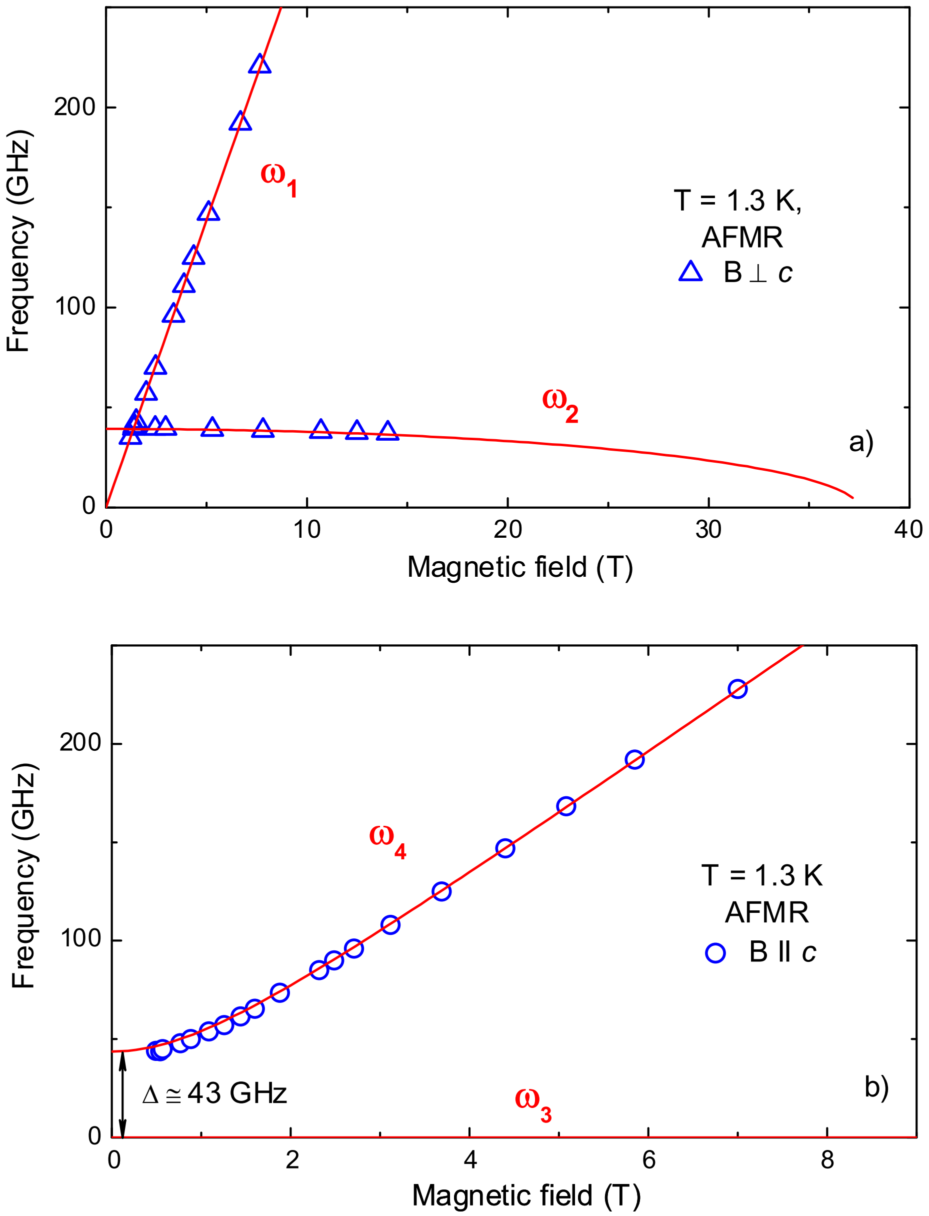

Figure 6.10.: *Frequency-field diagram of the ESR excitations measured at* $T = 1.3$ K *for a magnetic field aligned (a) parallel and (b) perpendicular to the ab plane. The signals* ω_1, ω_2, ω_3, *and* ω_4 *correspond to AF resonance modes of a 3D ordered AF system with easy-plane anisotropy calculated as described in the text.*

$$\omega_1/\gamma = B, \tag{6.5}$$
$$\omega_2/\gamma = \sqrt{2B_A B_E - (B_A/2B_E)\,B^2}, \tag{6.6}$$

for magnetic fields applied parallel to the easy plane and

$$\omega_3/\gamma = 0, \tag{6.7}$$
$$\omega_4/\gamma = \sqrt{2B_A B_E + (1 - B_A/2B_E)\,B^2}, \tag{6.8}$$

for magnetic fields applied perpendicular to the easy plane, where $\gamma = g\mu_B/\hbar$ is the gyromagnetic ratio, and B_E and B_A are the exchange and anisotropy field, respectively.

These results clearly show that below T_N the ab plane is the easy plane, along which the magnetic moments are aligned at $B = 0$. The frequency-field diagram was analyzed using the Eqs. (6.5) – (6.8). The best fit was obtained for $B_E = 18.72$ T and $B_A = 0.05$ T. The exchange field B_E is related to the exchange coupling by the simple relation $B_E = 4SJ/\hbar\gamma$ and yields $J/k_B = 12.9$ K, which is in perfect agreement with the value of the intraplane exchange coupling obtained from magnetization and specific-heat measurements. Noticeably, using ESR data, the anisotropy constant ($\sim$ 0.3% of the exchange interaction) can be estimated, revealing the validity of the isotropic quasi-2D spin-$\frac{1}{2}$ Heisenberg model applied to $[Cu(pyz)_2(HF_2)]PF_6$.

6.4. Summary

Our specific-heat, high-field magnetization, and ESR studies revealed the important role of 2D spin correlations in the spin-$\frac{1}{2}$ quasi-2D Heisenberg antiferromagnet $[Cu(C_4H_4N_2)_2(HF_2)]PF_6$. The antiferromagnetic resonance was studied in magnetic fields up to 16 T, revealing the presence of a 3D collinear AF long-range ordered state with an energy gap of $\Delta = 43$ GHz. The direct observation of the energy gap allowed an accurate estimation of the effective spin-Hamiltonian parameters, g-factors ($g_c = 2.28$ and $g_a b = 2.05$), $J/k_B = 12.8$ K, and $A/J \sim 0.3\%$. The presence of a field-induced easy-plane anisotropy has unambiguously been identified by the observation of a peculiar non-monotonic field dependence of the ordering temperature.

7. Conclusions

During this thesis work, a pulsed-field tunable-frequency ESR spectrometer has been developed. This device allows performing high-field (up to 63 T and beyond) high-resolution ESR experiments in the frequency range 50 - 450 GHz (employing VDI radiation sources) and 1.2 - 75 THz (employing free-electron lasers). The spectrometer was used complementary to a 16 T ESR spectrometer, operated in the frequency range of 24 GHz - 1.3 THz. The facilities were successfully used for the investigation of magnetic excitation spectra in a number of low-dimensional spin systems. These include the following materials.

1. The spin-$\frac{1}{2}$ chain compound $(C_6H_9N_2)CuCl_3$. Based on the obtained ESR spectra the striking incompatibility with a simple uniform $S = \frac{1}{2}$ Heisenberg chain model has been revealed. The observed excitation spectrum was explained in terms of the recently developed theory for spin-$\frac{1}{2}$ chains, revealing the important role of next-nearest-neighbor interactions in this compound.

2. Copper pyrimidine dinitrate $[PM{\cdot}Cu(NO_3)_2(H_2O)_2]_n$, a spin-$\frac{1}{2}$ antiferromagnetic chain material with alternating g-tensor and the Dzyaloshinskii-Moriya interaction. The excitation spectrum was probed in magnetic fields up to 63 T. Pronounced changes in the frequency-field dependence of the magnetic excitations have been observed in the vicinity of the saturation field, $B \sim B_{sat} = 48.5$ T, clearly indicating a transition from the soliton-breather to a spin-polarized state with magnons as elementary excitations. The experimental data were compared with results of density matrix renormalization group calculations. Excellent agreement was found.

3. The spin-ladder material $(C_5H_{12}N)_2CuBr_4$. The ESR studies provided a direct evidence for a pronounced anisotropy in this compound, that is in contrast to the fully isotropic spin-ladder model employed for this material previously. It is argued that this effect is caused by spin-orbit

coupling, which appears to be important for describing the magnetic phase diagram (including magnon condensation and the transition into the Luttinger-Liquid phase) of this compound. The detailed characterization of the anisotropy effects complements the determination of the full spin Hamiltonian of $(C_5H_{12}N)_2CuBr_4$.

4. The quasi-two dimensional spin-$\frac{1}{2}$ compound $[Cu(C_4H_4N_2)_2(HF_2)]PF_6$. The presence of a field-induced XY behavior has unambiguously been identified by the observation of a peculiar non-monotonic field dependence of the ordering temperature. The frequency-field diagram of magnetic excitations in the AFM-ordered state has been studied. The data were analyzed in the frame of a mean-field theory, confirming a collinear magnetic structure of this system with an easy-plane anisotropy. Parameters of the effective spin-Hamiltonian (exchange interaction, anisotropy, and g-factor) were obtained and employed for describing the high-field properties of this material. It is argued that despite the onset of 3D long-range magnetic ordering the magnetic properties of this material (including the high-magnetic-field magnetization studied in fields up to 48 T) are strongly affected by two-dimensional spin correlations.

Bibliography

[1] S. Hill, J.A. Perenboom, N.S. Dalal, T. Hathaway, T. Stalcup, and J.S. Brooks, Phys. Rev. Lett. **80**, 2453 (1998).

[2] K. Katsumata, J. Phys.: Condens. Matt. **12**, R589 (2000).

[3] T. Asano, H. Nojiri, Y. Inagaki, J.P. Boucher, T. Sakon, Y. Ajiro, and M. Motokawa, Phys. Rev. Lett. **84**, 5880 (2000).

[4] M. Yoshida, K. Shiraki, S. Okubo, H. Ohta, T. Ito, H. Takagi, M. Kaburagi, and Y. Ajiro, Phys. Rev. Lett. **95**, 117202 (2005).

[5] S.A. Zvyagin, A.K. Kolezhuk, J. Krzystek, and R. Feyerherm, Phys. Rev. Lett. **95**, 017207 (2005).

[6] J. Krzystek, S.A. Zvyagin, A. Ozarowski, S. Trofimenko, and J. Telser, J. Magn. Res. **178**, 174 (2006).

[7] S.A. Zvyagin, J. Wosnitza, C.D. Batista, M. Tsukamoto, N. Kawashima, J. Krzystek, V.S. Zapf, M. Jaime, N.F. Oliveira, and J.A. Paduan-Filho, Phys. Rev. Lett. **98**, 047205 (2007).

[8] G. Toraldo di Francia, Nuovo Cimento **16**, 61 (1960).

[9] P.M. van den Berg and T.H. Tan, J. Opt. Soc. Am. **64**, 325 (1974).

[10] T.A. Vaughan, R.J. Nicholas, C.J.G.M. Langerak, B.N. Murdin, C.R. Pidgeon, N.J. Mason, and P.J. Walker, Phys. Rev. B **53**, 16481 (1996).

[11] L. Van Bockstal, L. Li, C.J.G.M. Langerak, M.J. van de Pol, A. De Keyser, A.F.G. van der Meer, A. Ardavan, J. Singleton, R.J. Nicholas, F. Herlach, R. Bogaerts, H.U. Müller, and M. von Ortenberg, Physica B **246-247**, 208 (1998).

[12] C.J.G.M. Langerak, L. Li, L. Van Bockstal, A. Ardavan, M.J. van de Pol, A.F.G. van der Meer, F. Herlach, H.U. Müller, R.J. Nicholas, and J. Singleton, Physica B **246 - 247**, 400 (1998).

[13] C.J.G.M. Langerak, J. Singleton, L. Li, L. Van Bockstal, A. Ardavan, M.J. van der Pol, A.F.G. van der Meer, F. Herlach, N. Mason, R.J. Nicholas, and P.J. Walker, Physica B **256**, 339 (1998).

[14] S.K. Singh, B.D. McCombe, J. Kono, S.J. Allen, J.I. Lo, W.C. Mitchel, and C.E. Stutz, Phys. Rev. B **58**, 7286 (1998).

[15] M. Helm, T. Fromherz, B.N. Murdin, C.R. Pidgeon, K.K. Geerinck, N.J. Hovenyer, and W.Th. Wenckebach, Appl. Phys. Lett. **63**, 3315 (1993).

[16] P. Michel, F.G. Gabriel, E. Grosse, P. Evtushenko, T. Dekorsy, M. Krenz, M. Helm, U. Lehnert, W. Seidel, R. Wünsch, D. Wohlparth, and A. Wolf, Proceedings of the 26th International Free Electron Laser Conference, Trieste, Italy, 29 August - 3 September 2004, Comitato Conferenze Elettra, Trieste, Italy, 8 (2004).

[17] U. Lehnert, P. Michel, W. Seidel, G. Staats, J. Teichert, and R. Wünsch, Proceedings of the 29th International Free Electron Laser Conference, Novosibirsk, Russia, 26-31 August 2007, Joint Accelerator Conference Website (JACoW), 97 (2007).

[18] M. Freitag, R. Schlenk, W. Seidel, U. Willkommen, D. Wohlfarth, R. Wünsch, and B. Wustmann, Proceedings of FEL, Bessy, Berlin, Germany, 345 (2006).

[19] J.S. Lee, M. Gensch, K. Hinrichs, W. Seidel, and H. Schade, Infrared Physics & Technology **51**, 537 (2008).

[20] F. Gabriel, P. Gippner, E. Grosse, D. Janssen, P. Michel, H. Prade, A. Schamlott, W. Seidel, A. Wolf, and R. Wünsch, Nucl. Instr. & Meth. in Phys. Res. B **161**, 1143 (2000).

[21] W. Seidel, E. Grosse, M. Justus, K.W. Leege, D. Proehl, R. Schlenk, A. Winter, D. Wohlfarth, and R. Wünsch, Proceedings of the 29th International Free Electron Laser Conference, Novosibirsk, Russia, 26-31 August 2007, Joint Accelerator Conference Website (JACoW), 171 (2007).

[22] W. Seidel, S. Friebel, R. Jainsch, M. Justus, K.W. Leege, D. Pröhl, D. Stehr, H. Weigelt, S. Winnerl, and D. Wohlfarth, Proceedings of the 28th International Free Electron Laser Conference, Berlin, Germany, 27 August - 1 September 2006, Joint Accelerator Conference Website (JACoW), 341 (2006).

[23] T. Dekorsy, V.A. Yakovlev, W. Seidel, M. Helm, and F. Keilmann, Phys. Rev. Lett. **90**, 055508 (2003).

[24] H. Schneider, O. Drachenko, S. Winnerl, M. Helm, and M. Walther, Appl. Phys. Lett. **89**, 133508 (2006).

[25] H. Schneider, O. Drachenko, S. Winnerl, M. Helm, T. Maier, and M. Walther, Infrared Physics & Technology **50**, 95 (2007).

[26] S. Schneider, J. Seidel, S. Grafström, L.M. Eng, S. Winnerl, D. Stehr, and M. Helm, Appl. Phys. Lett. **90**, 143101 (2007).

[27] S.C. Kehr, M. Cebula, O. Mieth, T. Hartling, W. Seidel, S. Grafstrom, L.M. Eng, S. Winnerl, D. Stehr, and M. Helm, Phys. Rev. Lett. **100**, 256403 (2008).

[28] M.F. Kimmitt, Infrared Phys. **32**, 213 (1991).

[29] E.H. Putley, Phys. Stat. Sol. **6**, 571 (1964).

[30] T. Herrmannsdörfer, H. Krug, F. Pobell, S. Zherlitsyn, J. Freudenberger, K.H. Müller, and L. Schutz, J. Low Temp. Phys. **133**, 41 (2003).

[31] S. Zherlitsyn, T. Herrmannsdörfer, Yu. Skourski, A. Sytcheva, and J. Wosnitza, J. Low Temp. Phys. **146**, 719 (2007).

[32] S. Zherlitsyn, A.D. Bianchi, T. Herrmannsdörfer, F. Pobell, Yu. Skourski, A. Sytcheva, S. Zvyagin, and J. Wosnitza, IEEE Trans. Appl. Supercond. **16**, 1660 (2006).

[33] J. Wosnitza, G. Goll, M. Bartkowiak, B. Bergk, A.D. Bianchi, H.v. Löhneysen, T. Yoshino, and T. Takabatake, Physica B: Cond. Matt. **403**, 1219 (2008).

[34] Wieland-K88 is a high-strength copper alloy with the chemical composition: Cr - 0.5%, Ag - 0.1%, Fe - 0.08%, Ti - 0.06%, Si - 0.03%, Cu balance (product of „Wieland-Werke AG").

[35] S.A. Zvyagin, M. Ozerov, E. Čižmár, D. Kamenskyi, S. Zherlitsyn, T. Herrmannsdörfer, J. Wosnitza, R. Wünsch, and W. Seidel, Rev. Scien. Instr. **80**, 073102 (2009).

[36] T.J. Sato, S.H. Lee, T. Katsufuji, M. Masaki, S. Park, J.R.D. Copley, and H. Takagi, Phys. Rev B **68**, 266604 (2007).

[37] H.A. Bethe, Z. Phys. **71**, 205 (1931).

[38] G. Müller, H. Thomas, H. Beck, and J.C. Bonner, Phys. Rev. B **24**, 1429 (1981).

[39] M.B. Stone, D.H. Reich, C. Broholm, K. Lefmann, C. Rischel, C.P. Landee, and M.M. Turnbull, Phys. Rev. Lett. **91**, 037205 (2003).

[40] F.D.M. Haldane, Phys. Rev. Lett. **50**, 1153 (1983).

[41] S. Grossjohann and W. Brenig, Phys. Rev. B **79**, 094409 (2009).

[42] B. Lake, D.A. Tennant, C.D. Frost, and S.E. Nagler, Nature Mater. **4**, 329 (2005).

[43] S. Watanabe, and H. Yokoyama, J. Phys. Soc. Japan **68**, 2073 (1999).

[44] S.R. White and I. Affleck, Phys. Rev. B **54**, 9862 (1996).

[45] B.S. Shastry and B. Sutherland, Phys. Rev. Lett. **47**, 964 (1981).

[46] See, e.g., A.A. Zvyagin *Finite Size Effects in Correlated Electron Models: Exact Results*, Imperial College Press, London (2005) and references therein.

[47] P. Pincus, Solid State Commun. **9**, 1971 (1971); M.C. Cross, and D.S. Fisher, Phys. Rev. B **19**, 402 (1979).

[48] F.D.M. Haldane, Phys. Rev. B **25**, 4925 (1982).

[49] K. Okamoto and K. Nomura, Phys. Lett. A **169**, 433 (1992).

[50] S.L. Drechsler, O. Volkova, A.N. Vasiliev, N. Tristan, J. Richter, M. Schmitt, H. Rosner, J. Màlek, R. Klingeler, A.A. Zvyagin, and B. Büchner, Phys. Rev. Lett. **98**, 077202 (2007).

[51] C.N. Yang and C.P. Yang, Phys. Rev. **150**, 327 (1966).

[52] A.A. Zvyagin, J. Phys.: Condens. Matter **3**, 3865 (1991).

[53] A.A. Zvyagin, Zh. Eksp. Teor. Fiz. **98**, 1396 (1990).

[54] A.K. Hassan, L.A. Pardi, G.B. Martins, G. Cao, and L.C. Brunel, Phys. Rev. Lett. **80**, 1984 (1998).

[55] S. Hill, R.S. Edwards, N. Aliaga-Alcalde, and G. Christou, Science **302**, 1015 (2003).

[56] S.A. Zvyagin, A.K. Kolezhuk, J. Krzystek, and R. Feyerherm, Phys. Rev. Lett. **93**, 027201 (2004).

[57] A.A. Zvyagin, Phys. Rev. B **79**, 064422 (2009).

[58] M Oshikawa and I. Affleck, Phys. Rev. Lett. **82**, 5136 (1999).

[59] A.A. Zvyagin, Phys. Rev. B **63**, 172409 (2001).

[60] M Oshikawa and I. Affleck, Phys. Rev. B **65**, 134410 (2002).

[61] A. Möller, T. Taetz, N. Hollmann, J.A. Mydosh, V. Kataev, M. Yehia, E. Vavilova, and B. Büchner, Phys. Rev. B **76**, 134411 (2007).

[62] E. Vavilova, A.S. Moskvin, A. Arango, A. Sotnikov, S.L. Drechsler, R. Klingeler, O. Volkova, A. Vasiliev, V. Kataev, and B. Büchner, Eur. Phys. Lett. **88**, 27001 (2009).

[63] H. Manaka and I. Yamada, Phys. Rev. B **62**, 14279 (2000).

[64] Yi. Liu, J. Drumheller, and R.D. Willet, Phys. Rev. B **52**, 15327 (1995).

[65] U. Geiser, R.M. Gaura, R.D. Willet, and D.X. West, Inorg. Chem. **25**, 4203 (1986).

[66] C. Yasuda, S. Todo, K. Hukushima, F. Alet, M. Keller, M. Troyer, and H. Takayama, Phys. Rev. Lett. **94**, 217201 (2005).

[67] S. Blundell *et al.*, unpublished.

[68] S. Eggert, I. Affleck, and M. Takahashi, Phys. Rev. Lett. **73**, 332 (1992).

[69] M. Ozerov, E. Čižmár, J. Wosnitza, S.A. Zvyagin, F. Xiao, C.P. Landee, and M.M. Turnbull, J. Phys: Conf. Series **150**, 042159 (2009).

[70] E.S.R Gopal, *Specific heat at low temperature*, Plenum Press, New York, 102 (1966).

[71] R. Feyerherm, S. Abens, D. Günther, T. Ishida, M. Meißner, M. Meschke, T. Nogami, and M. Steiner, J.Phys.: Condens. Matter **12**, 8495 (2000).

[72] M. Ozerov, A.A. Zvyagin, E. Čižmár, J. Wosnitza, R. Feyerherm, F. Xiao, C.P. Landee, and S.A. Zvyagin, Phys. Rev. B **82**, 014416 (2010).

[73] A.A. Zvyagin, Phys. Lett. A **158**, 333 (1991).

[74] W.E. Marsh, W.J. Valente, and D.J. Hodgson, Inorg. Chim. Acta **51**, 49 (1981).

[75] J.A.C. van Ooijen, J. Reedijk, and A.L. Spek, J. Chem. Soc. Dalton Trans. **7**, 1183 (1979).

[76] J.W. Hall, W.E. Marsh, R.R. Weller, and W.E. Hatfield, Inorg. Chem. **20**, 1033 (1981).

[77] A.J. Wolthuis, W.J. Huiskamp, L.J. de Jongh, and J. Reedijk, Physica B&C **133**, 161 (1985).

[78] J.H. Smit, L. J. De Jongh, J.A.C. van Ooijen, J. Reedijk, and J.C. Bonner, Physica B **97**, 229 (1979).

[79] H.J.M. de Groot, L.J. de Jongh, R.D. Willett, and J. Reedijk, J. Appl. Phys. **53**, 8038 (1982).

[80] I. Affleck and M. Oshikawa, Phys. Rev. B **60**, 1038 (1999).

[81] D.C. Dender, P.R. Hammar, D.H. Reich, C. Broholm, and G. Aeppli, Phys. Rev. Lett. **79**, 1750 (1997).

[82] M. Kohgi, K. Iwasa, J.M. Mignot, B. Fak, P. Gegenwart, M. Lang, A. Ochiai, H. Aoki, and T. Suzuki, Phys. Rev. Lett. **86**, 2439 (2001).

[83] M. Kenzelmann, Y. Chen, C. Broholm, D.H. Reich, and Y. Qiu, Phys. Rev. Lett. **93**, 017204 (2004).

[84] I. Umegaki, H. Tanaka, T. Ono, H. Uekusaand, and H. Nojiri, Phys. Rev. B **70**, 184401 (2009).

[85] M. Oshikawa and I. Affleck, Phys. Rev. Lett. **79**, 2883 (1997).

[86] F.H.L. Essler, Phys. Rev. B **59**, 14376 (1999).

[87] T. Giamarchi, *Quantum physics in one dimension*, Oxford 2003.

[88] F.H.L. Essler, A. Furusaki, and T. Hikihara, Phys. Rev. B **68**, 064410 (2003).

[89] J.Z. Zhao, X.Q. Wang, T. Xiang, Z.B. Su, and L. Yu, Phys. Rev. Lett. **90**, 207204 (2003).

[90] J. Lou, S. Qin, C. Chen, Z. Su, and L. Yu, Phys. Rev. B **65**, 064420 (2002).

[91] J.B. Fouet, O. Tchernyshyov, and F. Mila, Phys. Rev. B **70**, 174427 (2004).

[92] H. Nojiri, Y. Ajiro, T. Asano, and J.P. Boucher, New J. Phys. **8**, 218 (2006).

[93] A.U.B. Wolter, H. Rakoto, M. Costes, A. Honecker, W. Brenig, A. Klümper, H.H. Klauss, F.J. Litterst, R. Feyerherm, D. Jérome, and S. Süllow, Phys. Rev. B **68**, 220406(R) (2003).

[94] M. Yasui, Y. Ishikawa, N. Akiyama, T. Ishida, T. Nogami and F. Iwasaki, Acta Crystallogr. B **57**, 288 (2001).

[95] T. Ishida, K. Nakayama, M. Nakagawa, W. Sato, Y. Ishikawa, M. Yasuri, F. Iwasaki, and T. Nogami, Synth. Met. **85**, 1655 (1997).

[96] J.Z. Lou, C.F. Chen, J.Z. Zhao, X.Q. Wang, T. Xiang, Z.B. Su, and L. Yu, Phys. Rev. Lett. **94**, 217207 (2005).

[97] J.Z. Lou, C.F. Chen, and X.Q. Wang, Phys. Rev. B **73**, 092407 (2006).

[98] E. Dagotto and T.M. Rice, Science **271**, 618 (1996).

[99] M. Uehara, T. Nagata, J. Akimitsu, H. Takahashi, N. Môri, and K. Kinoshita, J. Phys. Soc. Jpn. **65**, 2764 (1996).

[100] T. Giamarchi and A.M. Tsvelik, Phys. Rev. B **59**, 11398 (1999).

[101] H.J. Mikeska and A.K. Kolezhuk, Quantum Magnetism, Lect. Notes Phys. **645**, 1 (2004).

[102] S. Tomonaga, Prog. Theor. Phys. **5**, 544 (1950).

[103] J.M. Luttinger, J. Math. Phys. **4**, 1154 (1963).

[104] F.D.M. Haldane, Phys. Rev. Lett. **45**, 1358 (1980); J. Phys. C: Solid State Phys. **14**, 2585, (1981).

[105] M. Azuma, Z. Hiroi, M. Takano, K. Ishida, and Y. Kitaoka, Phys. Rev. Lett. **73**, 3463 (1994).

[106] C.P. Landee, M.M. Turnbull, C. Galeriu, J. Giantsidis, and F.M. Woodward, Phys. Rev. B **63**, 100402 (2001).

[107] T. Masuda, A. Zheludev, H. Manaka, L.P. Regnault, J.H. Chung, and Y. Qiu, Phys. Rev. Lett. **96**, 047210 (2006).

[108] B.C. Watson, N.V. Kotov, M.W. Meisel, D.W. Hall, G.E. Granroth, W.T. Montfrooij, S.E. Nagler, D.A. Jensen, R. Backov, M.A. Petruska, G.E. Fanucci, and D.R. Talham, Phys. Rev. Lett. **86**, 5168 (2001).

[109] M. Klanjšek, H. Mayaffre, C. Berthier, M. Horvatić, B. Chiari, O. Piovesana, P. Bouillot, C. Kollath, E. Orignac, R. Citro, and T. Giamarchi, Phys. Rev. Lett. **101**, 137207 (2008).

[110] B. Thielemann, Ch. Rüegg, K. Kiefer, H.M. Rønnow, P. Bouillot, C. Kollath, E. Orignac, R. Citro, T. Giamarchi, A.M. Läuchli, D. Biner, K. Krämer, F. Wolff-Fabris, V. Zapf, M. Jaime, J. Stahn, N.B. Christensen, B. Grenier, D.F. McMorrow, and J. Mesot, Phys. Rev. B **79**, 020408(R) (2009).

[111] B. Thielemann, Ch. Rüegg, H.M. Rønnow, A.M. Läuchli, J.S. Caux, B. Normand, D. Biner, K. Krämer, H.U. Güdel, J. Stahn, K. Habicht, K. Kiefer, M. Boehm, D.F. McMorrow, and J. Mesot, Phys. Rev. Lett. **102**, 107204 (2009).

[112] Ch. Rüegg, K. Kiefer, B. Thielemann, D.F. McMorrow, V. Zapf, B. Normand, M.B. Zvonarev, P. Bouillot, C. Kollath, T. Giamarchi, S. Capponi, D. Poilblanc, D. Biner, and K.W. Krämer, Phys. Rev. Lett. **101**, 247202 (2008).

[113] A.V. Sologubenko, T. Lorenz, J.A. Mydosh, B. Thielemann, H.M. Rönnow, Ch. Rüegg, and K.W. Krämer, Phys. Rev. B **80**, 220411 (2009).

[114] E. Orignac and T. Giamarchi, Phys. Rev. B **57**, 5812 (1998).

[115] A.P. Tonel, A. Foerster, J. Links, and A.L. Malvezzi, Phys. Rev. B **64**, 054420 (2001).

[116] R. Citro and E. Orignac, Phys. Rev. B **65**, 134413 (2002).

[117] Z.J. Ying, I. Roditi, A. Foerster, and B. Chen, Eur. Phys. J. B **41**, 67 (2004).

[118] E. Orignac, R. Citro, S. Capponi, and D. Poilblanc, Phys. Rev. B **76**, 144422 (2007).

[119] K. Penc, J.B. Fouet, S. Miyahara, O. Tchernyshyov, and F. Mila, Phys. Rev. Lett. **99**, 117201 (2007).

[120] S. Miyahara, J.B. Fouet, S.R. Manmana, R.M. Noack, H. Mayaffre, I. Sheikin, C. Berthier, and F. Mila, Phys. Rev. B **75**, 184402 (2007).

[121] B.R. Patyal, B.L. Scott, and R.D. Willett, Phys. Rev. B **41**, 1657 (1990).

[122] R.D. Willett, C. Galeriu, C.P. Landee, M.M. Turnbull, B. Twamley, Inorg. Chem. **43**, 3804 (2004).

[123] A.T. Savici, G.E. Granroth, C.L. Broholm, D.M. Pajerowski, C.M. Brown, D.R. Talham, M.W. Meisel, K.P. Schmidt, G.S. Uhrig, and S.E. Nagler, Phys. Rev. B **80**, 094411 (2009).

[124] F. Anfuso, M. Garst, A. Rosch, O. Heyer, T. Lorenz, Ch. Rüegg, and K. Krämer, Phys. Rev. B **77**, 235113 (2008).

[125] T. Lorenz, O. Heyer, M. Garst, F. Anfuso, A. Rosch, Ch. Rüegg, and K. Krämer, Phys. Rev. Lett. **100**, 067208 (2008).

[126] K.Y. Choi, V. Gnezdilov, B.C. Watson, M.W. Meisel, D.R. Talham, and P. Lemmens, J. Phys.: Condens. Matter **17**, 4237 (2005).

[127] T. Nikuni, M. Oshikawa, A. Oosawa, and H. Tanaka, Phys. Rev. Lett. **84**, 5868 (2000);

[128] S. Wessel, M. Olshanii, and S. Haas, Phys. Rev. Lett. **87**, 206407 (2001).

[129] E. Čižmár, M. Ozerov, J. Wosnitza, B. Thielemann, K.W. Krämer, Ch. Rüegg, O. Piovesana, M. Klanjšek, M. Horvatić, C. Berthier, and S.A. Zvyagin, Physical Review B **82**, 054431 (2010).

[130] B. Bleaney and D.K. Bowers, Proc. Roy. Soc (London) **A214**, 451 (1952).

[131] A. Abragam and B. Bleaney, *Electron Paramagnetic Resonance of Transition Ions* (Claredon Press, Oxford, 1970).

[132] S. Stoll and A. Schweiger, J. Magn. Reson. **178**, 42 (2006).

[133] S. Zvyagin, B.C. Watson, J.H. Park, D.A. Jensen, A. Angerhofer, L.C. Brunel, D.R. Talham, and M.W. Meisel, Physica B **329-333**, 1211 (2003).

[134] P.W. Anderson and J. Photogr. Sci. **9**, 316 (1954).

[135] V.N. Glazkov, A.I. Smirnov, H. Tanaka, and A. Oosawa, Phys. Rev. B **69**, 184410 (2004).

[136] S.A. Zvyagin, J. Wosnitza, J. Krzystek, R. Stern, M. Jaime, Y. Sasago, and K. Uchinokura, Phys. Rev. B **73**, 094446 (2006).

[137] S.E. Sebastian, P. Tanedo, P.A. Goddard, S.C. Lee, A. Wilson, S. Kim, S. Cox, R.D. McDonald, S. Hill, N. Harrison, C.D. Batista, and I.R. Fisher, Phys. Rev. B **74**, 180401 (2006).

[138] A. Carrington, A. D. McLachlan, Introduction to Magnetic Resonance (Harper and Row, New York, 1967).

[139] T. Kaplan, Z. Phys. B **49**, 313 (1983).

[140] L. Shekhtman, O. Entin-Wohlman, and A. Aharony, Phys. Rev. Lett. **69**, 836 (1992).

[141] N. Mermin and H. Wagner, Phys. Rev. Lett. **17**, 1133 (1966).

[142] P. Sengupta, A.W. Sandvik, and R.R.P. Singh, Phys. Rev. B **68**, 094423 (2003).

[143] H.Q. Ding, Phys. Rev. Lett. **68**, 1927 (1992).

[144] A. Cuccoli, G. Gori, R. Vaiaa, and P. Verrucchi, J. Appl. Phys. **99**, 08H503 (2006).

[145] B.B. Beard, R.J. Birgeneau, M. Greven, and U.J. Wiese, Phys. Rev. Lett. **80**, 1742 (1998).

[146] A. Cuccoli, T. Roscilde, V. Tognetti, R. Vaia, and P. Verrucchi, Phys. Rev. B **67**, 104414 (2003).

[147] V.L. Berezinskii, Zhur. Eksp. Teor. Fiz. **59**, 907 (1970).

[148] V.L. Berezinskii, Zhur. Eksp. Teor. Fiz. **61**, 1144 (1971).

[149] J.M. Kosterlitz and D.J. Thouless, J. Phys. **C5**, L124 (1972).

[150] J.M. Kosterlitz and D.J. Thouless, J. Phys. **C6**, 1181 (1973).

[151] R. Gupta and C.F. Baillie, Phys. Rev. B **45**, 2883 (1992).

[152] H.Q. Ding, Phys. Rev. B **45**, 230 (1992).

[153] H.Q. Ding and M.C. Makivić, Phys. Rev. B **42**, 6827 (1990).

[154] A. Cuccoli, T. Roscilde, R. Vaia, and P.Verrucchi, Journal of Magnetism and Magnetic Materials **272-276**, 884 (2004).

[155] A. Cuccoli, V. Tognetti, R. Vaia, and P. Verrucchi, Phys. Rev. B **56**, 14456 (1997).

[156] P. Sengupta, C.D. Batista, R.D. McDonald, S. Cox, J. Singleton, L. Huang, T.P. Papageorgiou, O. Ignatchik, T. Herrmannsdörfer, J.L. Manson, J.A. Schlueter, K.A. Funk, and J. Wosnitza, Phys. Rev. B **79**, 060409(R) (2009).

[157] A. Cuccoli, T. Roscilde, R. Vaia, and P. Verrucchi, Phys. Rev. B **68**, 060402(R) (2003).

[158] J.C. Bonner and M.E. Fisher, Phys. Rev. **135**, A640 (1964).

[159] U. Balucani, L. Capriotti, A. Cuccoli, A. Fubini, and V. Tognetti, T. Roscilde, R. Vaia, and P. Verrucchi, Low Temp. Phys. **31**, 668 (2005).

[160] E. Čižmár, S.A. Zvyagin, R. Beyer, M. Uhlarz, M. Ozerov, Y. Skourski, J.L. Manson, J.A. Schlueter, and J. Wosnitza, Phys. Rev. B **81**, 064422 (2010).

[161] A. Santoro, A.D. Mighell, and C.W. Reimann, Acta Crystallogr. **B26**, 979 (1970).

[162] H.W. Richardson, and W.J. Hatfield, Am. Chem. Soc. **98**, 835 (1976).

[163] S. Amaral, W.E. Jensen, C.P. Landee, M.M. Turnbull, and F.M. Woodward, Polyhedron **20**, 1317 (2001).

[164] P. Lumme, S. Lindroos, and E. Lindell, Acta Crystallogr., Sect. C **43**, 2053 (1987).

[165] M.M. Turnbull, G. Pon, and R.D. Willett, Polyhedron **15**, 1835 (1991).

[166] P.A. Goddard, J. Singleton, P. Sengupta, R.D. McDonald, T. Lancaster, S.J. Blundell, F.L. Pratt, S. Cox, N. Harrison, J.L. Manson, H.I. Southerland, and J.A. Schlueter, New J. Phys. **10**, 083025 (2008).

[167] F. Xiao, F.M. Woodward, C.P. Landee, M.M. Turnbull, C. Mielke, N. Harrison, T. Lancaster, S.J. Blundell, P.J. Baker, P. Babkevich, and F. L. Pratt, Phys. Rev. B **79**, 134412 (2009).

[168] F.M. Woodward, P.J. Gibson, G.B. Jameson, C.P. Landee, M.M. Turnbull, and R.D. Willett, Inorg. Chem. **46**, 4256 (2007).

[169] J.L. Manson, M.M. Conner, J.A. Schlueter, T. Lancaster, S.J. Blundell, M.L. Brooks, F.L. Pratt, T. Papageorgiou, A.D. Bianchi, J. Wosnitza, and M.H. Whangbo, Chem. Commun., 4894 (2006).

[170] J.L. Manson, J.A. Schlueter, K.A. Funk, H.I. Southerland, B. Twamley, T. Lancaster, S.J. Blundell, P.J. Baker, F.L. Pratt, J. Singleton, R.D. McDonald, P.A. Goddard, P. Sengupta, C.D. Batista, L. Ding, C. Lee, M.H. Whangbo, I. Franke, S. Cox, C. Baines, and D. Trial, J. Am. Chem. Soc. **131**, 6733 (2009).

[171] F.M. Woodward, A.S. Albrecht, C.M. Wynn, C.P. Landee, and M.M. Turnbull, Phys. Rev. B **65**, 144412 (2002).

[172] Y. Wang, T. Plackowski, and A. Junod, Physica C **355**, 179 (2001).

[173] R. Lortz, Y. Wang, A. Demuer, P.H.M. Böttger, B. Bergk, G. Zwicknagl, Y. Nakazawa, and J. Wosnitza, Phys. Rev. Lett. **99**, 187002 (2007).

[174] S. Cox, R.D. McDonald, J. Singleton, S. Miller, P.A. Goddard, S. El Shawish, J. Bonca, J.A. Schlueter, and J.L. Manson, arXiv:0907.3514 (unpublished).

[175] Y.J. Kim and R.J. Birgeneau, Phys. Rev. B **62**, 6378 (2000).

[176] E.A. Turov, Physical Properties of Magnetically Ordered Crystals (Academic Press, 1965).

[177] J.W. Battles and G.E. Everett, Phys. Rev. B **1**, 3021 (1970).

8. List of publications

1. S.A. Zvyagin, E. Čižmár, M. Ozerov, J. Wosnitza, R. Feyerherm, S.R. Manmana, and F. Mila;
   Field-induced gap in a quantum spin-$\frac{1}{2}$ *chain in a strong magnetic field*
   Physical Review B **83**, 060409(R) (2011).

2. E. Čižmár, M. Ozerov, J. Wosnitza, B. Thielemann, K.W. Krämer, Ch. Rüegg, O. Piovesana, M. Klanjšek, M. Horvatić, C. Berthier, and S.A. Zvyagin;
   Anisotropy of magnetic interactions in the spin-ladder compound $(C_5H_{12}N)_2CuBr_4$
   Physical Review B **82**, 054431 (2010).

3. M. Ozerov, A.A. Zvyagin, E. Čižmár, J. Wosnitza, R. Feyerherm, F. Xiao, C.P. Landee, and S.A. Zvyagin;
   Spin dynamics in $S = 1/2$ *chains with next-nearest-neighbor exchange interactions*
   Physical Review B **82**, 014416 (2010).

4. E. Čižmár, M. Ozerov, Y. Skourski, S.A. Zvyagin, J.A. Schlueter, J.L. Manson, and J. Wosnitza;
   High-field magnetization study of $[Cu(pyz)_2HF_2]PF_6$*: an* $S = 1/2$ *quasi-two-dimensional Heisenberg magnet*
   Journal of Low Temperature Physics **159**, 92 (2010).

5. E. Čižmár, S.A. Zvyagin, R. Beyer, M. Uhlarz, M. Ozerov, Y. Skourski, J.L. Manson, J.A. Schlueter, and J. Wosnitza;
   Magnetic properties of the quasi-two-dimensional $S = 1/2$ *Heisenberg antiferromagnet* $[Cu(pyz)_2(HF_2)]PF_6$
   Physical Review B **81**, 064422 (2010).

6. D. Kropman, E. Mellikov, A. Öpik, K. Lott, T. Kärner, I. Heinmaa, T. Laas, A. Medvid, W. Skorupa, S. Prucnal, L. Rebohle, S.A. Zvyagin, E. Čižmár, M. Ozerov, and J. Wosnitza;
Interaction of point defects with impurities in the Si-SiO_2 system and its influence on the properties of the interface
Thin Solid Films, **158**, 2374 (2010).

7. A.A. Validov, E.M. Lavrentyeva, M. Ozerov, S.A. Zvyagin, M.M. Turnbull, C.P. Landee and G.B. Teitel'baum;
Quantum critical dynamics of $S = 1/2$ antiferromagnetic Heisenberg chains studied in CuPzN by ESR
Journal of Physics: Conference Series **200**, 022070 (2010).

8. S.A. Zvyagin, M. Ozerov, E. Čižmár, D. Kamenskyi, S. Zherlitsyn, T. Herrmannsdörfer, J. Wosnitza, R. Wünsch, and W. Seidel;
Terahertz-range free-electron laser electron spin resonance spectroscopy: Techniques and applications in high magnetic fields
Review of scientific instruments **80**, 073102 (2009).

9. E. Čižmár, M. Ozerov, J. Wosnitza, S.A. Zvyagin, J. Krzystek, C.P. Landee, B.R. Landry, M.M. Turnbull and J.L. Wikaira;
Magnetic properties of the Zn-doped Haldane-gap material NENB
Journal of Physics: Conference Series **150**, 042017 (2009).

10. M. Ozerov, E. Čižmár, J. Wosnitza, S.A. Zvyagin, F. Xiao, C.P. Landee, and M.M. Turnbull;
Magnetic properties of the $S = 1/2$ Heisenberg spin-chain material (6MAP)$CuCl_3$
Journal of Physics: Conference Series **150**, 042159 (2009).

11. E. Čižmár, M. Ozerov, O. Ignatchik, T.P. Papageorgiou, J. Wosnitza, S.A. Zvyagin, J. Krzystek, Z. Zhou, C.P. Landee, B.R. Landry, M.M. Turnbull, and J.L. Wikaira;
Magnetic properties of the Haldane-gap material $Ni(N_2C_2H_6)_2NO_2BF_4$
New Journal of Physics **10**, 033008 (2008).

9. Versicherung

Hiermit versichere ich, dass ich die vorliegende Arbeit ohne unzulässige Hilfe Dritter und ohne Benutzung anderer als der angegebenen Hilfsmittel angefertigt habe. Die aus fremden Quellen direkt oder indirekt übernommenen Gedanken sind als solche kenntlich gemacht. Die Arbeit wurde bisher weder im Inland noch im Ausland in gleicher oder ähnlicher Form einer anderen Prüfungsbehörde vorgelegt.

Die vorliegende Doktorarbeit wurde am Hochfeld-Magnetlabor Dresden im Forschungszentrum Dresden-Rossendorf e. V. unter der wissenschaftlichen Betreuung von Herrn Dr. Sergei Zvyagin angefertigt.

Ich erkenne die Promotionsordnung der Technischen Universität Dresden an.

Dresden, den 12. November 2010

Mykhaylo Ozerov

10. Curriculum vitae

Mykhaylo Viktorovich Ozerov, born 21 April 1982 in Storozhynets, Chernivtsi region, Ukraine

1989 - 1999	Storozhynets secondary school, Ukraine. Finishing with honors.
1996 - 1999	Participation in all-Ukrainian Competition of Young Physicists. Diploma of the III degree.
1999 - 2001	Chernivtsy National University, Ukraine. Department of Physics (specialization: Radioengineering).
2002 - 2005	Taras Shevchenko National Kyiv University, Ukraine. Department of Physics (specialization: Laser and optoelectronic devices). Magister diploma with honors.
2005 - 2007	Ph.D. student in Taras Shevchenko National Kyiv University. (specialization: Optics. Laser Physics).
2007 - 2011	Ph.D. student in Dresden High Magnetic Field Laboratory in Research Center Dresden-Rossendorf e. V., Germany. (Hochfeld-Magnetlabor Dresden, Forschungszentrum Dresden-Rossendorf, Deutschland).
4. May 2011	Defense of the dissertation

11. Acknowledgment

I am heartily thankful to my supervisors, Prof. Jochen Wosnitza and Dr. Sergei Zvyagin, whose encouragement, guidance and support from the initial to the final level enabled me accomplish this thesis. Particularly, I would like to thank Prof. Jochen Wosnitza for giving me the opportunity to realize myself as a researcher at the Forschungszentrum Dresden - Rossendorf. I deeply appreciate my guru, Sergei Zvyagin, for permanent willingness to discuss encountered problems. During all time he indefatigably was passing on his scientific knowledge and experience to me and I would be rather happy if I can a little justify his efforts. I owe my special gratitude to Prof. Bernd Pilawa for his kind consent to be a second reviewer.

I am indebted to many of my colleagues at the Dresden High Magnetic Field Laboratory for creating the beautiful working atmosphere and many fruitful collaborations. In particular, I would like to thank Dr. E. Čižmár; working with him in the same group was a really great pleasure. Without his personal and attentive support and assistance, and deep support on the theoretical and on the experimental area, this work would have taken a much longer time. I would like to thank Y. Skourski and S. Zherlitsyn for their help with the pulsed-field experiments. I also thank R. Beyer and M. Uhlarz for specific-heat and the magnetic susceptibility measurements. I appreciate the participation of F. Möller, U. Bartheld, and other technicians from the HLD workshop, who helped me to design and to built ESR equipment.

I would also like to thank Dr. W. Seidel, R. Schurig, and the FELBE team for their support in pulsed-field experiments with free-electron laser. I thank A.A. Zvyagin (Institute for Low Temperature Physics and Engineering, Kharkov, Ukraine) for many fruitful discussions.

I am much obliged to my teachers and former supervisors L.M. Fedorenko, A.P. Fedorenko, L.V. Poperenko, M.V. Vinnichenko, who gave me thorough grounding and qualities necessary for becoming a researcher. To my parents and wife I express sincere gratitude for the continuous support, attention and love. Mother's grit and assiduousness in the work was an striking example, stimulating me in a preparation and an implementation of these experiments. A very heartfelt thanks are addressed to my dear wife, not only because of providing with delicious lunches, but because of a warm caring and an encouragement, which prevented me to be cast down.

Finally, I would like to acknowledge the support of Deutsche Forschungsgemeinschaft, SFB 463, EuroMagNET II (EU under Contract No. 228043).